

**MODELING OF NC-AFM EXPERIMENTS BY  
THE UTILIZATION OF MOLECULAR  
DYNAMICS AND THE HARMONIC  
OSCILLATOR MODEL**

A THESIS SUBMITTED TO  
THE GRADUATE SCHOOL OF ENGINEERING AND SCIENCE  
OF BILKENT UNIVERSITY  
IN PARTIAL FULFILLMENT OF THE REQUIREMENTS FOR  
THE DEGREE OF  
MASTER OF SCIENCE  
IN  
MECHANICAL ENGINEERING

By

Berkin Uluutku

July, 2017

MODELING OF NC-AFM EXPERIMENTS BY THE UTILIZATION OF  
MOLECULAR DYNAMICS AND THE HARMONIC OSCILLATOR MODEL

By Berkin Uluutku

July, 2017

We certify that we have read this thesis and that in our opinion it is fully adequate, in scope and in quality, as a thesis for the degree of Master of Science.

---

Mehmet Zeyyad Baykara (Advisor)

---

Mehmet Selim Hanay

---

Ahmet Oral

Approved for the Graduate School of Engineering and Science:

---

Ezhan Karařan  
Director of the Graduate School

## ABSTRACT

# MODELING OF NC-AFM EXPERIMENTS BY THE UTILIZATION OF MOLECULAR DYNAMICS AND THE HARMONIC OSCILLATOR MODEL

Berkin Uluutku

M.S. in Mechanical Engineering

**Advisor:** Mehmet Zeyyad Baykara

July, 2017

Atomic force microscopy is a widely-used instrument in nanotechnology and nanoscience. Imaging of single molecules, atoms or even bond structures and tip-sample interactions with pm and pN resolution are made possible with non-contact atomic force microscope (NC-AFM) techniques. Since very high resolution imaging is relatively recent and underlying effects are not yet fully understood, interpretation of images can be controversial and may differ. Therefore theoretical modeling is used alongside with experimental work in order to gain a better insight about underlying physical phenomena regarding NC-AFM images and related artifacts.

In this thesis work, a simulator for NC-AFM experiments is suggested which utilizes the harmonic oscillator equations for AFM cantilever dynamics and molecular dynamics (MD) for the interaction between tip and sample. For this purpose, a model graphene surface with underlying platinum substrate and a platinum tip is created and their interaction is mapped at different distances with MD techniques. Calculated interaction forces are fitted to polynomials and imported to the harmonic oscillator model. With the harmonic oscillator model and imported interaction data, two different operating modes of NC-AFM are modeled: *Constant Height* and *Topography Scan*.

When obtained force maps are investigated, tip asymmetry related artifacts are observed. Due to tip asymmetry, a shift in detected atom positions and overall spatial disturbance are observed. Furthermore, the mobility of atoms causes elongation of the

tip and a bumpy formation of the sample surface near the tip. Elongation of the tip decreased the overall interaction due to increasing sharpness of the tip. Also an overall noise is detected due to individual, thermally-induced movements of atoms.

Obtained NC-AFM scan results were able to map the surface as desired. In constant height mode, more attractive hollow-site regions of graphene are detected via high frequency shifts, as expected. Also due to increasing interaction, closer tip-surface distances resulted in higher frequency shifts. Increasing oscillation amplitudes caused a decrease in the ratio of short-range interactions over the whole oscillation cycle and hence decreased the frequency shift. In the topography scan mode, attractive hollow-site regions are tracked as expected; increasing the set frequency shift also increased the topography corrugation and decreased the mean tip-sample distance. Moreover, non-optimal (too slow or too fast) distance controllers resulted in tracking the surface in an unreliable way and controller-induced noise. With these results, a functional NC- AFM model is demonstrated which is able to satisfactorily simulate NC-AFM experiments.

**Keywords:** Nanotechnology, Nanoscience, Non-contact Atomic Force Microscope, Molecular Dynamics, Harmonic Oscillator Model

## ÖZET

# MOLEKÜLER DİNAMİK VE HARMONİK OSİLATÖR MODELİNİN KULLANIMIYLA TEMASSIZ AKM DENEYLERİNİN MODELLENMESİ

Berkin Uluutku

Makine Mühendisliği, Yüksek Lisans

**Tez Danışmanı:** Mehmet Zeyyad Baykara

Temmuz, 2017

Atomik kuvvet mikroskopisi (AKM), nanoteknoloji ve nanobilimde yaygın olarak kullanılan bir cihazdır. Temassız AKM teknikleri yardımı ile moleküllerin, atomların ve hatta bağ yapıları ile uç-numune etkileşimlerinin görüntülerini pm ve pN mertebesinde çözünürlükle elde etmek mümkündür. Yüksek çözünürlüklü temassız AKM ile görüntüleme deneyleri göreceli olarak yeni olduklarından, ilgili fiziksel mekanizmalar tamamıyla aydınlanabilmiş değildir ve yorumlamalarda farklılıklar görülebilmektedir. Bu sebeple, yapılan deneylerin ve AKM görüntülerindeki yapay etkilerin ardında yatan fiziksel olguları daha iyi anlamak amacıyla, deneylere ek olarak teorik modelleme kullanılmaktadır.

Bu tez çalışmasında; uç ile numune arasındaki etkileşimler için moleküler dinamik (MD), AKM giriş dinamiği için de harmonik osilatör denklemlerini kullanan bir temassız AKM simülatörü önerilmiştir. Bu amaçla örnek yüzey olarak platin alttaş tarafından desteklenen bir grafen yüzey ile platin bir AKM ucu oluşturulmuş ve aralarında farklı uzaklıklarda meydana gelen etkileşimler MD teknikleri ile hesaplanmıştır. Hesaplanan etkileşim kuvvetleri polinom eğrilerine uydurulmuş ve harmonik osilatör modeline aktarılmıştır. Harmonik osilatör modeli ile temassız AKM'nin iki farklı çalışma modu modellenmiştir: Sabit Yükseklik ve Topografi Taraması.

Elde edilen kuvvet haritaları incelendiğinde, uç asimetrisinden kaynaklanan tutarsızlıklar gözlemlenmiştir. Uç asimetrisinden ötürü, algılanan atom pozisyonlarında kayma ve genel mekânsal bozulma gözlemlenmiştir. Ayrıca, atomların hareketliliği uçta uzamaya ve yüzeyde uca yakın yerlerde tümsekleşmelere neden olmuştur. Uç uzaması, uçta sivrilmeye ve bu sebeple genel etkileşimde azalmaya sebep olmuştur. Buna ek olarak atomların bireysel termal hareketlerinden kaynaklanan genel bir gürültü tespit edilmiştir.

Elde edilen temassız AKM tarama sonuçları yüzeyi hedeflenen gibi haritalamayı başarmıştır. Sabit yükseklik modunda, çekimsel olarak daha kuvvetli etkileşim sergileyen grafenin boşluk bölgeleri, beklenildiği gibi, yüksek frekans sapması vasıtasıyla tespit edilmişlerdir. Buna benzer olarak, uç-yüzey mesafesinin kısaltılması, etkileşimi arttırdığından frekans sapmasında da artışa sebep olmuştur. AKM kirişinin titreşim genliğinin arttırılması, bir salınım döngüsü boyunca kısa mesafeli etkileşimlerin oranını azaltmış ve bu sebeple frekans sapmasında azalmaya sebep olmuştur. Topografi taraması modunda çekimsel olarak daha kuvvetli etkileşim yaratan boşluk bölgeleri başarılı bir şekilde takip edilmiştir; ayarlanan sapma frekansı artırıldıkça, ortalama uç-numune uzaklığı azalmış ve topografik farklar artmıştır. Bütün bunlara ek olarak, ideal olmayan (çok hızlı veya çok yavaş) mesafe kontrolcülerini kullanıldığında, yüzey güvenilir bir şekilde takip edilememiş ve kontrolcüden kaynaklanan gürültü artmıştır. Bu sonuçlar vasıtasıyla, temassız AKM deneylerini tatminkâr bir şekilde benzeten, işlevsel bir temassız AKM modeli gösterilmiştir.

**Anahtar Kelimeler:** Nanoteknoloji, Nanobilim, Temassız Atomik Kuvvet Mikroskobu, Moleküler Dinamik, Harmonik Osilatör Modeli

# Acknowledgement

Before anyone and anything, I would like to express my regards to my advisor Prof. Mehmet Zeyyad Baykara who has supported, advised and mentored me over the years. I am confident to say that I would be in a very different place as a different person if I haven't had a chance to work under his mentoring. He not only thought me how to do research but also helped me to choose a path for my life. Frankly, I do not think I can thank him enough.

Also I would like to thank all our former and recent group members who are individually unique in different ways: Pınar Karayaylalı, Arda Balkancı, Tuna Demirbaş, Ebru Cihan, Tarek Abdelwahab, Alper Özoğul, Zeynep Melis Süar, Nasima Afsharimani and the last but not least Verda Saygın who became more than a colleague and a friend. I am very glad to know them and I can say let alone that is a treasure.

I also would love to mention my professors at Bilkent University, who were very supporting in every way and taught me a lot. I also would love to thank them for being surprisingly patient with me.

Furthermore, I'd like to thank the friends I made during my studies in Bilkent University. I've collected good memories and experiences thanks to them which are priceless. Specifically, for this dissertation I would like to thank Müge Özcan for her fruitful discussions and bearing my intentional pestering whenever I got bored during my studies in the office.

I feel like I have to thank MATLAB which was like a magic carpet under me for several years. I do not think anything is impossible with MATLAB. Coding to computing, playing music to locating the Holy Grail (never tried but pretty sure it can do it).

Lastly, I want to thank my parents and my family who supported me in every way in every step of my life. It is very hard to imagine having realized even a miniscule achievement without their constant support starting from the day I was born. It is undefinably good to have some people believe in you constantly even when you stop believing in yourself.

*Hey dad! I'm one step closer to become a doctor...*

# Contents

|   |            |
|---|------------|
| <b>Acknowledgement .....</b>                    | <b>vii</b> |
| <b>List of Figures .....</b>                    | <b>xi</b>  |
| <b>1. Introduction .....</b>                    | <b>1</b>   |
| 1.1 Scanning Probe Microscopy .....             | 1          |
| 1.1.1 Basic Principles of SPM .....             | 3          |
| 1.1.2 Atomic Force Microscopy .....             | 4          |
| 1.2 Molecular Dynamics .....                    | 9          |
| 1.2.1 Basic Principles of MD .....              | 12         |
| 1.2.2 Applications of Molecular Dynamics .....  | 18         |
| <b>2. Literature Survey .....</b>               | <b>22</b>  |
| 2.1 Atomic Resolution Force Microscopy .....    | 22         |
| 2.2 Molecular Dynamics Simulations .....        | 32         |
| <b>3. Methodology .....</b>                     | <b>38</b>  |
| 3.1 MD Simulations .....                        | 38         |
| 3.2 Cantilever Dynamics .....                   | 42         |
| <b>4. Results and Discussion .....</b>          | <b>47</b>  |
| 4.1 Force Maps Obtained by MD Simulations ..... | 47         |
| 4.2 NC-AFM Scanning Results .....               | 56         |

|  |           |
|--|-----------|
| <b>5. Conclusion and Outlook .....</b> | <b>65</b> |
| <b>Bibliography .....</b>              | <b>67</b> |

# List of Figures

|   |    |
|---|----|
| <b>Figure 1.1</b> Illustration of a model surface, a model STM probe tip and tunneling current ( $I$ ) between them..   | 2  |
| <b>Figure 1.2</b> Some example SPM probe illustrations; (a) a STM tip, (b) cross section of a SNOM tip and (c) an AFM cantilever.....   | 4  |
| <b>Figure 1.3</b> Illustration of a model piezoelectric tube scanner. 4-cylinder-sliced piezoelectric elements are used for the actuation in x and y coordinates and one concentric cylindrical piezoelectric part for actuation in z direction.....  | 5  |
| <b>Figure 1.4</b> Illustration of a model photo detector that consist of four independent photo-diodes. Individual photo-diodes are marked with different letters..   | 6  |
| <b>Figure 1.5</b> A sample AFM illustration with a photodetector, cantilever and piezoelectric scanner.....   | 7  |
| <b>Figure 1.6</b> One of the macroscale liquid models built by J. D. Bernal in late 50's [19].  | 10 |
| <b>Figure 1.7</b> Logical computation sequence used in Alder and Wainwright's work published in 1959. Image reproduced from the referred paper [22]..   | 12 |
| <b>Figure 1.8</b> Lennard-Jones interaction between two generic atoms in reduced units. As can be seen from the figure, when the distance reaches the $1.12\sigma$ value, the repulsive part of equation starts to dominate the attractive part and in the distance of $\sigma$ , the potential energy reaches zero (equilibrium point).. | 15 |

|  |    |
|--|----|
| <b>Figure 1.9</b> A flowchart that shows a very basic running algorithm of a MD process..  | 18 |
| <b>Figure 1.10</b> Results of protein folding experiments done by Levitt and Warshel. Image has been reproduced from their 1975 Nature paper [34].   | 19 |
| <b>Figure 1.11</b> Image taken from Ye et al.'s work [36]. On the left, three layers of graphene and silicon dioxide tip can be seen. On the right, there is an additional layer of water molecules between tip and sample.  | 20 |
| <b>Figure 1.12</b> MD simulation of a single satellite tobacco mosaic virus in liquid water environment. The side of the virus capsule is made transparent in order to demonstrate inside of the virus [37].   | 21 |
| <b>Figure 2.1</b> (a) Block diagram of a Phase-Locked Loop (PLL). (b) Block diagram of a typical FM-AFM. Cantilever deflection signal is fed to a bandpass filter in order to filter the noise out. Phase-shifter shifts cantilever response by $-\frac{\pi}{2}$ to get the desired phase difference between input and output. Automatic gain control sets oscillation amplitude to a desired value and PLL provides frequency shift information [41].   | 24 |
| <b>Figure 2.2</b> (a) Representative illustration of a cantilever tracking a surface with atomic resolution. (b) Topography image of the Si (111) surface obtained with the-NC-AFM technique. In unit cell "A", a misplaced atom (which is a defect) can be seen (34 nm oscillation amplitude and 17 N/m cantilever stiffness) [42]. (c) Topography image of the Sn/Si (111) alloy surface (20 nm oscillation amplitude and 30.5 N/m cantilever stiffness) [44]. (d) Topography image of the KBr (001) surface with a visible step edge (0.15 nm oscillation amplitude and around 1800 N/m cantilever stiffness) [45]. (e) Topography image of C 60 molecules adsorbed on KBr (001) surface (0.15 nm oscillation amplitude and around 1800 N/m cantilever stiffness) [45]. | 26 |
| <b>Figure 2.3</b> (a) Illustration of C 60 molecular model, together with an STM image (b, c) Constant height NC-AFM measurements of C 60 molecule at different heights. Height is denoted on the images with z. Oscillation amplitude is 0.36 Å. (d) Illustration of Hexabenzocoronene model. (e) Constant height NC-AFM measurements of Hexabenzocoronene molecule. Oscillation amplitude is 0.35 Å. (f) Illustration of DBNP model. (g) Constant height NC-AFM measurements of DBNP molecule. Oscillation amplitude is 0.48 Å. Images reproduced and put together from the work of Gross et al. [46].   | 28 |

**Figure 2.4** (a) Illustration of the titanium dioxide (110) surface. (b) “All inclusive” NC-AFM image of the surface. Color scheme varies with frequency shift. Bridging oxygen atoms are detected as bright spots and titanium atoms form the less bright stripes between them. Both images are reproduced from the work of Bechstein et al. [47]... 29

**Figure 2.5** (a) Representation of a 3D force field with atomic corrugation. (b) Force map at 12 pm distance. (c) Force map at 52 pm distance. (d, e) Vertical slices from the 3D force field in (a). (f) Three vertical force curves on two different types of carbon atoms and hollow site on graphite. (g) Energy map at 12 pm distance. (h) Energy map at 52 pm distance. Images are taken from work of Baykara et al. [49]. ..... 31

**Figure 2.6** (a) Vertical force maps calculated on the NaCl (001) surface with tips of varying stiffness. Images in (a-d) are calculated alongside the [100] direction and the images in (e-h) alongside the [110] direction. Apparent size changes of attractive and repulsive regions with stiffness can be observed. In color scale, red corresponds to repulsive, blue corresponds to attractive interaction. Image is reproduced from [51]. 33

**Figure 2.7** (a-b) Horizontal force maps on obtained bilayer graphene surface with symmetric and asymmetric tips. Images in (c-d) are vertical force corrugation maps obtained along the white dotted lines in (a-b). Red sites correspond to less attractive regions whereas blue regions corresponds to more attractive regions. Image is reproduced from [52]. ..... 34

**Figure 2.8** 2D version of the tip-sample model used by Pishkenari & Meghdari in their study. Black spheres represent frozen atoms, orange spheres represent thermostated atoms and yellow spheres represent Newtonian atoms. Image is reproduced from Pishkenari & Meghdari’s work [52]. ..... 36

**Figure 2.9** NC-AFM scheme used in the work of Nony et al. published in 2006. Image is reproduced from reference [57]..... 37

**Figure 3.1** Constructed model sample which consists of single layer graphene on top of bulk platinum. Platinum substrate, single-layer graphene and graphene on platinum can be seen in (a), (b) and (c), respectively.. ..... 39

**Figure 3.2** Three stages of platinum tip construction. (a) Initial cubic structure. (b) Rotated version of the cube. (c) The tip after relaxation..... 40

**Figure 3.3** Side view of the simulated system. Red atoms are fixed, green atoms are thermostated and blue atoms are free to move. The image of the *PacMan* ghost represents the interactionless ghost atom that pulls the model tip with a rigid string. 42

**Figure 3.4** Block diagram of the NC-AFM model working in constant height mode. Frequency detection and driving the cantilever are performed by a phase-locked loop. Driving (excitation) signal’s amplitude is modulated with a PI amplitude controller. Interaction force is calculated with respect to the tip-surface distance and applied to the oscillating AFM cantilever..... 43

**Figure 3.5** Block diagram of the NC-AFM model working in constant height mode. Frequency detection and driving the cantilever are performed by a phase-locked loop. Driving (excitation) signal’s amplitude is modulated with a PI amplitude controller. Cantilever base – surface distance is modulated according to the difference between the actual frequency shift and a set value. Interaction force is calculated with respect to the tip-surface distance and applied to the oscillating AFM cantilever. .... 45

**Figure 4.1** (a) Force map obtained on the graphene surface in “Fixed Surface & Fixed Tip” configuration at 3 Å separation. (b) Force-distance data over a carbon atom and a hollow site and their interpolated curves. Separation after 3.5 Å distance is highly visible ..... 48

**Figure 4.2** In (a), the spatial disturbance in the force map due to tip asymmetry is marked. Two types of carbon atoms are named as A and B, and areas of the same magnitude of forces are enclosed with dashed lines. Two perimeters are projected on one another and the difference between the areas of A and B atoms becomes quite visible. In (b), actual positions of carbon atoms and a hollow site are marked on the force map acquired by the same asymmetric tip. An approximate 0.5 Å of lateral shift in detected positions is observed..... 49

**Figure 4.3** Two force maps obtained in the “Fixed Surface & Free Tip” configuration. (a) and (b) are taken at separations of 4.5 Å and 4 Å, respectively. There is considerable shift in detected lateral positions of surface sites along both x and y directions. Distortions and artifacts due to atomic motion are visible in (b)..... 51

**Figure 4.4** Histogram of tip atom heights (as measured from the tip apex). Free tip atoms are denoted by blue and fixed tip atoms are denoted by orange. Foremost tip atoms are assumed to have a height of zero before preparation of the histogram. As can

be seen from the histogram, the fixed tip contains more atoms in the near-surface region. The free tip is elongated and contains less atoms in the near-surface region. .... 52

**Figure 4.5** (a) Force-distance data over a carbon atom and a hollow site and their interpolated curves in the “Free Surface & Fixed Tip” configuration. Although separation starts before 3 Å, separation after 3 Å is quite clear. (b) Force map at 2.5 Å separation. The spatial disturbance of the honeycomb structure, caused by tip asymmetry and amplified by surface deformation, is clearly visible. Please note that the indicated tip-sample distances are with respect to the unrelaxed state of the system (i.e., before the graphene moves down to the platinum support by an additional 0.5 Å). ... 53

**Figure 4.6** A simulation snapshot from the “Free Surface & Fixed Tip” configuration. Carbon atoms close to the tip are elevated nearly 0.5Å toward the tip. A white guide line has been drawn under the line of carbon atoms to make elevated atoms more visible. The tip is followed by this bump of carbon atoms like a “Mexican wave”..... 54

**Figure 4.7** Force maps at (a) 3.5 Å and (b) 4 Å separation obtained in the “Free Surface & Free Tip” configuration. Although it is very easy to discern the honeycomb structure of the graphene at both tip heights, noise over the force maps due to atomic motion is clearly visible. .... 55

**Figure 4.8** Vertical slices of interaction forces obtained via different configurations. Blue and yellow colored parts represents more and less attractive parts of the surface, respectively. (a) Fixed Surface & Fixed Tip. (b) Fixed Surface & Free Tip. (c) Free Surface & Fixed Tip. (d) Free Surface & Free Tip..... 56

**Figure 4.9** NC-AFM scans of (a) “Fixed Surface & Fixed Tip” and (b) “Fixed Surface & Free Tip” configurations in constant height mode. Artifacts discussed for force maps of the configurations are carried over to the scans. Please note that the scan area in (a) is smaller than the horizontal force map presented in Figure 4.1a..... 57

**Figure 4.10** NC-AFM scans of (a) “Free Surface & Fixed Tip” and (b) “Free Surface & Free Tip” configurations in constant height mode. Artifacts discussed for force maps of the configurations are carried over to the scans. Please note that the scan area in (a) is smaller than the horizontal force map presented in Figure 4.5b. .... 58

**Figure 4.11** NC-AFM constant height mode images taken from the “Free Surface & Free Tip” configuration at (a) 4 Å and (b) 4.4 Å separations with 0.8 Å peak-to-peak

(p-p) oscillation amplitude. (c) Line profiles taken from NC-AFM scans at two different separations of 4.2Å and 4.4Å..... 59

**Figure 4.12** Constant height scans in the “Free Surface & Free Tip” configuration with 4.2 Å separation and two different p-p oscillation amplitudes: (a) 0.8 Å, (b) 1 Å. As can be seen from the images, increasing the oscillation amplitude decreases the overall frequency shift..... 60

**Figure 4.13** NC-AFM topography scan of the “Free Surface & Free Tip” configuration where (a) is the obtained topography map and (b) is the error signal map. Set frequency shift is -222 Hz. Hollow-sites are shown in the topography map with larger heights, in accordance with their higher reactivity when compared with carbon atoms ..... 61

**Figure 4.14** Two topography scans with (a) -200 Hz and (b) -222 Hz frequency shift values. With increasing deviation from the initial natural frequency, the corrugation of the topography maps increases, consistent with a smaller mean tip-sample distance. In (b) at the very bottom of the image there are visible artifact due to the less than ideal settings of the distance controller. Please note that the image in (b) has been acquired with different controller parameters than the image in Figure 4.13a. .... 612

**Figure 4.15** NC-AFM scan with -220 Hz frequency shift set point, 0.8 Å p-p oscillation amplitude and a very slow distance controller. (a) Topography map demonstrates very low corrugation (~2 pm) which may be impossible to detect in a real life experiment. (b) Error signal demonstrates very high corrugation in error, when compared with Figure 4.13b... ..... 623

**Figure 4.16** (a) Topography map obtained with -220 Hz frequency shift set point, 0.8 Å p-p oscillation amplitude and a very fast distance controller. Although corrugation is quite high, it is not easy to distinguish hollow sites of the graphene surface due to controller-induced overall noise over the image. (b) Blue graph demonstrates a line profile taken along the red dashed line in (a). Red line demonstrates the line profile taken from a different scan with a more optimal distance controller. As one can see, very fast controller parameters create additional noise over the physical features rather than improve tracking.. ..... 64

# Chapter 1

## Introduction

### 1.1 Scanning Probe Microscopy

Although atoms have been characterized in many different ways via different physical quantities, “seeing” a single atom was not possible until a new way of microscopy has been invented by Binnig et al. in 1981 [1]. Scanning tunneling microscope (STM) is able to get images of surfaces without getting affected by any diffraction limits, because it operates with the principle of “quantum tunneling”. Simply putting a very sharp, metallic probe tip near enough to a surface, optionally with a bias voltage to catalyze the process, makes electrons tunnel between the tip and surface (Figure 1.1). By precisely detecting and locking on the tunneling current between the tip and sample, the topography of the surface can be mapped. STM not only enables researchers to visualize individual atoms and atomic structures, but also provides very vast experimental opportunities. Apart from the ability to see individual atoms; STM provides opportunities to the measurement of spin states [2], standing waves of surface electrons [3], local density of states [4], [5] and many other measurements. In addition STM

makes possible the manipulation of surfaces on small length scales, such as the manipulation of individual atoms [6], charges [7] and spins [8]. STM is such a powerful instrument that the inventors of the STM –Binnig and Rohrer– received the Nobel Prize in Physics in 1986 due to their invention [9]. One can also argue that STM has additional significance in surface science because STM is the first scanning probe microscopy (SPM) technique and other SPM methods with various applications have originated from STM.

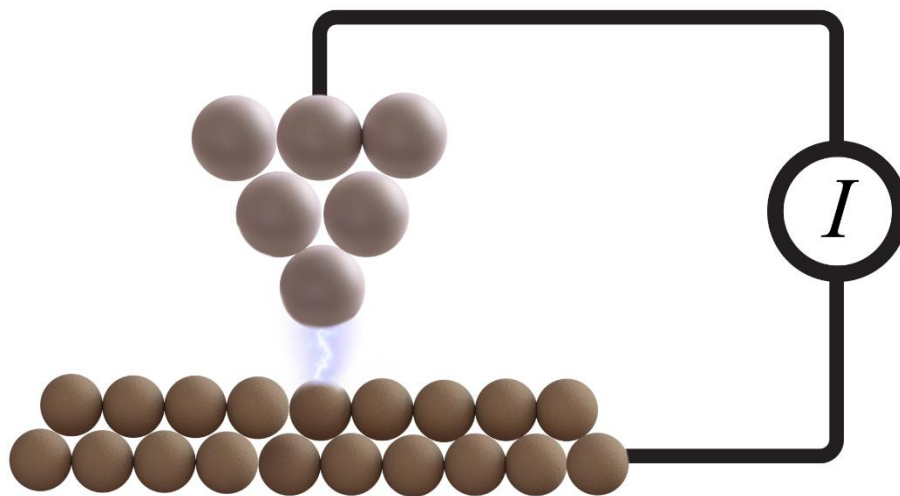


**Figure 1.1** Illustration of a model surface, a model STM probe tip and tunneling current ( $I$ ) flowing between them.

The SPM family of microscopy techniques has started with the STM as discussed above. Their operating principle can be generalized as interaction between a probe and a surface in various ways. As an example, this interaction between surface and the probe may be the tunneling current in STM while it can be the capacitance in scanning capacitance microscopy. There are several SPM techniques that are widely used. Some notable examples are:

- Scanning Tunneling Microscopy (STM)
- Magnetic Force Microscopy (MFM) [10]
- Scanning Capacitance Microscopy (SCM) [11]
- Scanning Hall Probe Microscopy (SHPM) [12]
- Near-field Scanning Optical Microscopy (NSOM) [13]
- Atomic Force Microscopy [14] [15] [16]

### 1.1.1 Basic Principles of SPM

As mentioned above, SPM techniques are based on recording some interaction between a surface to be imaged and a probe. This interaction can be many things depending on the SPM technique, including the tunneling current, force *etc.* In order to create and detect a desired interaction with the surface, a suitable probe is required. For instance, STM uses (ideally) atomically sharp needle-like tips to measure tunneling current between surface and the probe while NSOM uses a fiber-optic probe to emit and detect light and evanescent field. Although the type of probe may vary (Figure 1.2), a probe to interact with the surface is essential for any SPM operation. Further, this interaction may also be modulated/locked-onto with a feedback control loop. This control mechanism may be very simple or relatively complex depending on the application. But a quick example of SPM probe interaction and feedback can be given from the working mechanism of STM. In STM constant-current mode, the probe position is modulated during scanning in a way to keep the detected tunneling current constant. In a simple overview, the probe gets approached to the surface if tunneling current is less than desired and retracted from the surface if tunneling current is higher than desired

In order to be able to scan a surface, or even a line some actuation mechanism is needed to drive the probe across the substrate surface to be scanned. Hence a relative motion in  $x$ ,  $y$  and  $z$  coordinates is needed; it does not really matter whether the probe is moved across the surface or the surface moved beneath the probe. In modern SPMs usually this motion is provided by a piezoelectric transducer. Piezoelectric transducers use the piezoelectric effect for actuation of motion. An applied voltage difference to a piezoelectric material results in a strain in the material. In SPM scanners, usually PZT (lead zirconate titanate) type ceramic piezoelectric materials are used. Typical design of a piezoelectric scanner (Figure 1.3) consists of radially polarized arch shaped piezoelectric materials that form together a cylinder. Applying voltage to the independent piezoelectric parts of the cylinder makes those part expand or contract which results in a bending in the overall shape of cylinder that creates a motion in the  $x$  and  $y$  directions. In addition to these, in order to have an actuation in  $z$  direction a concentric cylindrical piezoelectric tube is attached to the system [14].

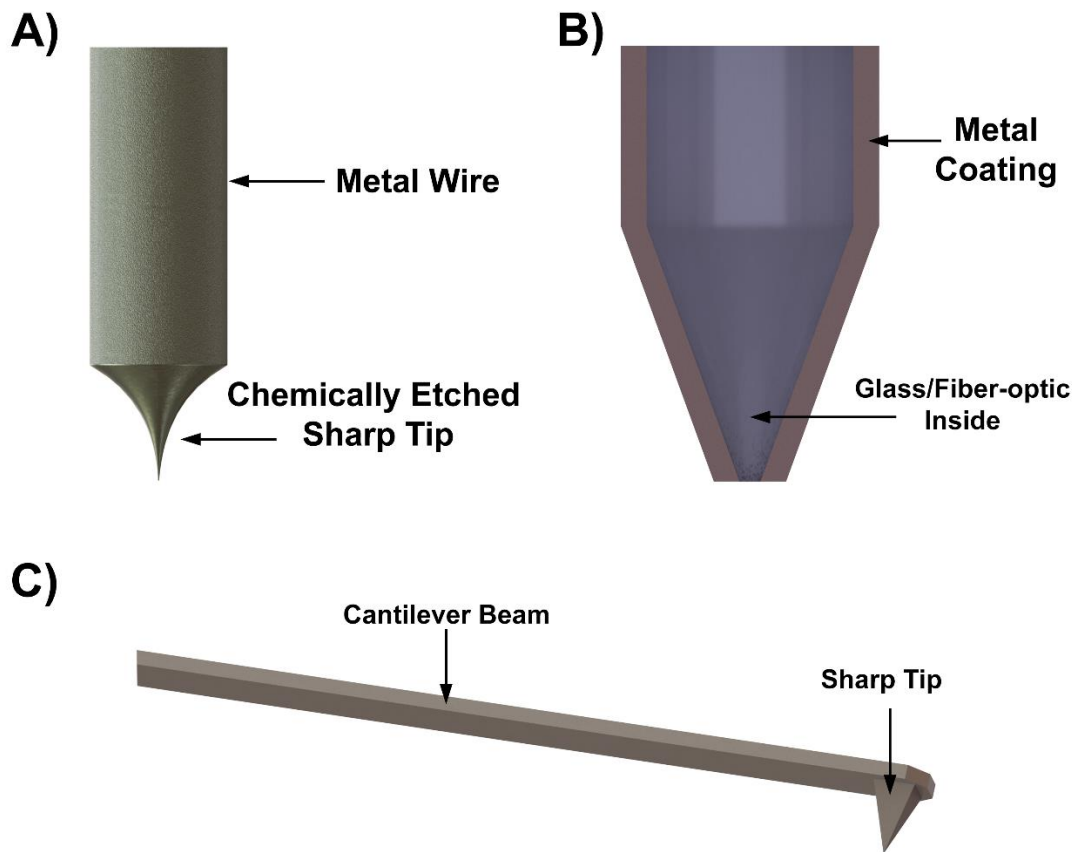


**Figure 1.2** Some example SPM probe illustrations; (a) an STM tip, (b) cross-section of a SNOM tip and (c) an AFM cantilever.

### 1.1.2 Atomic Force Microscopy

As discussed in the previous section, AFM is a type of scanning probe microscopy invented by none other than the inventor of STM –Gerd Binnig– and his co-workers in 1986 [15]. In their paper, Binnig remarks that, in order to measure forces in atomic level, they propose to attach the scanning probe tip to a cantilever manufactured by simply gluing a piece of diamond to a thin gold lever, riding it on a sample surface and measuring the resulting deflection of the cantilever with STM. With this setup relying on physical *contact* rather than the quantum tunneling effect, not only conducting and semiconducting surfaces could be scanned (as is the case for STM), but any surface regardless of its electrical properties. As such, AFM allows topography measurements of any solid surface. It is not far-fetched to say that AFM was and still is a revolutionary instrument. With relatively cheap and simple setups, it is possible to obtain very high resolution topography images, force-distance curves, *etc.* from nearly any sample.

Although the basic idea remained the same, over a brief time period the initial design of AFM changed with more simple, cheap and efficient probes and detection methods which made the instrument more resourceful than ever [16].



**Figure 1.3** Illustration of a model piezoelectric tube scanner. 4-cylinder-sliced piezoelectric elements are used for the actuation in  $x$  and  $y$  coordinates and one concentric cylindrical piezoelectric part for actuation in  $z$  direction.

All typical atomic force microscopes consist of similar parts to operate, although different operation modes may require different electronics or hardware. First of all, since AFM is part of the scanning probe microscopy, AFM needs a probe to operate. A typical AFM uses a very sharp tip (ideally one atom sharp at the end) attached to a micro-machined cantilever which acts as a soft spring to be deflected by tip-sample interaction forces. AFM cantilevers are generally manufactured by using common micro-fabrication techniques like photolithography and etching. Although, cantilevers manufactured can be later coated by many different materials, silicon and silicon nitride are very common materials to manufacture AFM cantilevers from.

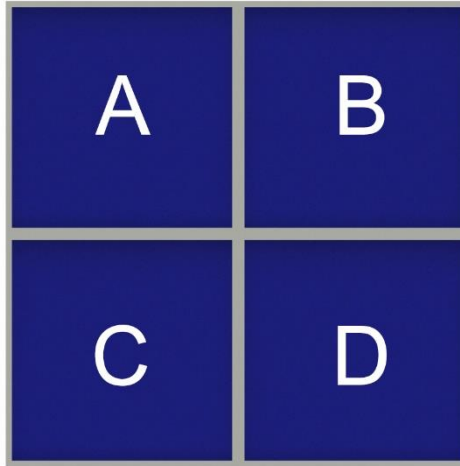


**Figure 1.4** Illustration of a model photo detector that consist of four independent photo-diodes. Individual photo-diodes are marked with different letters.

As discussed before, AFM detects surface forces by measuring the deflection of the cantilever that holds AFM probe. Although the first AFM used STM for deflection detection, there are many other ways that are being used to measure cantilever deflection (i.e. laser interferometer, capacitive detection). The most common way of measuring cantilever deflection is using a laser and photo detector system. A laser beam reflected onto a photo detector that consist of four independent photo diode (Figure 1.4) can measure very small cantilever deflections. In resting position, the laser reflecting from the cantilever falls in the middle of the photo detector creating no difference in readings of photo diodes. However, any deflection of the cantilever in the normal direction would cause the laser spot to go up or down thus creating a voltage difference between the upper part of the photo detector and its lower part. Therefore a tiny deflection in the cantilever would break the center alignment of the laser spot and hence get detected. Deflection of the cantilever can be quantified with the following equation:

$$\theta = \psi ((V_A + V_B) - (V_C + V_D)) \quad (1.1)$$

where  $\theta$  is the deflection of the cantilever,  $\psi$  is some calibration constant that correlates voltage to deflection and  $V$  values are the voltage readings of photodiodes respective to their sub-indices.

With the described subsystems above, a cantilever with a sharp tip as a scanning probe, an optical detector and a piezoelectric scanner, more or less a very basic AFM can be

thought of (see Figure 1.5). Different operation modes of AFM require different types of controller systems and may require additional hardware. For instance; many operating modes of AFM require an oscillating cantilever and thus include a piezoelectric actuator that oscillates the cantilever, while contact mode operation does not require such hardware. Likewise, while a simple tip-sample distance controller is enough for some operating modes, some other operating modes may require more complex controller circuitry. However, the parts discussed above are the basic parts that are common to more or less all AFM designs.

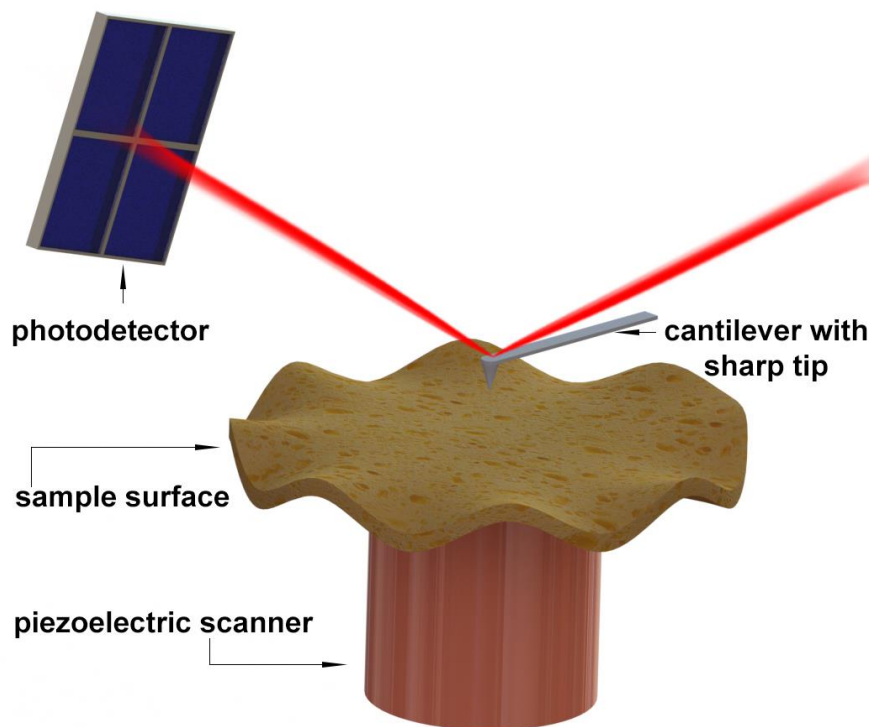


**Figure 1.5** A sample AFM illustration with a photodetector, cantilever and piezoelectric scanner.

AFM can be used in many different operating modes for different purposes. However, the first mode invented was the contact mode. Being the first mode ever invented and the simplest one, contact mode set a basis for the other AFM modes. Yet, since it is still relevant and commonly used, it makes sense to describe the contact mode first. In the contact mode AFM, cantilever and the sample surface are in physical contact in a conventional sense; the tip and the surface are in a repulsive regime of interaction. Due to repulsion between cantilever tip and the surface, the cantilever beam gets deflected

in the normal direction. Detecting deflection values during scanning gives quite a good idea about surface topography. This process can be imagined as a blind person reading the *Braille* alphabet with his fingers. Although this simple mechanism is quite useful for detecting surface topography, it can be damaging to the tip or the sample due to uncontrolled repulsive interaction forces. With the addition of a simple distance controller loop, damage can be significantly reduced. The cantilever base can be approached or retracted from the surface in order to keep a constant set force value, which is directly proportional to the deflection of cantilever. In this method, the cantilever base tracks the sample surface and directly delivers a topography map. The contact mode of AFM is also beneficial in other experiments, for instance the characterization of mechanical properties of the surface. With a well-characterized cantilever, the AFM tip can be pressed into the surface and a force-distance curve can be recorded. With the help of force-distance curves, the elasticity of surfaces can be easily determined. In addition to the surface characterization, contact mode of AFM is widely used in the manipulation of surfaces, characterization of friction, and nanolithography. In addition to its ease and wide range of use, contact mode AFM can also be used in any desired medium like ambient, vacuum and liquid.

Other common modes of the AFM (in addition to contact mode) can be classified as “oscillating modes”. Due to their common use in research; tapping and non-contact modes of the AFM will be introduced in this section. Tapping mode is one of the most widely-used AFM mode available. In this mode, a sinusoidal oscillatory vibration is provided to the cantilever, usually with the help of a piezoelectric actuator at the base of the cantilever mount. Rather than being in contact with the sample constantly, bouncing on top of the sample up and down and “tapping” on it intermittently yields better results with mechanically delicate samples, such as biological ones. Not having continuous contact with sample and not applying a constant shear force during scanning (as is the case in contact mode) reduces the chance of damaging fragile samples. In addition, tapping mode is also less effected by capillary forces acting under ambient conditions. Under ambient conditions, most surfaces are covered with a very thin water layer. Although this layer usually passes unnoticed in our daily lives, it creates a huge difference in small scales. During contact mode, capillary forces may *trap* the tip over

the surface or mask actual interactions with the sample. Intermittent contact provided by tapping mode also overcomes capillary issues [14].

Non-contact mode of the AFM (NC-AFM), is quite self-explanatory in terms of basic principle. In NC-AFM, a cantilever with an oscillation amplitude smaller than a few nanometers gets very close to the sample surface but never physically touches it. The only interactions between the sample and the tip are relatively small van der Waals and chemical forces in the attractive regime. These weak attractive interactions cause a reduction of the effective resonance frequency of the cantilever which can be detected and locked on to. Since NC-AFM detects weak interatomic interactions, the main use of the NC-AFM is in getting true atomic-resolution images of surfaces and detecting interatomic and intermolecular forces. This delicate process is usually conducted under vacuum in order to achieve best resolution with high quality factors and to reduce the chance of “blunting” the tip apex via contact with the sample surfaces through capillary forces.

## **1.2 Molecular Dynamics**

Molecular Dynamics (MD) is the study of physical movements, behaviors and interactions between atoms and molecules. Usually, atomic interactions between atoms and molecules are calculated from their potentials and trajectory of the atoms in the systems are determined by solving Newton’s equations of motion by various numerical methods. Predicting, interpreting and experimenting with complex atomic structures with many bodies provides essential benefits to chemistry, physics, biology and many other fields. With MD techniques, the behavior of molecules, their shape and size; near other molecules or in other environments and under different temperature conditions can be examined and predicted with accurate, quantitative results. MD simulations are quite popular due to their flexibility and success at predicting molecular structure and thermodynamic properties of molecular systems [17]. The significance of MD simulations and work is also recognized by the Nobel Prize. In 2013 Karplus, Levitt and Warshel received a Nobel Prize in chemistry for their work in “development of multiscale models for complex chemical systems” which includes MD approaches [18].

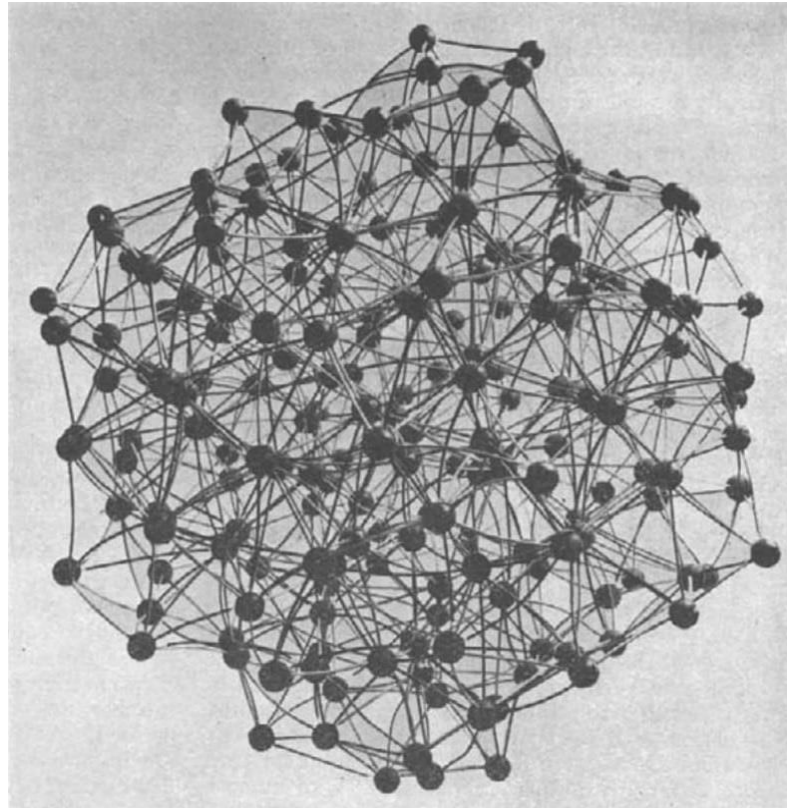


**Figure 1.6** One of the macroscale liquid models built by J. D. Bernal in late 50's [19].

Even before the widespread usage of computers in academia, MD-like simulation ideas were in researchers' minds and the building of macroscopic models of atoms and molecules were done by researchers. For instance, Bernal investigated the structure of liquids and neighboring atoms in liquids using rubber balls and sticks (see Figure 1.6) in his work published in *Nature* in 1959 [19]. In his paper, Bernal mentions the first MD works happening in the very same years and states his hopes regarding the adaptation of his work to computing machines used by Alder and Wainwrights. Bernal later mentions his macroscale liquid models and their challenges in his Bakerian Lecture in 1962 as: *"... I took a number of rubber balls and stuck them together with rods of a selection of different relative lengths ranging from 2.75 to 4 in. I tried to do this in the first place as casually as possible, working in my own office, being interrupted every five minutes or so and not remembering what I had done before the interruption."* [20]. It can be said that MD as a valid scientific technique started in the beginning due to the work of Alder and Wainwright in late 50's [21], [22] which are also mentioned by Bernal in that time. In their work, Alder and Wainwright simulated atoms as perfectly

elastic hard spheres and modeled their collisions (see Figure 1.7). They extracted thermodynamic and dynamic properties of molecules from their model. After initial steps, MD developed fairly fast and started to spread more. There are some notable works just after Alder and Wainwright's work that developed more different and refined approaches. Work of Gibson et al. from 1960 that examines dynamics of radiation damage by a simulation of a copper block with the Born-Mayer potential model can be given as one of the earliest examples [23]. Later in 60's Rahman and Verlet published two famous papers in the area which are both using the Lennard-Jones potential. In 1964 Rahman published his study on dynamics and self-diffusion of liquid argon atoms which correlate quite well with experimental results [24]. In 1967, Verlet published his paper on fluidic and thermodynamic properties of argon atoms [25]. This paper is also quite significant because Verlet's time integration algorithm which is frequently used even today, is introduced in this paper.

MD is a resourceful tool to investigate physical movements, behaviors and interactions between atoms and molecules. From the introduction of the concept to today, it is commonly used by itself as a study of physics or with experiments to provide a better understanding of underlying sources and causes that yield experimental results. Regardless of the area, MD is a powerful and a resourceful tool that can show different probable structures and interactions of molecules in any environmental condition which may not be easily (or ever) achieved in a controlled laboratory environment.

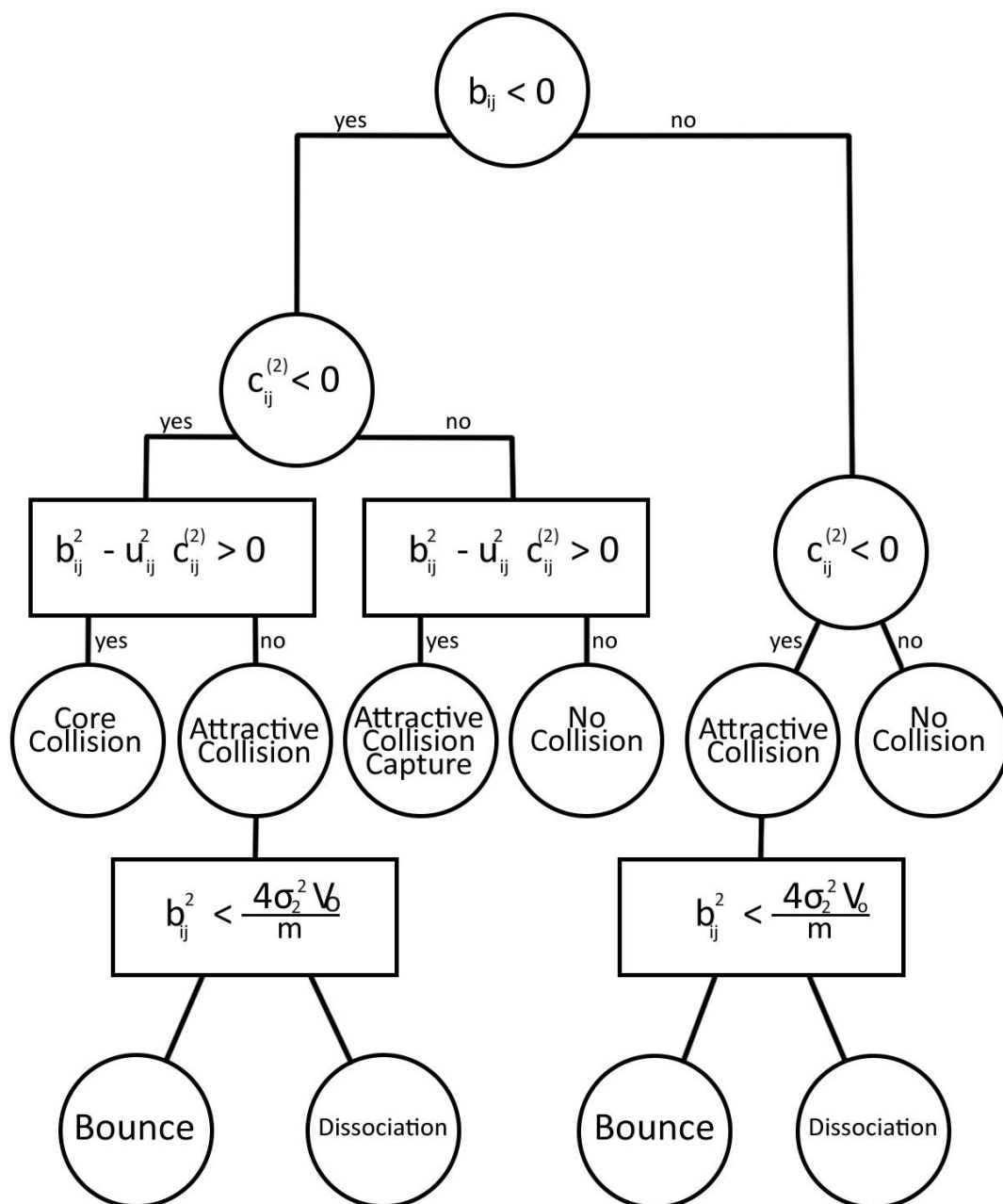


**Figure 1.7** Logical computation sequence used in Alder and Wainwright's work published in 1959. Image reproduced from the referred paper [22].

### 1.2.1 Basic Principles of MD

Majority of molecular dynamics work can be considered in the scope of classical mechanics that relies on Newton's equations for motion and the assumptions that let individual atoms to be treated with Newton's equations of motion. First of these

assumptions can be stated as the “Born-Oppenheimer approximation”. In this approximation, electrons of the atom moves instantaneously with movement of the nuclei and nuclear coordinates and trajectory of the atom can be assumed as a systems coordinates. Furthermore, forces acting on the atoms can be expressed with potential energies which only depends on the position of the nuclei. Those potentials can be assumed to involve (i) fairly complex equations to solve, like time-independent version of the Schrödinger’s equation for electronic variables which are used in *ab initio* MD methods which also considers quantum mechanics and electronic structure of the atoms to build classical/quantum hybrid approaches to treat system with a classical approach and use quantum mechanics to model interactions in small sites, or (ii) fairly simple pre-defined empirical potentials which are commonly used and yield generally successful results [17], [26]. Thinking the atoms as a point masses with no quantum properties but with a potential energy depending on their coordinates gives us freedom to apply Newton’s laws of motion to them. By knowing mass properties of the atoms and deriving forces acting on them from the associated potential energies, their acceleration and hence velocities, momenta and positions can be determined. With this approach, equations of motion of the  $i^{th}$  atom in an N-atom system can be written with the Newton’s second law:

$$m_i \frac{d^2 r_{ix}}{dt^2} = -\frac{\partial U}{\partial r_{ix}}, \quad m_i \frac{d^2 r_{iy}}{dt^2} = -\frac{\partial U}{\partial r_{iy}}, \quad m_i \frac{d^2 r_{iz}}{dt^2} = -\frac{\partial U}{\partial r_{iz}} \quad (1.2)$$

Where  $m_i$  is the atomic mass,  $r_{ix}$ ,  $r_{iy}$  and  $r_{iz}$  are Cartesian coordinates and  $U$  is the atomic potential that is defined according to set system. Hence trajectories of atoms can be calculated. Like any other set pf differential equations, initial conditions of atoms acceleration, velocity and position should be set beforehand.

As mentioned before, many studies of MD use empirical potentials that depend on the position of an atom. Those empirical potentials are also addressed as “force fields” or “interatomic potentials’ in different sources. Those empirical potentials represent quantum-mechanical and chemical interactions between atoms on a simplistic level. Those empirical energy functions are defined to fit with results of experimental data or quantum-mechanical calculations of very small and limited systems. Usually, defined energy functions include atomic charge, radius, bond length, angle and so forth. These

interatomic potentials can be investigated under two main headings: pair potentials and many-body potentials. Pair potentials can be described as a function which defines the potential energy between two interacting atoms. A simple example that can be given for pair potentials is the Coulomb potential that results from charge interactions;

$$E = C \frac{q_i q_j}{r} \quad (1.3)$$

Where  $C$  is the Coulomb constant,  $q_i$  and  $q_j$  are the net charges of interacting atoms and  $r$  is the interatomic distance. As one can see from the Equation 1.3, the interaction between two atoms get stronger as they get closer. If an attractive case is imagined, there is nothing keeping atoms from getting infinitesimally close to each other and forming a black hole or super condensed heavy mass considering only Equation 1.3. However, in real life no such thing happens due to the Pauli repulsion principle. As two atoms get close to each other their electrons in the shell starts to overlap therefore resulting in a very strong net repulsive force [17]. In order to include strong repulsion when atoms get too close to each other some of the researchers, especially in the very early MD work, used the hard sphere model. In the hard sphere model atoms are assumed to have a spherical shape which is allowed by the Born-Oppenheimer approximation. Furthermore, those assumed spherical shapes have *rigid* walls which are impenetrable. Therefore we can add a repulsive  $\psi$  term to the calculated potential which is defined in Equation 1.4 where  $\sigma$  is assumed the rigid sphere diameter and  $r$  is the interaction distance.

$$\psi(r) = \begin{cases} \infty ; r < \sigma \\ 0 ; r \geq \sigma \end{cases} \quad (1.4)$$

Although the hard sphere approach is used in many studies and applicable to many cases, most of the pair potentials includes a rapidly increasing repulsive term which mimics the Pauli repulsion principle. Using a potential with a repulsive region term prevents discontinuities in the potential function, as is the case in the hard sphere model. Hence using pair potentials with a repulsive term results in smoother potential-distance graphs. For example, the very commonly used Lennard-Jones potential that consists of two parts as can be seen in Equation 1.5: one attractive term that scales with  $r^{-6}$  and one repulsive term that scales with  $r^{-12}$  (see Figure 1.8).

$$E = 4\epsilon \left[ \left( \frac{\sigma}{r} \right)^{12} - \left( \frac{\sigma}{r} \right)^6 \right] \quad (1.5)$$

$$E_{total} = E_{LJ} + E_{Coul} \quad (1.6)$$

Furthermore; the two given examples –Coulomb and Lennard-Jones potentials– also can be combined in necessary cases, as has been done in literature [26], [27] (see Equation 1.6).

### Lennard-Jones Potential Between Two Atoms

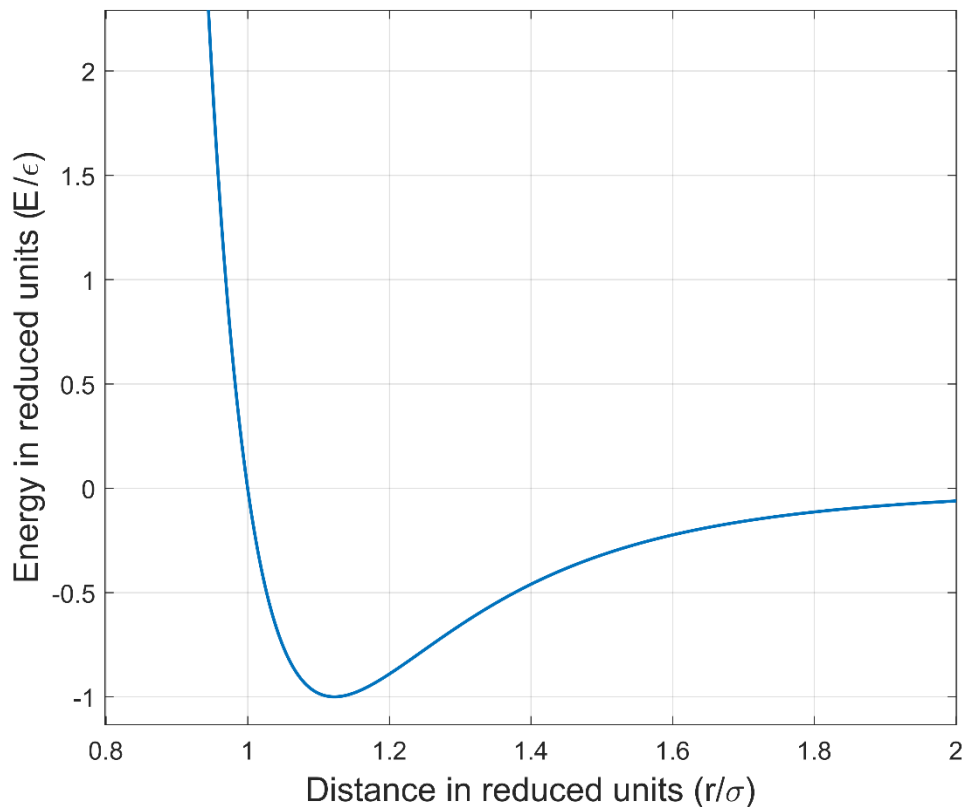


**Figure 1.8** Lennard-Jones interaction between two generic atoms in reduced units. As can be seen from the figure, when the distance reaches the  $1.12\sigma$  value, the repulsive part of equation starts to dominate the attractive part and in the distance of  $\sigma$ , the potential energy reaches zero (equilibrium point).

Many-body potentials are generally used to model chemically bonded or more complex structures like biomolecules. In those potentials, interaction distance is not sufficient to define a potential energy for an atom. In addition, angle bonds, dihedral angle bonds and so forth may be required to successfully define a potential that represents the simulated system. With introduction of angles and dihedrals, chemical bonding of trios,

quartets, and quintuples or more atoms may be incorporated to define correct structures. Some potentials may consider a more detailed geometry or may just be a pair potential that also considers a close neighbor third atom [17]. Some of the notable examples of many body potentials are given below.

**Embedded Atom Model:** Embedded atom model (EAM) is widely used while modeling metallic structures and metallic alloys. EAM contains a pairwise potential of an atom with neighboring atom and also considers electron cloud density of neighboring atoms. Potential is calculated with the Equation 1.7 where  $r_{ij}$  is the distance between atom  $i$  and  $j$ ,  $\phi_{ij}$  is a short range pair potential between atom  $i$  and  $j$ ,  $\rho_{h,i}$  is the host density which is approximated by the sum of all the neighboring atoms' atomic densities (see Equation 1.8 where  $\rho_j^a$  is the contribution from the density of atom  $j$ ) and finally  $F$  is the embedding potential energy which is a function of  $\rho_{h,i}$  [28], [29].

$$E_{tot} = \sum_i F_i(\rho_{h,i}) + \frac{1}{2} \sum_{\substack{i,j \\ i \neq j}} \phi_{ij}(r_{ij}) \quad (1.7)$$

$$\rho_{h,i} = \sum_{j(\neq i)} \rho_j^a(r_{ij}) \quad (1.8)$$

**Tersoff Potential:** Tersoff potential is a pairwise potential with an attractive term that is affected by the neighboring environment and bond structures which considers multi bodies. In Tersoff potential, the total potential energy of a system and a bond energy are defined as in Equations 1.8 and 1.9 ( $E_{tot}$  is total energy,  $V$  is bond energy,  $f_R$  is repulsive pair potential,  $f_A$  is attractive pair potential,  $f_C$  is a smooth cutoff function that stops calculation after a cutoff to manage computational resources and  $b_{ij}$  is the measure of bond order that is introduced by Tersoff in his 1998 journal paper [30]). Tersoff potential is generally used for silicon, carbon, diamond structures and may be suitable for hydrocarbons [31].

$$E_{tot} = \sum_i E_i = \frac{1}{2} \sum_{i \neq j} V_{ij} \quad (1.9)$$

$$V_{ij} = f_C(r_{ij})[a_{ij}f_R(r_{ij}) + b_{ij}f_A(r_{ij})] \quad (1.10)$$

**Adaptive Intermolecular Reactive Empirical Bond Order:** Reactive Empirical Bond-order (REBO) potential uses a variation of Tersoff potential that is specifically

developed to model covalent bonds of carbon-carbon interaction and hydrocarbons. However, due to the absence of dispersion and non-bonded repulsion terms; REBO potential is not a good fit for some solid-state materials (like graphene and graphite), some hydrocarbons, liquids and thin films. Therefore in 2000, Stuart proposed some additions to the REBO potential and proposed Adaptive Intermolecular Reactive Empirical Bond Order (AIREBO) which essentially adds the REBO potential to the Lennard-Jones potential (in some cases Morse potential which is called AIREBO-M) and a torsional potential and be written as [32];

$$E = \frac{1}{2} \sum_i \sum_{j \neq i} [E_{LJ} + E_{REBO} + E_{torsional}] \quad (1.11)$$

Interatomic potentials are one of the key elements of an MD simulation. There are many different empirical and semi-empirical potentials that have different strengths and weaknesses in different aspects. Therefore choosing a suitable potential for a given study is crucial and choosing an improper model may lead to undesired and unrealistic systems and results.

So far, trajectories of individual atoms and their position-dependent potentials that result in forces have been discussed. Another essential part of MD simulations is the “time integration”. With the time integration, trajectories of the individual atoms and their new potential energies according to their new positions are calculated. The most common way of integrating an MD system is the Verlet time integration method that was proposed in 1967 [25]. The Verlet algorithm can be put on the paper basically as;

$$r_i(t + h) = r_i(t - h) + 2r_i(t) + \frac{1}{m} \sum_{j \neq i} f(r_{ij}(t))h^2 \quad (1.12)$$

Where  $t$  is time,  $h$  is the time increment,  $r$  is the position of the atom,  $f$  is the interatomic force and  $m$  is the atomic mass.

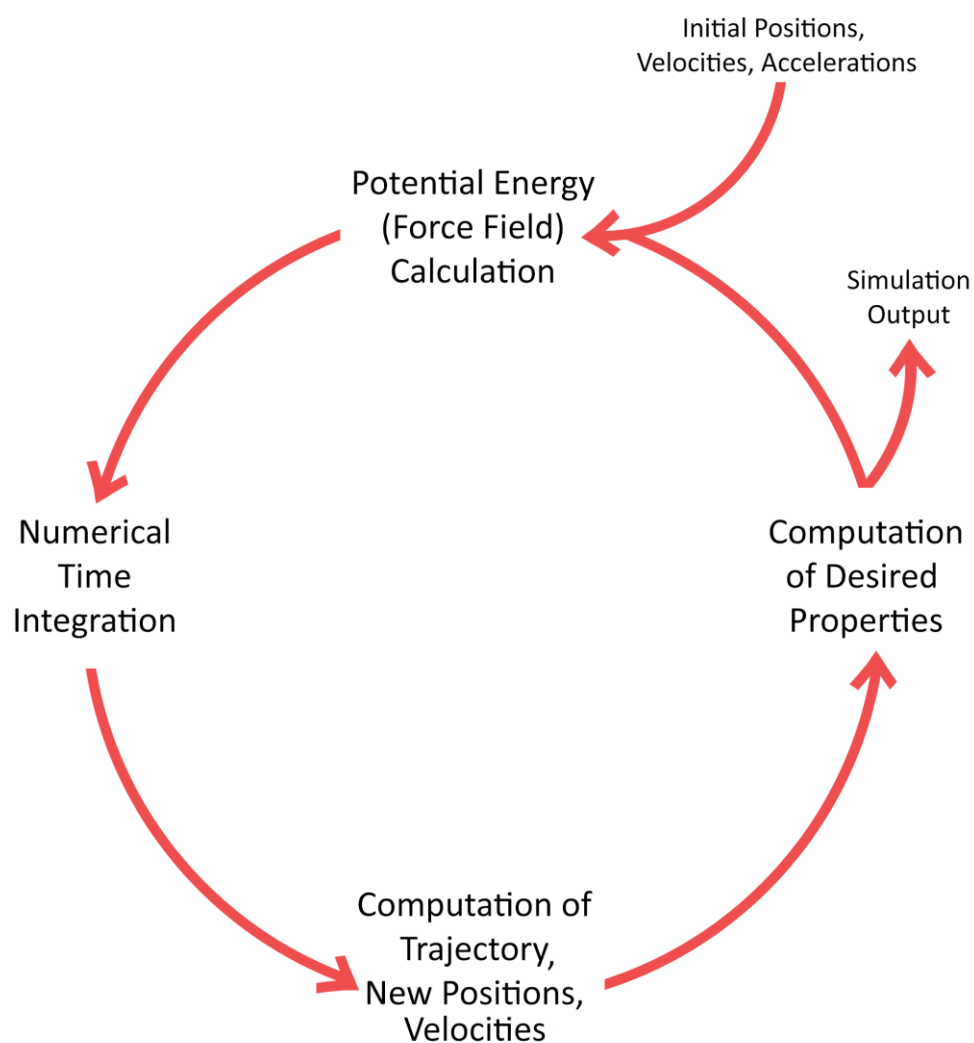


**Figure 1.9** A flowchart that shows a very basic running algorithm of a MD process.

### 1.2.2 Applications of Molecular Dynamics

As discussed before, MD has many applications in various areas of chemistry, physics, biology and so forth. In the beginning, MD work got popular in materials for obvious reasons. Not long after, MD works were applied to biophysics and biochemistry to mostly examine binding sites and structures of proteins. Especially with the-quantum mechanics-combined approach of *ab initio* MD, it was possible to successfully simulate chemical interaction sites. MD simulations are used on a wide scale, essentially from

theoretical physics to biological applications. Some examples in different areas are briefly presented here in order to demonstrate applications of MD and its wide range.

As mentioned above, one of the very first journal articles that employs MD was the work done by Alder and Wainwright which investigates phase transition of argon atoms modeled as hard spheres. In their first publications with MD, they published their phase transition predictions with 108 and 32 particles alongside Monte Carlo simulations conducted by their colleagues which agrees with their results [21], [33]. The association and disassociation mechanisms they published in their later work that explains the MD technique they used can be seen in Figure 1.7 [22].

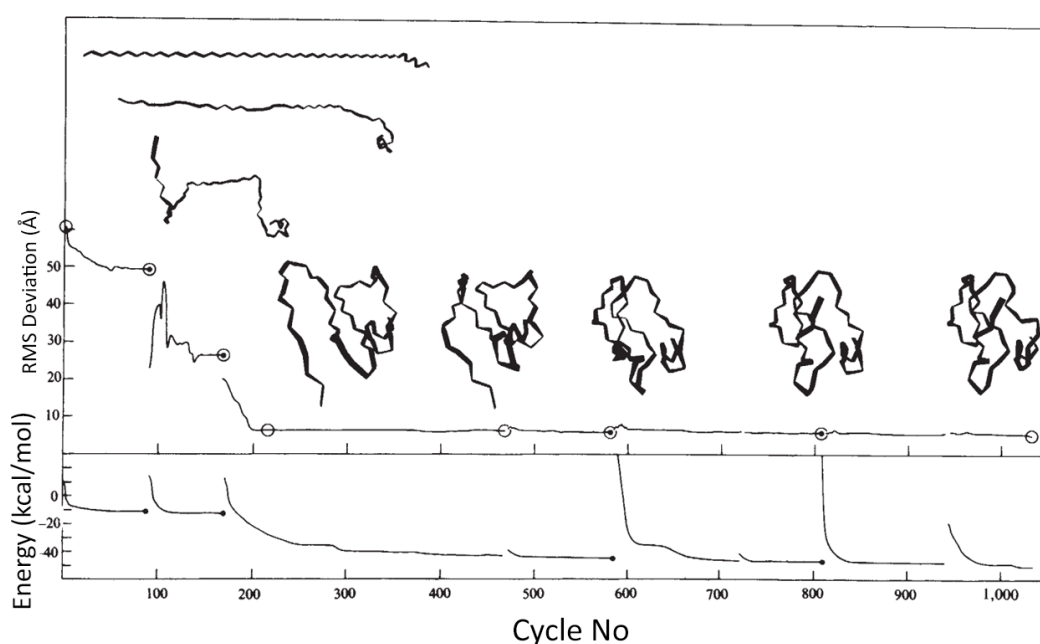


**Figure 1.10** Results of protein folding experiments done by Levitt and Warshel. Image has been reproduced from their 1975 Nature paper [34].

In 1975 Levitt and Warshel (both 2013 Chemistry Nobel Prize Laureates for their MD work) published a paper in Nature about computer simulations of protein folding. In their work they simplified protein chains to be represented by two C atoms and reduced the degree of freedom of amino acid residues to one. They modeled their system's potential with a simple Lennard-Jones potential. They minimized the potential energy of linked chains in a damped environment and applied thermal vibrations in cycles as minimization process completes [34]. One of their plots showing their results can be seen in Figure 1.9. Their work's significance not only comes from its accuracy but from

the fact that it is one of the first biological works done with MD. Furthermore it should be considered that their work has been done before Tersoff's work on potentials which yield result better with hydrocarbon structures, and yet got accurate results.

Another example of MD work in a different area is water adsorption and its effects. Hu and Sun examined the disjoining pressure effect in an ultra-thin water film on gold surface [35]. They prepared a gold sandwich with a thin water layer in-between. They modelled their system with using different potential models according to their system's needs. They used EAM for calculating the potential between their gold walls and TIP4P-Ew model for water-water molecule interactions. They modeled gold-water interactions with Lennard-Jones and Spohr potentials. Their MD work supported the results coming from classic disjoining theory from adhesion and showed that neither out-of-plane nor in-plane ordering of water films has a big impact on disjoining pressure.

MD simulations are also widely used to interpret tribology and friction experiments. For instance Ye et al. investigated load-dependent friction hysteresis on graphene [36]. They modeled a silicon dioxide AFM tip and multi layers of graphene. In addition to vacuum simulation, a water droplet between surfaces also modeled to simulate ambient conditions. In the work, the Tersoff potential was used in tip atoms and AIREBO was used to model graphene layers. TIP4P potential is used to calculate the potential between water molecules. Interaction between tip, graphene, and –if present– water was modeled with the Lennard-Jones potential. A snapshot from their simulations can be found in Figure 1.11.

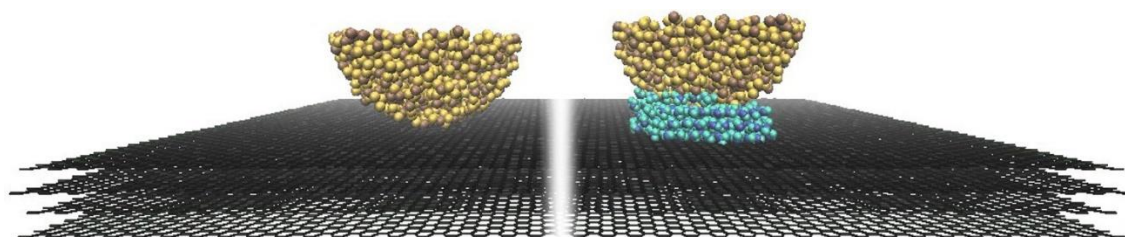


**Figure 1.11** Image taken from Ye et al.'s work [36]. On the left, three layers of graphene and silicon dioxide tip can be seen. On the right, there is an additional layer of water molecules between tip and sample.

Another fascinating example of MD use in biology involves modeling of a single complete satellite tobacco mosaic virus done by Freddolino et. al. in 2005 [37]. This simulation contained up to 1 million individual atoms and demonstrated the stability of the virus and its core RNA while demonstrating the instability of shell of the virus without its RNA and discussed physical properties of the virus, its assembly and infection mechanism. This work is still one of the MD simulations with the most particles simulated. A snapshot from their work can be found in Figure 12.

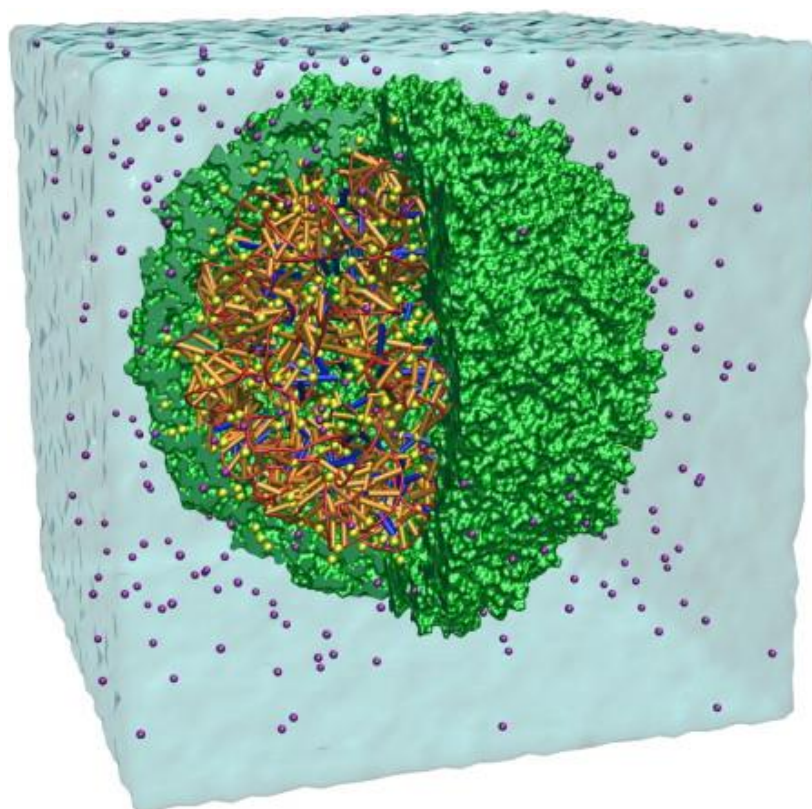


**Figure 1.12** MD simulation of a single satellite tobacco mosaic virus in liquid water environment. The side of the virus capsule is made transparent in order to demonstrate inside of the virus [37].

## Chapter 2

### Literature Survey

#### 2.1 Atomic Resolution Force Microscopy

Even the very first imaging work published by the use of the first ever AFM was able to demonstrate 1 Å vertical resolution under ambient conditions in contact mode [15]. Although this is quite enough to detect atomic steps in structures like graphite layers, it is typically not enough to obtain images of single atoms. Furthermore, using the contact mode of the AFM results in strong repulsive forces between the substrate and the tip and as such, has damaging/blunting effects on the tip apex (as mention in Chapter 1) which prevents atomic resolution or reproducible atomic resolution images. Therefore, in order to take atomic resolution AFM images, oscillating modes of the AFM that operate outside of the repulsive region are used [38]. Therefore it can be said that NC-AFM is commonly used for atomic resolution AFM imaging. In Chapter 1, NC-AFM is briefly introduced together with some other operating modes of the AFM. Since NC-AFM is considered in the scope of this thesis for atomic resolution AFM imaging, in this section it will be examined more thoroughly and some notable NC-AFM studies will be discussed.

Reproducible atomic resolution images have been achieved in the non-contact regime with the frequency modulation (FM) method [39]. To understand the physical mechanism behind frequency modulation, first of all dynamics of the cantilever should be investigated. In a simple view, the AFM cantilever can be assumed as a point mass with one degree of freedom with a forced harmonics oscillation (see Figure 2.1) [40]. Therefore we can write the natural frequency of the cantilever and the equation of motion for the cantilever as:

$$f_0 = \sqrt{\frac{k_{eq}}{m_{eff}}} \quad (2.1)$$

$$m_{eff}\ddot{z}(t) + c\dot{z}(t) + k_{eq}z(t) = F_{int}(z(t)) + F_{exc}(t) \quad (2.2)$$

where  $z$  is the deflection of the cantilever from resting point,  $c$  is some damping coefficient,  $F_{int}$  is interaction force between AFM tip and substrate which is distance dependent,  $k_{eq}$  is the equivalent spring constant of the cantilever and  $F_{exc}$  is excitation force externally provided to the cantilever, typically via a piezo actuator. Although the cantilever has a natural resonance frequency of  $f_0$  introducing another term that is dependent on the deflection changes effective spring constant of the system. Therefore the systems' natural resonance frequency shifts from the cantilever's natural resonance frequency. With Equation 2.2, when a cantilever is excited in  $f_0$  there will be a phase difference of  $\frac{\pi}{2}$  between input excitation and output response. However, when the system's effective natural frequency is changed due to interaction between tip and sample, this phase difference changes to some value other than  $\frac{\pi}{2}$ . In FM-AFM, the phase difference between input excitation and the cantilever response is set to  $\frac{\pi}{2}$  which aims to provide an excitation corresponding to the system's natural frequency. This aim is achieved by using a phase-locked loop (PLL) to detect and control the oscillation of the cantilever (see Figure 2.1). Output of the Voltage-Controlled Oscillator (VCO) component of the PLL generates a clean sinusoidal wave with constant phase shift matching to cantilever response. Therefore, many AFM systems use VCO output to drive the AFM cantilever (see Figure 2.1a). But the AFM cantilever can also be driven with a phase shifter and an automatic gain controller, without using the VCO output (see Figure 2.1b) [41].

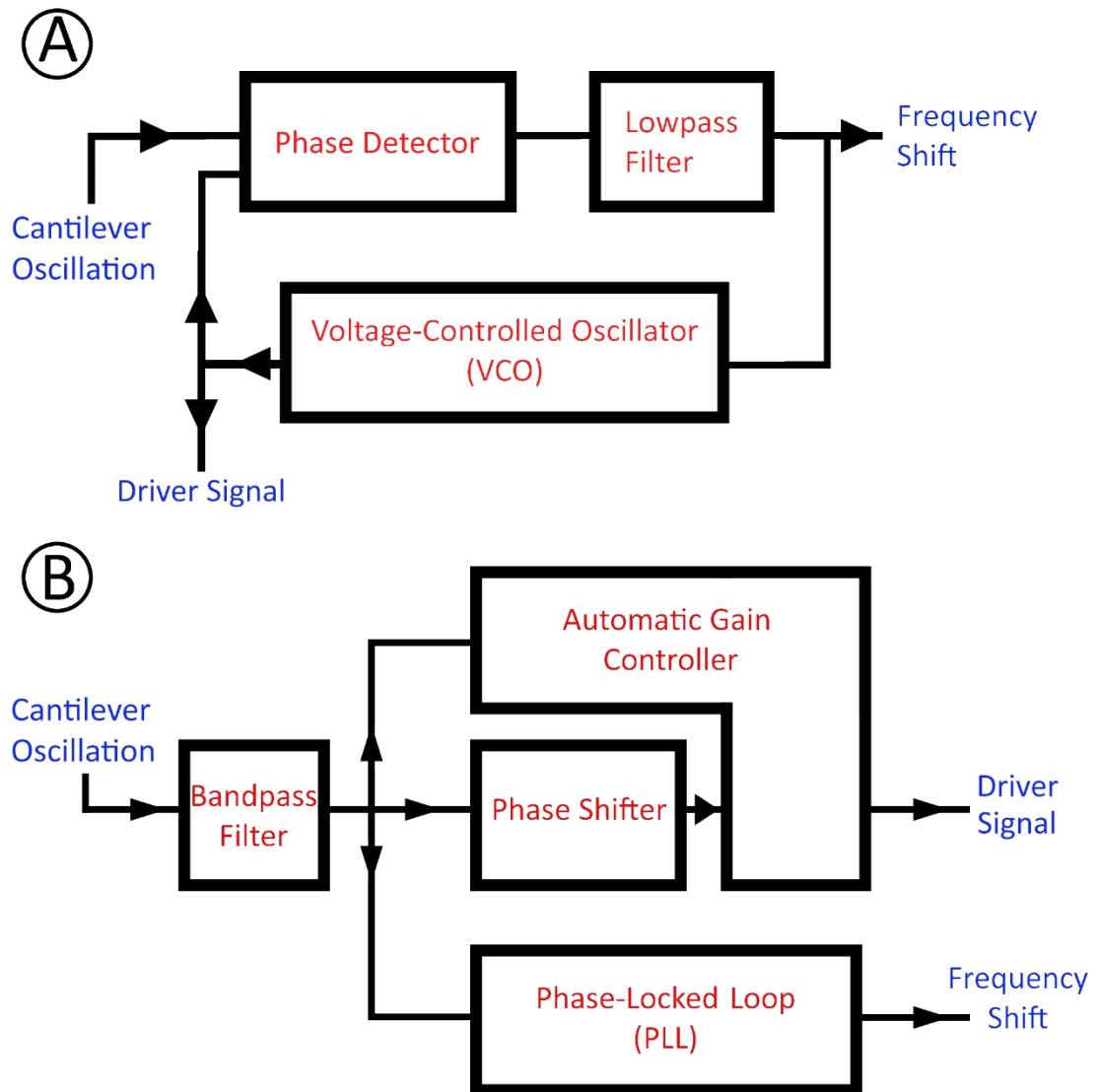


**Figure 2.1** (a) Block diagram of a Phase-Locked Loop (PLL). (b) Block diagram of a typical FM-AFM. Cantilever deflection signal is fed to a bandpass filter in order to filter the noise out. Phase-shifter shifts cantilever response by  $-\frac{\pi}{2}$  to get the desired phase difference between input and output. Automatic gain control sets oscillation amplitude to a desired value and PLL provides frequency shift information [41].

By setting a fixed frequency shift value and changing the obtained frequency shift to bring it to the set value by making the cantilever come closer to or further away from the surface in the  $z$  direction during scanning, the cantilever base is made to precisely track the surface. By keeping record of the  $z$  position of the cantilever base, atomic resolution topography maps are obtained (see Figure 2.2a). In 1995 Giessibl and

Kitamura & Iwatsuki separately managed to obtain atomic resolution images of the silicon (111) surface with the NC-AFM technique as described above [42], [43]. In his work in 1995, Giessibl used a cantilever beam with 17 N/m stiffness & 34 nm oscillation amplitude and scanned a Si (111) surface in ultra-high vacuum (UHV). With this setup Giessibl was able to image the 7×7 unit cell of the Si (111) surface with its defects (see Figure 2.2b). The image taken was a reproducible image and portions of the image where individual atoms in their unit cell structure and their defects are non-visible are attributed to where the AFM tip got contaminated or lost its sharpness. Over time, the technique has improved greatly. For instance in 2006, Sugimoto et al. imaged the Sn/Si (111) alloy surface with a similar setup (silicon cantilever with 20 nm oscillation amplitude and 30.5 N/m stiffness in UHV environment, see Figure 2.2c) [44]. While imaging with silicon cantilevers, relatively high oscillation amplitudes are preferred for atomic resolution, because large oscillation amplitudes prevent jump-to-contact and possible instabilities [41]. However, using a quartz tuning fork setup with a metallic tip provides small but stable oscillation amplitudes due to high stiffness. Oscillating the tip with a small oscillating amplitude provides more sensitivity to short-range chemical interactions. Therefore, obtaining higher resolutions and getting images of molecules adsorbed on other surfaces is made possible. For instance, with this technique Pawlak et al. investigated C<sub>60</sub> molecules adsorbed on the KBr (001) surface [45]. In their work, KBr surfaces, their step edges and C<sub>60</sub> structures on KBr can be clearly seen with a topography scan (Figure 2.2d,e). They also investigate adsorbed C<sub>60</sub> molecules with constant height mode, which will be discussed later in this chapter. It can be seen that the oscillation amplitude used in their work (0.15 nm) is significantly lower than oscillation amplitudes used by both Giessibl in 1995 (34 nm) or Sugimoto et al. in 2006 (20 nm).

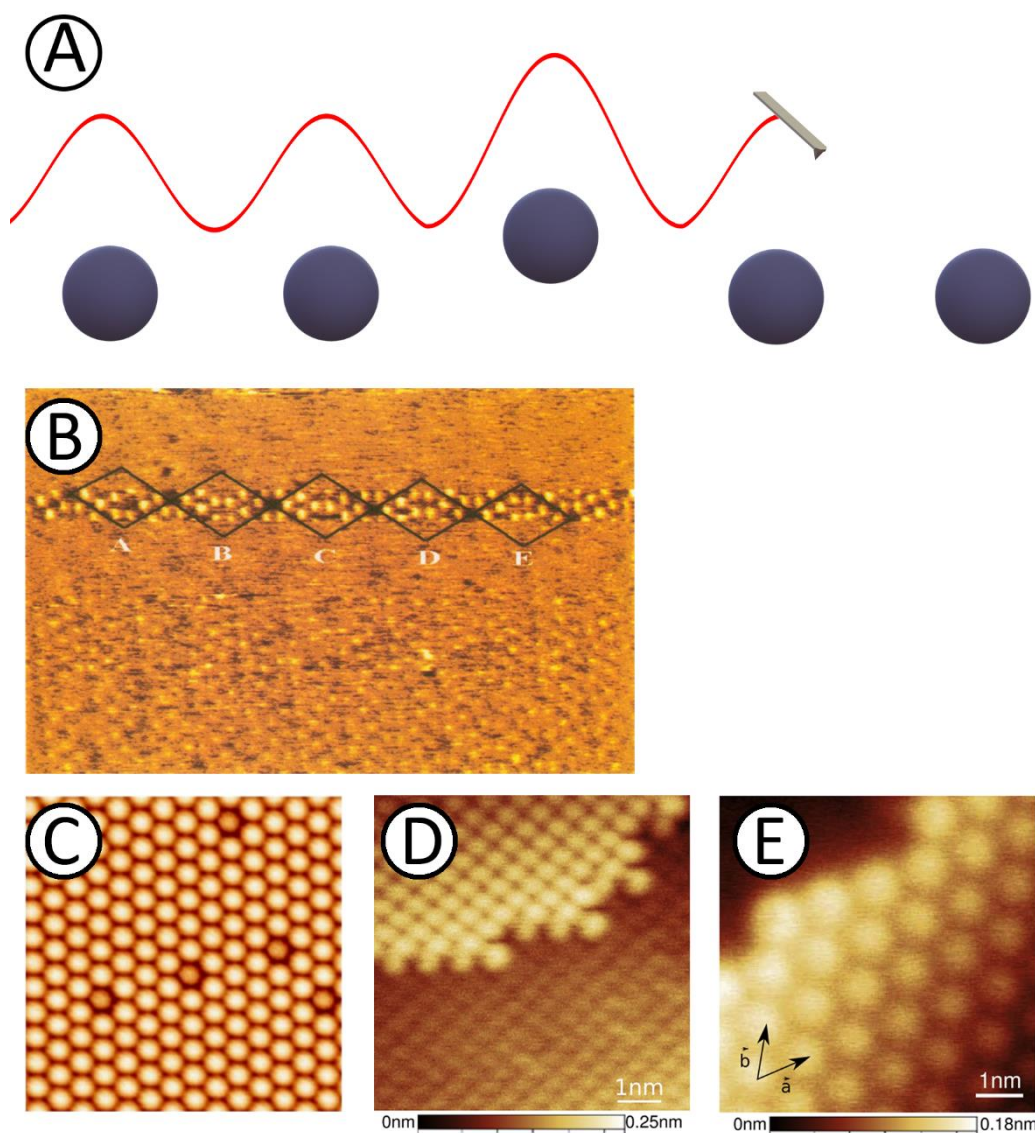


**Figure 2.2** (a) Representative illustration of a cantilever tracking a surface with atomic resolution. (b) Topography image of the Si (111) surface obtained with the-NC-AFM technique. In unit cell “A”, a misplaced atom (which is a defect) can be seen (34 nm oscillation amplitude and 17 N/m cantilever stiffness) [42]. (c) Topography image of the Sn/Si (111) alloy surface (20 nm oscillation amplitude and 30.5 N/m cantilever stiffness) [44]. (d) Topography image of the KBr (001) surface with a visible step edge (0.15 nm oscillation amplitude and around 1800 N/m cantilever stiffness) [45]. (e) Topography image of C<sub>60</sub> molecules adsorbed on KBr (001) surface (0.15 nm oscillation amplitude and around 1800 N/m cantilever stiffness) [45].

Obtaining frequency shift data provides information about the interaction force between tip and the surface. By keeping the cantilever base at a constant height, conducting a scan in  $x$  &  $y$  directions and recording values of frequency shift in positions yields a frequency shift image. Although NC-AFM technique in constant height mode is pretty straight forward and simple, it is used widely to yield successful atomic resolution images of surfaces and even individual molecules. Work done by Gross et al. in 2012 is a good example of high resolution constant height NC-AFM images of single molecules [46]. In their work, Gross et al. took images of several different molecules using NC-AFM images in constant height mode. They were able to measure bond lengths of molecules in their experiments (see Figure 2.3). In the work, Gross et al. functionalized their AFM tip with a CO molecule and took constant height NC-AFM measurements of different molecules that contains carbon-carbon bonds. They demonstrated different bond orders from different molecules. They used fullerenes adsorbed onto the Cu (111) surface, Hexabenzocoronene molecule adsorbed on the Cu (111) surface and dibenzo(cd,n)naphtho(3,2,1,8-pqra)perylene (DBNP) molecules adsorbed on bilayer NaCl which is supported by a Cu(111) surface. Apart from having very high resolution NC-AFM measurements of small molecules, oscillation amplitudes used during the experiments also stands out. Oscillation amplitudes used in the work are lower than a mere 1 Å, down to even one third of 1 Å. As mentioned before, in order to prevent instabilities or the jump-to-contact effect, relatively higher oscillation amplitudes are chosen during typical NC-AFM experiments using relatively soft silicon cantilevers. However, using high stiffness tuning fork systems cantilever instabilities can be overcome and using very low oscillation amplitudes becomes possible. Hence, with lower oscillation amplitudes, the cantilever-surface interaction becomes more sensitive to short range interactions which leads to higher resolution in NC-AFM measurements.

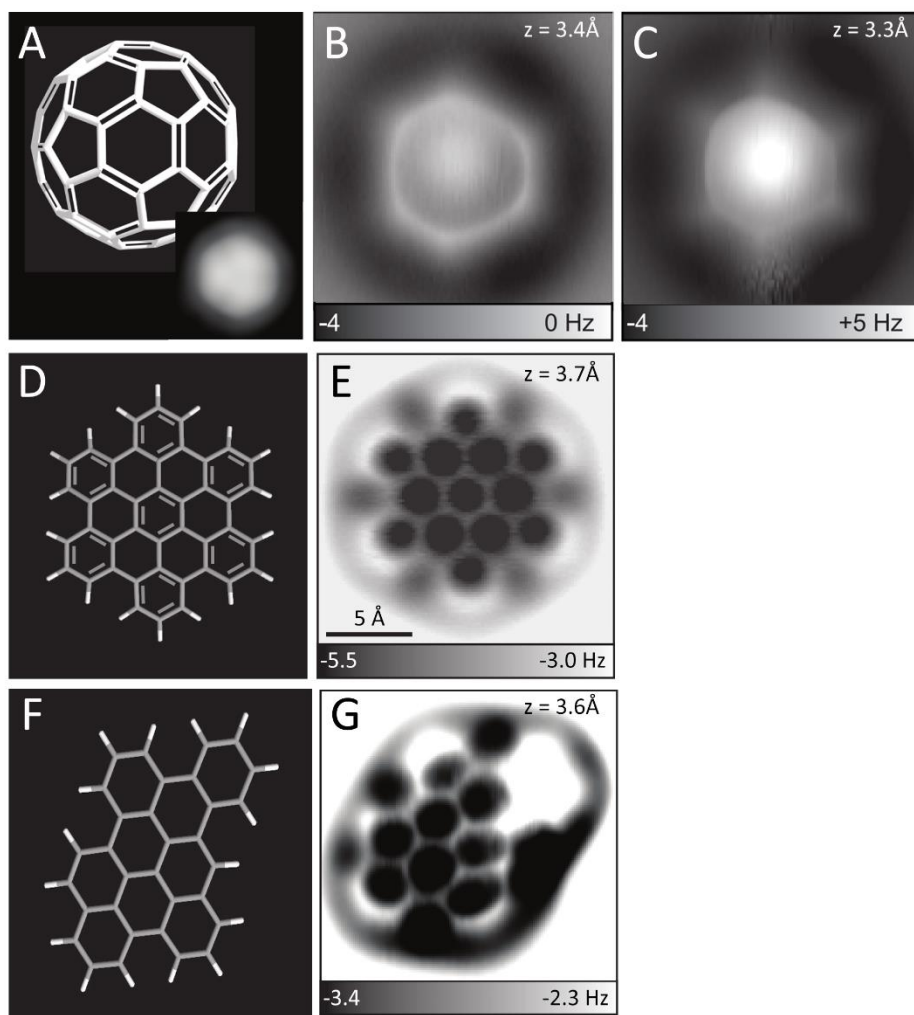


**Figure 2.3** (a) Illustration of  $C_{60}$  molecular model, together with an STM image (b, c) Constant height NC-AFM measurements of  $C_{60}$  molecule at different heights. Height is denoted on the images with  $z$ . Oscillation amplitude is  $0.36 \text{ \AA}$ . (d) Illustration of Hexabenzocoronene model. (e) Constant height NC-AFM measurements of Hexabenzocoronene molecule. Oscillation amplitude is  $0.35 \text{ \AA}$ . (f) Illustration of DBNP model. (g) Constant height NC-AFM measurements of DBNP molecule. Oscillation amplitude is  $0.48 \text{ \AA}$ . Images reproduced and put together from the work of Gross et al. [46].

While constant height mode of NC-AFM is quite successful, it has certain disadvantages. One of the most important disadvantage of the constant mode is the lack of a topography tracking mechanism which may cause crashing the tip into the surface or getting away from the surface during the experiments due to, e.g., thermal drift. This

problem can be overcome by using a very slow response topography controller which cannot respond to changes of the tip-surface interaction on the atomic scale but can respond on longer time scales which makes the cantilever track the sample surface in general and hence prevents any crash or withdrawal over extended measurement times. By using this “quasi-static” constant height NC-AFM mode, Bechstein et al. managed to image the (110) surface of titanium dioxide (in its *rutile* phase) and capture both bridging oxygen atoms and underlying titanium atoms in 2009 [47]. STM images on the very same surface are sensitive to unoccupied states at titanium and defect sites and thus left bridging oxygen sites invisible. NC-AFM techniques, on the other hand, were able to image both bridging oxygen atoms and titanium atoms underneath [48]. An illustration of the titanium dioxide (110) surface and a quasi-static constant height NC-AFM image can be found in Figure 2.4.

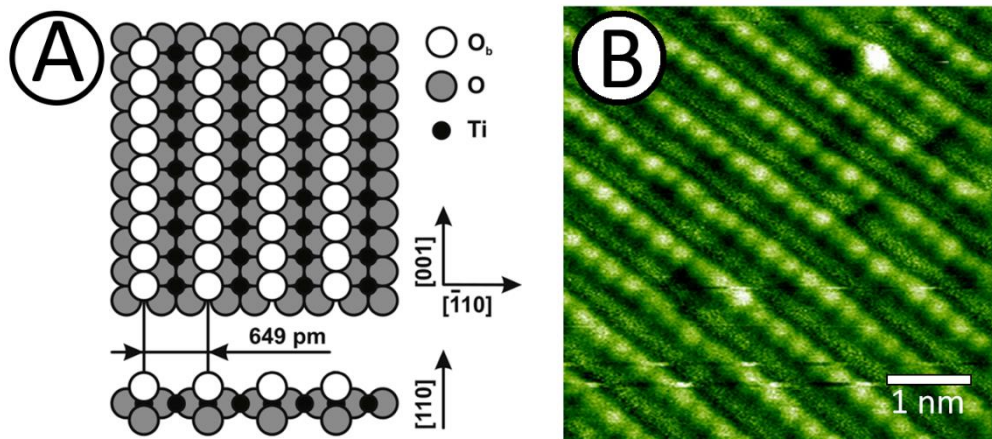


**Figure 2.4** (a) Illustration of the titanium dioxide (110) surface. (b) “All inclusive” NC-AFM image of the surface. Color scheme varies with frequency shift. Bridging oxygen atoms are detected as bright spots and titanium atoms form the less bright stripes between them. Both images are reproduced from the work of Bechstein et al. [47].

Frequency shift data obtained from NC-AFM can also be utilized to calculate the force and energy acting between the tip and the sample. Being able to convert frequency shift into force/energy constitutes another strength of NC-AFM. There are several ways to convert frequency shift information to interaction force/energy. However, the method by Sader and Jarvis is generally preferred due to its simplicity, validity for any

oscillation amplitude and accurate approximation [49]. According to the Sader and Jarvis method, the interaction force between tip and the sample in the  $z$  direction at a specific  $x$  and  $y$  position is given by:

$$F(z) = \int_z^\infty \left( 1 + \frac{\sqrt{A}}{8\sqrt{\pi(u-z)}} \right) \frac{\Delta f(u)}{f_0} - \frac{A^{\frac{3}{2}}}{\sqrt{2(u-z)}} \frac{d}{du} \left( \frac{\Delta f(u)}{f_0} \right) du \quad (2.3)$$

As one can see from the Equation 2.3; in order to be able to calculate force between tip and a sample at a given position, frequency shift values until the position where the interaction between sample and the surface becomes insignificant must be known. There are two approaches that to know frequency shift values. First approach is going to a specific location on the surface and doing “spectroscopy”, i.e., getting frequency shift values from NC-AFM by approaching to the surface gradually. With the data obtained by this method, interaction force between tip and a very specific site can easily calculated. The interaction energy can then be simply obtained by integrating the force data. The second approach is much more comprehensive and image-based rather than point-based. In this approach, constant height NC-AFM images are taken at different heights and therefore maps of the surfaces are obtained. Once many images from many different heights obtained; 3D, volumetric ( $x, y, z$ ) force maps can be calculated by their combination. For example, in 2010 Baykara et al. performed the layer-by-layer approach on the graphite surface and obtained 3D force maps from graphite surface [50]. In the work, Baykara et al. took 86 layers of constant height NC-AFM images using a tuning fork sensor with 2 pm intervals. Apart from obtaining force maps, also energy dissipation per cycle of the cantilever oscillation can be calculated via Equation 2.4 (where  $A$  is the oscillation amplitude,  $A_{excitation}$  is the excitation amplitude and  $Q$  is the quality factor) [50]:

$$E_{dissipation} = \pi k (A A_{excitation} - \frac{A^2}{Q}) \quad (2.4)$$

The 3D force map and some other data obtained from the work discussed can be found in Figure 2.5.

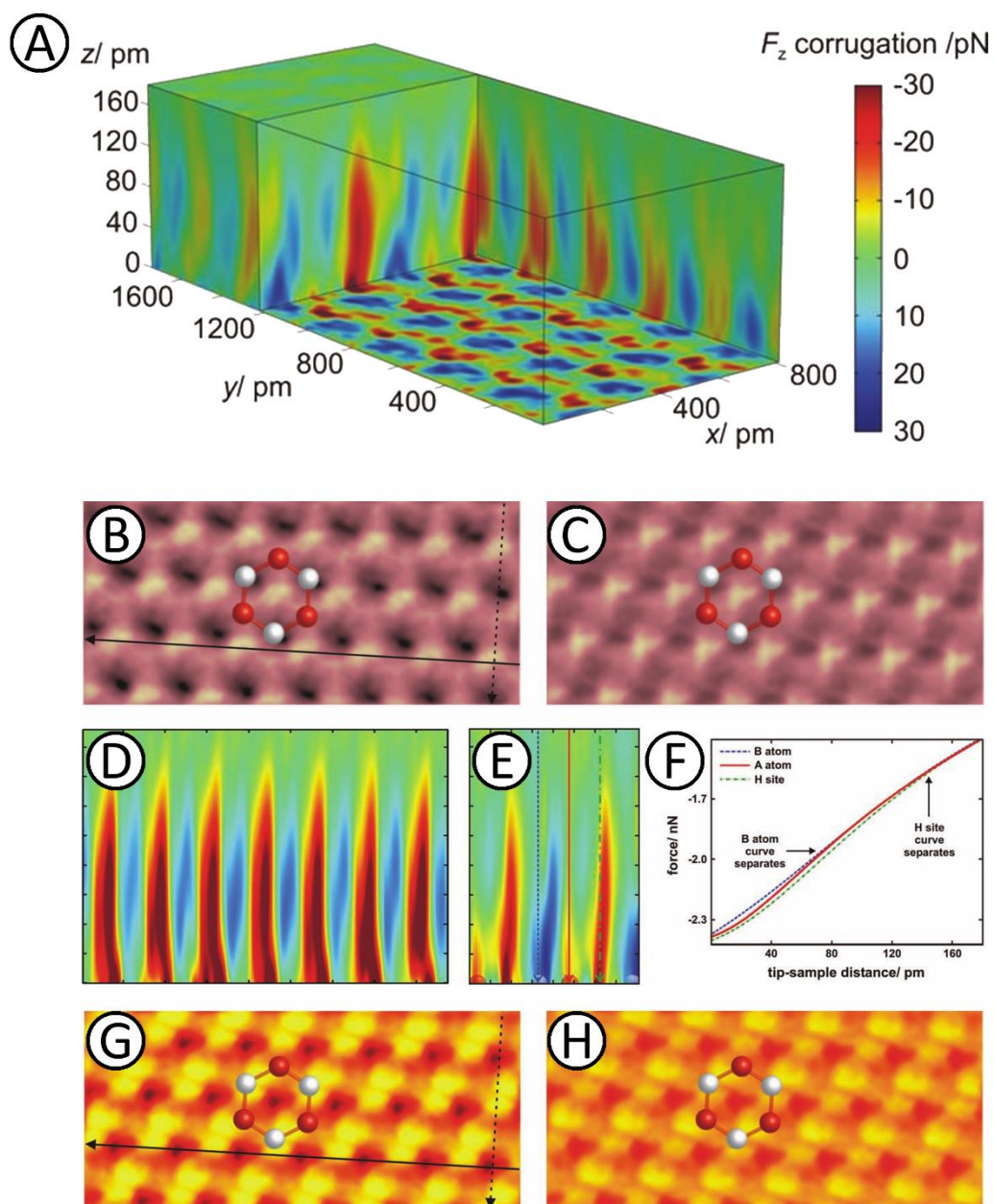


**Figure 2.5** (a) Representation of a 3D force field with atomic corrugation. (b) Force map at 12 pm distance. (c) Force map at 52 pm distance. (d, e) Vertical slices from the 3D force field in (a). (f) Three vertical force curves on two different types of carbon atoms and hollow site on graphite. (g) Energy map at 12 pm distance. (h) Energy map at 52 pm distance. Images are taken from work of Baykara et al. [50].

## 2.2 Molecular Dynamics Simulations

As discussed in the introduction section, molecular dynamics techniques are used for many different research areas. It is not surprising that molecular dynamics techniques are also widely used in SPM and NC-AFM studies. With the help of MD, the effects of energy dissipation, tip structure and elasticity effects on imaging, interactions at specific sites and many other phenomena can be investigated. Even the simplest approaches with MD techniques can provide insight into physical mechanisms in experiments.

In our previous works [51], [52], the effects of tip elasticity and asymmetry on NC-AFM and STM have been investigated with the help of interatomic force fields. In the first work [51], the effect of tip elasticity is investigated with a model single layer ionic NaCl surface and three-atom, 2D Pt tip with a single, charged end atom. Interaction between surface atoms and the tip atoms are modeled with the combination of Lennard-Jones potential and Coulomb potential. After obtaining LJ parameters for individual atom types (Na, Cl, Pt) from the literature, parameters to be used between specific interactions are calculated with Lorentz-Berthelot mixing rules, which are widely used in the literature. Lorentz-Berthelot mixing rules suggests that to obtain appropriate  $\sigma$  and  $\epsilon$  values, arithmetic and geometric means of the parameters of individual atom types should be calculated and used, respectively:

$$\sigma_{12} = \frac{\sigma_1 + \sigma_2}{2} \quad (2.5)$$

$$\epsilon_{12} = \sqrt{\epsilon_1 \epsilon_2} \quad (2.6)$$

In the study, the tip is assumed to have a lateral stiffness and lateral forces acting on the tip cause lateral deflections. With the deflection of the real tip position relative to the base position, vertical force maps obtained on the NaCl surface are structurally affected and the impact of the attractive sites increases proportionally with tip elasticity (Figure 2.6).

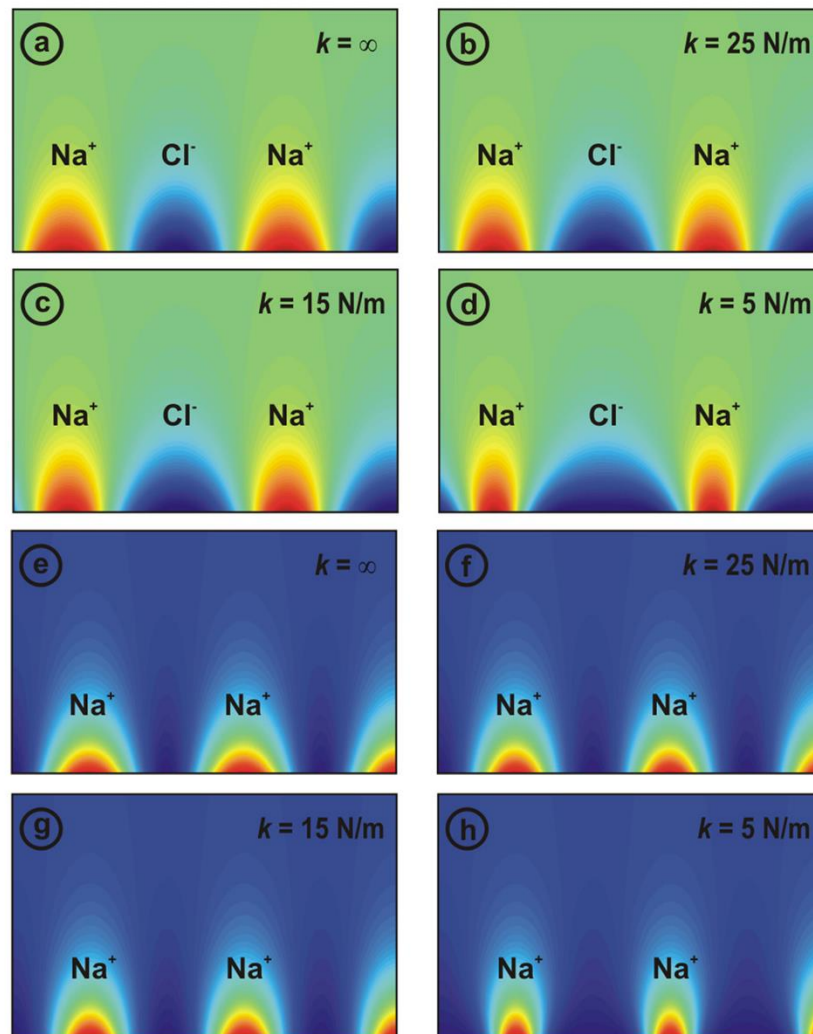


**Figure 2.6** (a) Vertical force maps calculated on the NaCl (001) surface with tips of varying stiffness. Images in (a-d) are calculated alongside the [100] direction and the images in (e-h) alongside the [110] direction. Apparent size changes of attractive and repulsive regions with stiffness can be observed. In color scale, red corresponds to repulsive, blue corresponds to attractive interaction. Image is reproduced from [51].

In the later work [52], a ten-atom pyramidal, 3D Pt tip and a two-layer graphene surface were modeled. In this work, the effect of tip asymmetry on NC-AFM and STM and related artifacts have been investigated. Tip symmetry is broken by rotating the pyramidal tip around front most atop. It can be seen from the results of the study that an asymmetric tip can break the apparent honeycomb symmetry of carbon atoms in the

images and make some atoms appear more attractive than others (Figure 2.7). In these studies, LJ interatomic potentials commonly used in MD studies are employed between tip and sample. However tips and surfaces were modeled as rigid bodies with no individual motion and internal interaction between atomic constituents. Hence, although these studies provides insight with simple approaches it would be more accurate to classify them as *molecular statics* than *molecular dynamics*.

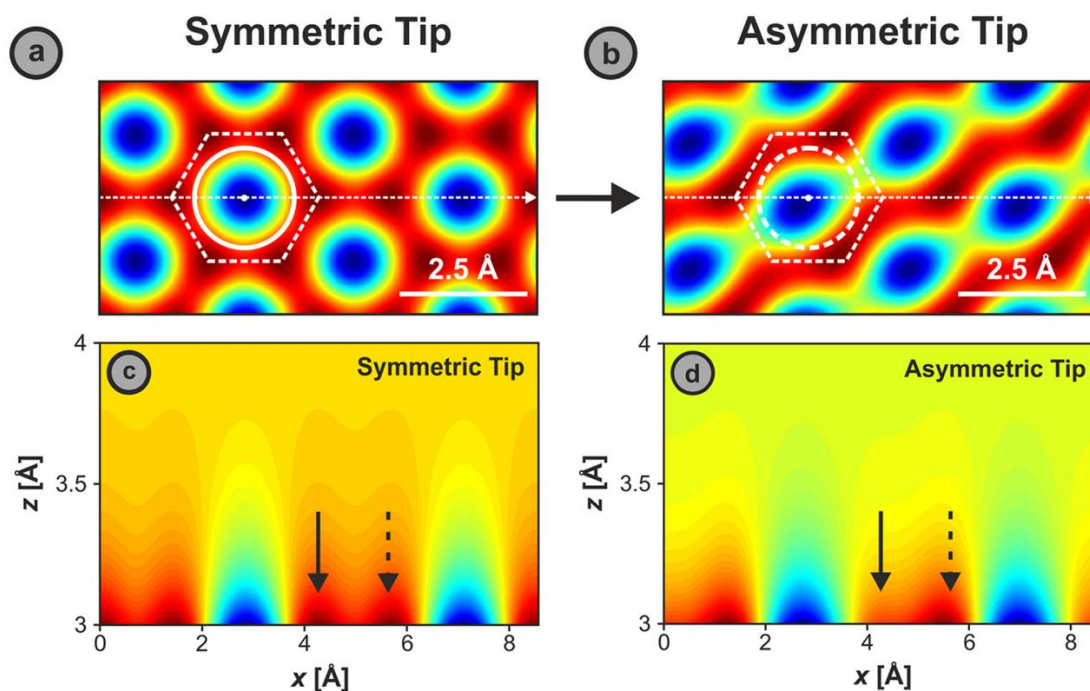


**Figure 2.7** (a-b) Horizontal force maps on obtained bilayer graphene surface with symmetric and asymmetric tips. Images in (c-d) are vertical force corrugation maps obtained along the white dotted lines in (a-b). Red sites correspond to less attractive regions whereas blue regions corresponds to more attractive regions. Image is reproduced from [52].

As discussed in the introduction chapter, “dynamics” is one of the essential features of molecular dynamics simulations. Without dynamics, the ability of the simulation to capture the experiments accurately decreases. While modeling a system in a finite box, energy input to the box and energy output from the box can change how closely the system mimics reality. Therefore, in addition to defining physical boundary conditions, defining thermo-dynamical boundary conditions are also important. Defining a

thermo-dynamical boundary condition is usually done by providing a group of atoms in the simulation some “thermostating” algorithms to control their velocities and hence their temperature. There are several ways and algorithms to apply a thermostating boundary to the system. Pishkenari and Meghdari’s work from 2010 is a nice example of a molecular dynamics study of NC-AFM to demonstrate thermostating [53]. In their work, Pishkenari & Meghdari created a 10 x 10 x 4 FCC lattice of gold atoms in (001) plane formation and a conic gold tip with 2 nm of length. After structurally building their system they applied physical and thermodynamic boundary conditions by dividing atoms into three groups. First, they created *frozen* atoms which absorb all the forces applied to them from other atoms and thus created a fixed layer around the physical boundaries of their simulation box. This layer consisted of 2 outer atomic layers of their cubic surface and the base of their tip. *Newtonian* atoms is another type of atom group created which were simply acting according to Newtonian equation of motion in response to interatomic forces applied on them. Finally, they’ve created a thermostating layer adjacent to the frozen layer. They applied two common thermostating methods together to their thermostat layers. First, simple velocity scaling. Velocity scaling is the simplest way of applying a thermostat to the simulations and is commonly used in different areas of MD [53]–[55]. Velocity scaling is just reducing velocities of the atoms according to a desired temperature value once every desired simulation step time. This scaling can be done instantaneously or can be done in a ramp fashion to achieve a continuity in particle velocities. Velocity scaling method does not impart an equation of motion to the particles. Hence equations of motion or the execution method is independent from damping. Second, the Nose-Hoover thermostat. In Nose-Hoover thermostat, an imaginary heat-bath is defined and taken into account while calculating the trajectory for *thermostated* atoms. An imaginary momentum coming from the defined imaginary heat sink acts like a dynamical friction force and hence decreases/increases the momentum of the particles according to temperature difference between particles and the imaginary heat sink. Since dynamic friction coefficients coming from Nose-Hoover have a Gaussian distribution, Nose-Hoover thermostat and integration also works fine for predicting small non-Newtonian systems [56], [57]. The 2D version of the model used by Pishkenari & Meghdari in their study can be seen in Figure 2.8 with different colors for different group of atoms.

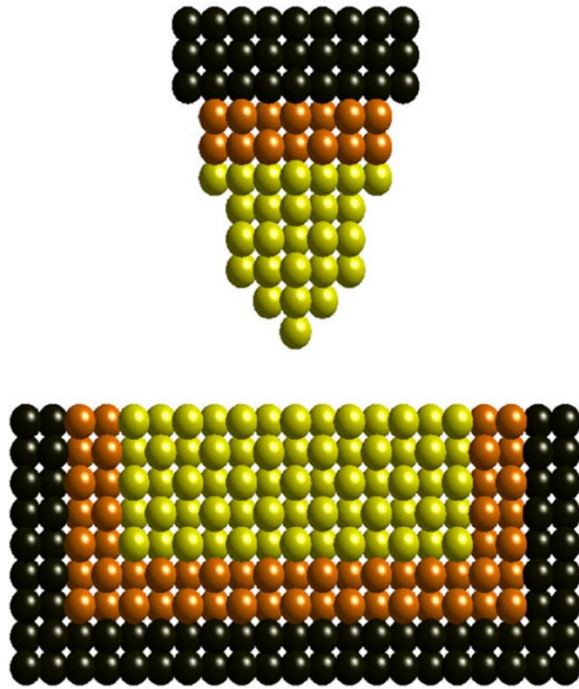


**Figure 2.8** 2D version of the tip-sample model used by Pishkenari & Meghdari in their study. Black spheres represent *frozen* atoms, orange spheres represent *thermostated* atoms and yellow spheres represent *Newtonian* atoms. Image is reproduced from Pishkenari & Meghdari’s work [53].

Although a thermostat layer is very commonly used in MD studies of NC-AFM, Klocke and Wolf simulated a small ionic tip on an ionic salt KBr surface without such a layer with good results [27]. In their work, an FCC ionic cubic surface and a rotated FCC cubic rectangular tip is used. Base atoms of the tip are defined with much higher masses than the other atoms of the tip which are much closer to the surface during simulation. After a relaxation time, running the simulation for a certain period in order to pass transient states, all the surface atoms of the surface cube which are not towards the tip are fixed to their positions, or “frozen” as denoted in Pishkenari & Meghdari’s work. As mentioned before, there is no defined thermostat region between fixed atoms and free atoms which are in Newtonian motion. Both Pishkenari & Meghdari and, Klocke & Wolf simulated a relatively small substrate surface and tip model with MD techniques and investigated their interaction, and then applied their oscillating cantilever model to these results. This is because including full extent of the AFM cantilever to the MD simulation is considered to be unfeasible.

Apart from the molecular dynamics perspective of the NC-AFM simulations, cantilever dynamics and simulation of controller electronics are also crucial and studied. As mentioned in the previous section of this chapter, motion of the tip of a cantilever can be modeled as a mass-spring-damper harmonic oscillator system with forced oscillation. Furthermore, controller schemes of NC-AFM are also briefly discussed in the previous section of this chapter. In 2006, Nony et al. published a paper on the simulation of an NC-AFM with high resemblance to real electronic schemes of PLL and amplitude controller of a frequency modulated system [58]. The controller scheme they used in the work can be found on Figure 2.9. In their model, the PLL of the electronics is not only used for frequency detection but also used for providing the driving (excitation) signal to the cantilever.

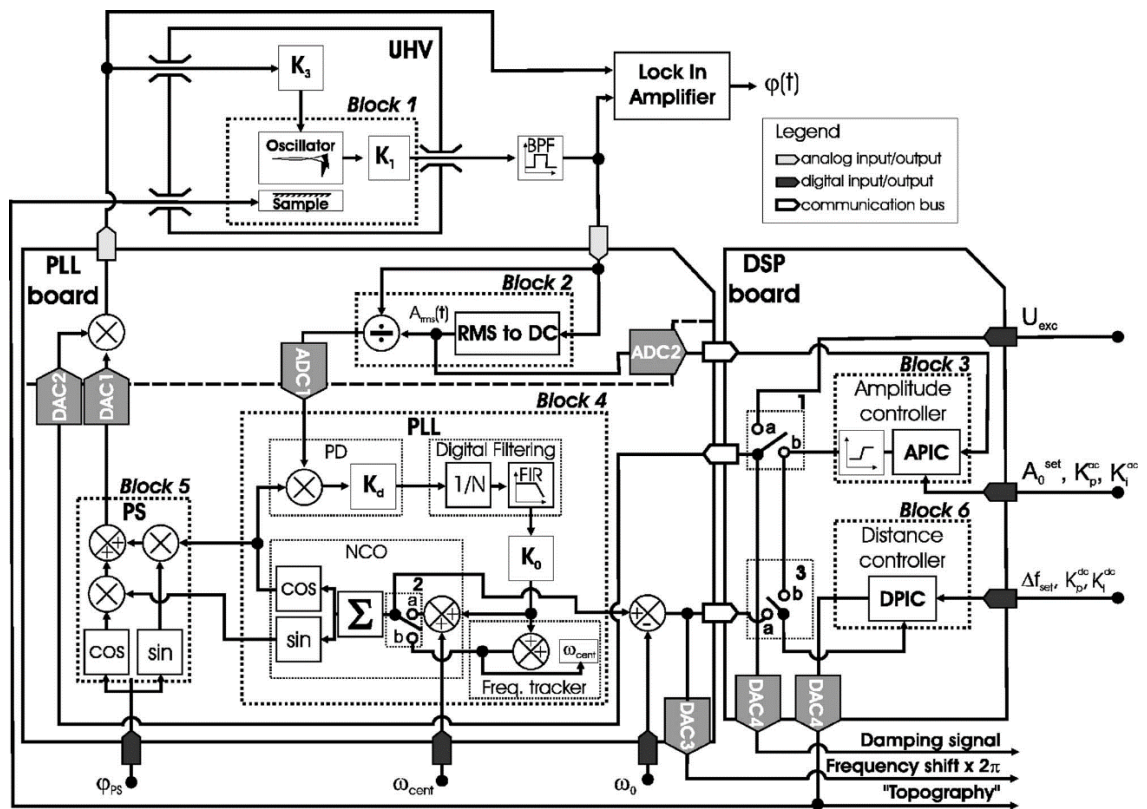


**Figure 2.9** NC-AFM scheme used in the work of Nony et al. published in 2006. Image is reproduced from reference [58].

# Chapter 3

## Methodology

### 3.1 MD Simulations

The MD simulation part of this thesis was coded and computed with LAMMPS (Large-scale Atomic/Molecular Massively Parallel Simulator) software [59]. LAMMPS is one of the most commonly used MD simulation software in academia. Interaction between a model graphene surface resting on bulk platinum with a platinum tip is modeled in order to simulate NC-AFM performed with a metallic tip on graphene. Hence, the system consisted of two types of elements: platinum and carbon atoms. Interaction between carbon and platinum atoms are modelled with the Lennard-Jones potential, interaction between carbon atoms are modeled with the AIREBO potential which is appropriate for modeling graphene and graphitic structures, and interaction between platinum atoms are modeled with EAM. Necessary and appropriate parameters required for the used interatomic potentials are taken from the literature [32], [60], [61]. Cut-off distance is set to 10 Å for simulation which is a reasonable cut-off value for selected interaction potentials. Integration of the time has been performed with the previously-introduced Verlet algorithm built in LAMMPS software with a time step of 0.001 ps.

For the geometric modeling of the surface, first coordinates for bulk FCC platinum are created by filling a  $40 \text{ \AA} \times 40 \text{ \AA} \times 16 \text{ \AA}$  space with platinum atoms according to FCC organization. Then, coordinates for a single-layer graphene surface of  $39.05 \text{ \AA} \times 39.05 \text{ \AA}$  are created according to appropriate dimensions and put on top of the (001) surface of the platinum with distance of  $3.3 \text{ \AA}$  (Figure 3.1).

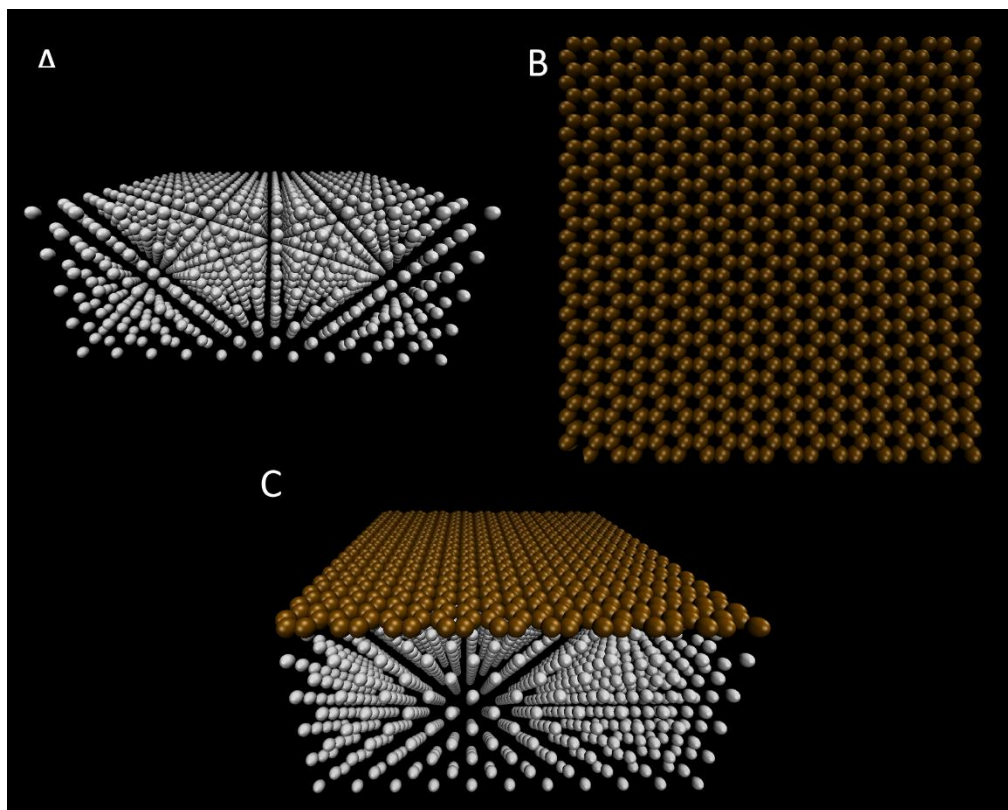


**Figure 3.1** Constructed model sample which consists of single layer graphene on top of bulk platinum. Platinum substrate, single-layer graphene and graphene on platinum can be seen in (a), (b) and (c), respectively.

In order to model the geometry of the platinum tip, a similar approach to creating the platinum surface has been followed. First a  $19 \text{ \AA} \times 19 \text{ \AA} \times 19 \text{ \AA}$  space is filled with platinum atoms according to the FCC configuration (Figure 3.2a). Subsequently, the tip cube is rotated around one of the corner atoms such that a model tip consisting of two pyramids attached together at their base is formed (Figure 3.2b). After rotation of the tip, tip atoms are relaxed without any thermostat or fixed atoms for 10000 simulation steps (10 picoseconds). After this initial relaxation of the tip, a realistic, sharp tip apex shape is obtained (Figure 3.2c).

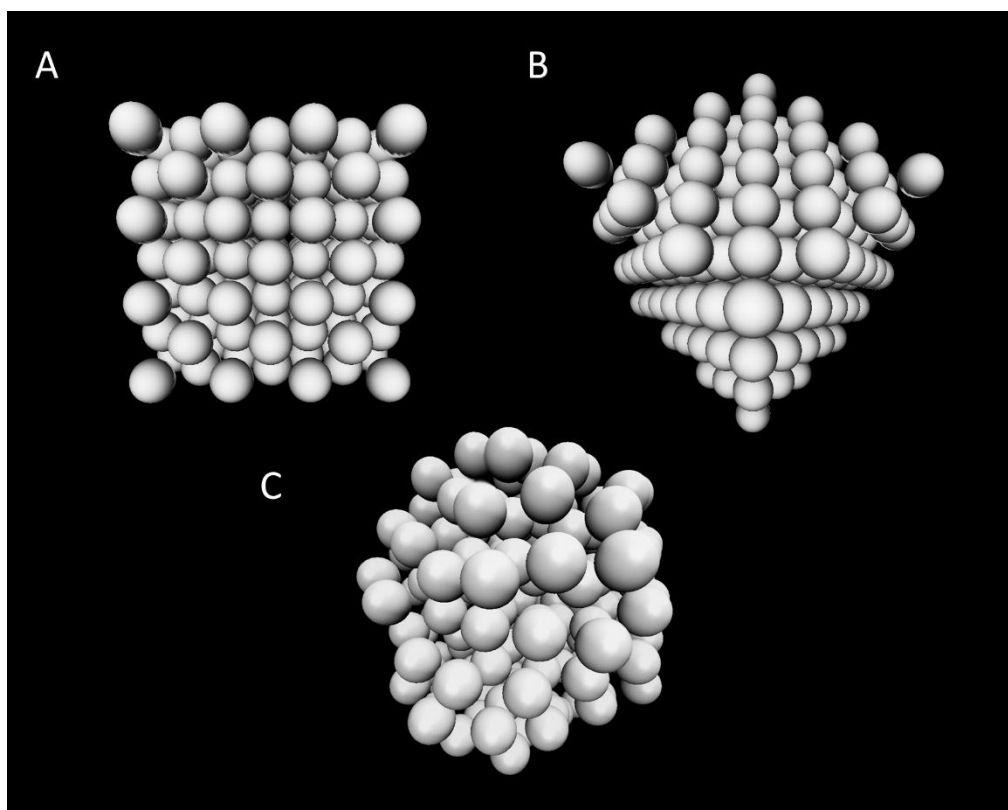


**Figure 3.2** Three stages of platinum tip construction. (a) Initial cubic structure. (b) Rotated version of the cube. (c) The tip after relaxation.

After constructing the sample substrate and the tip, the interaction forces are calculated in four different configurations: (i) Fixed Surface & Fixed Tip, (ii) Free Surface & Fixed Tip, (iii) Fixed Surface & Free Tip and, finally, (iv) Free Surface & Free Tip. In all of the configurations, a volume of  $8 \text{ \AA} \times 4 \text{ \AA} \times 7 \text{ \AA}$  is scanned in a layer-by-layer fashion along horizontal  $xy$  planes. In the  $x$  direction, data are acquired every 1 pm along the scanned  $8 \text{ \AA}$ ; in the  $y$  direction data are acquired every 5 pm along the scanned  $4 \text{ \AA}$ . Initial tip height is defined by the distance between the graphene surface and the foremost atom of the tip. Force maps are calculated every  $0.5 \text{ \AA}$ , between heights of  $2.5 \text{ \AA}$  and  $9.5 \text{ \AA}$ . Tip movement in the  $x$  direction is created by attaching an interactionless *ghost atom* with an imaginary rigid string to the very top atoms of the tip (which are fixed/immobile in all the configurations) and defining a movement speed to the created imaginary atom. Before the start of scanning, the tip and surface are relaxed for 100000 simulation steps, with a distance of  $9.5 \text{ \AA}$  between them.

The first configuration –Fixed Surface & Fixed Tip– is a pretty straightforward. None of the individual atoms are treated as independent moving particles and included in the equation of motion. The rigid tip was defined as the only moving body and the tip atoms are moved in the horizontal direction together as a body.

Understanding of the Free Surface & Free Tip configuration also provides understanding of the other configurations. In this configuration, free and individual motions of every atom is included in the calculations. In order to achieve more realistic conditions in the confined simulation box, some substrate and tip atoms are kept fixed (they defined the *physical boundary* of the system) and in order to simulate heat transfer to the outside environment, some atoms are defined as thermostated atoms, as discussed before (they constitute the *thermodynamic boundary*). Graphene atoms resting on the platinum surface are defined as free atoms with no constraints. Boundary conditions are applied to the supporting platinum structure and hence graphene, which is interacting with the model tip, is kept relatively undisturbed by this condition. In the platinum cube, 2 outer bottom and side layers are defined as fixed layers which are interacting with the other atoms but cannot move. Between the bottom fixed layer and the rest of the simulation, four layers of atoms are defined as thermostated atoms. Their trajectories are integrated with the rest of the free atoms but their velocities are scaled to 4 K, which is the temperature of a liquid helium heat sink, in every ten steps of the simulation in a ramp fashion. The rest of the substrate atoms are kept free in their motions and their trajectories are calculated in a Newtonian fashion without any interruption. The tip is also divided into three areas consisting of free, thermostated and fixed atoms. The first 6.7 Å of the tip includes free atoms (81 in total), the following 3 Å thermostated atoms with the same properties of the thermostated atoms of the surface (44 in total), and the rest of the atoms are defined as fixed atoms (43 in total). An illustration of the simulated system and the different type of atoms can be seen in Figure 3.3.

Free Surface & Fixed Tip and Fixed Surface & Free Tip configurations are quite self-explanatory in the sense that they follow the explanations above for the Free Surface & Free Tip configuration, for the surface and the tip, respectively.

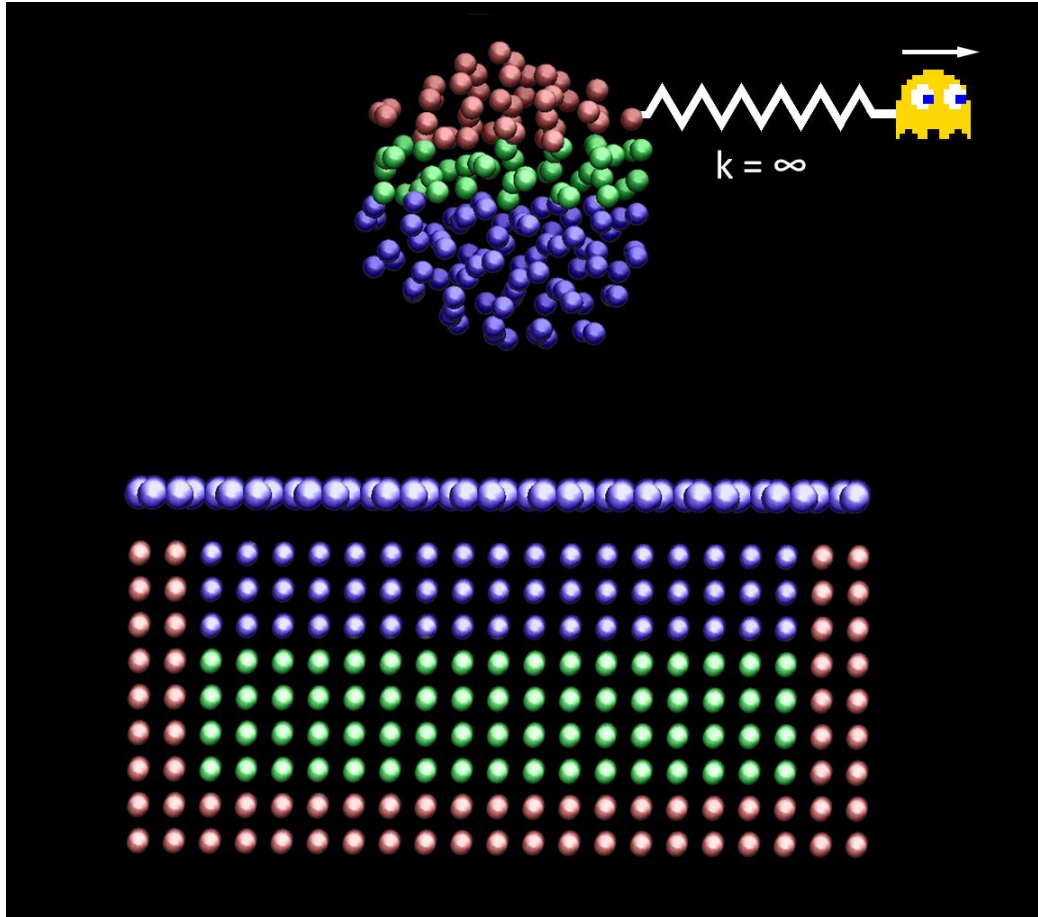


**Figure 3.3** Side view of the simulated system. Red atoms are fixed, green atoms are thermostated and blue atoms are free to move. The image of the *PacMan* ghost represents the *interactionless* ghost atom that pulls the model tip with a rigid string.

## 3.2 Cantilever Dynamics

In this thesis, the cantilever is modelled as a spring-mass-damper system with forced harmonic oscillation. Interaction between the cantilever tip and the sample surface is obtained from previously discussed MD simulations. Solution of the system and necessary controller models for different configurations are done in MATLAB® 2016b Simulink® version 8.8 with built in Runge-Kutta ODE solver with  $0.5 \mu\text{s}$  fixed time steps. The system is designed according to a high quality factor tuning fork model. Hence, the spring constant of the cantilever is assumed to be  $2000 \text{ N/m}$  with a quality factor of 10,000 and natural frequency of 25 kHz.

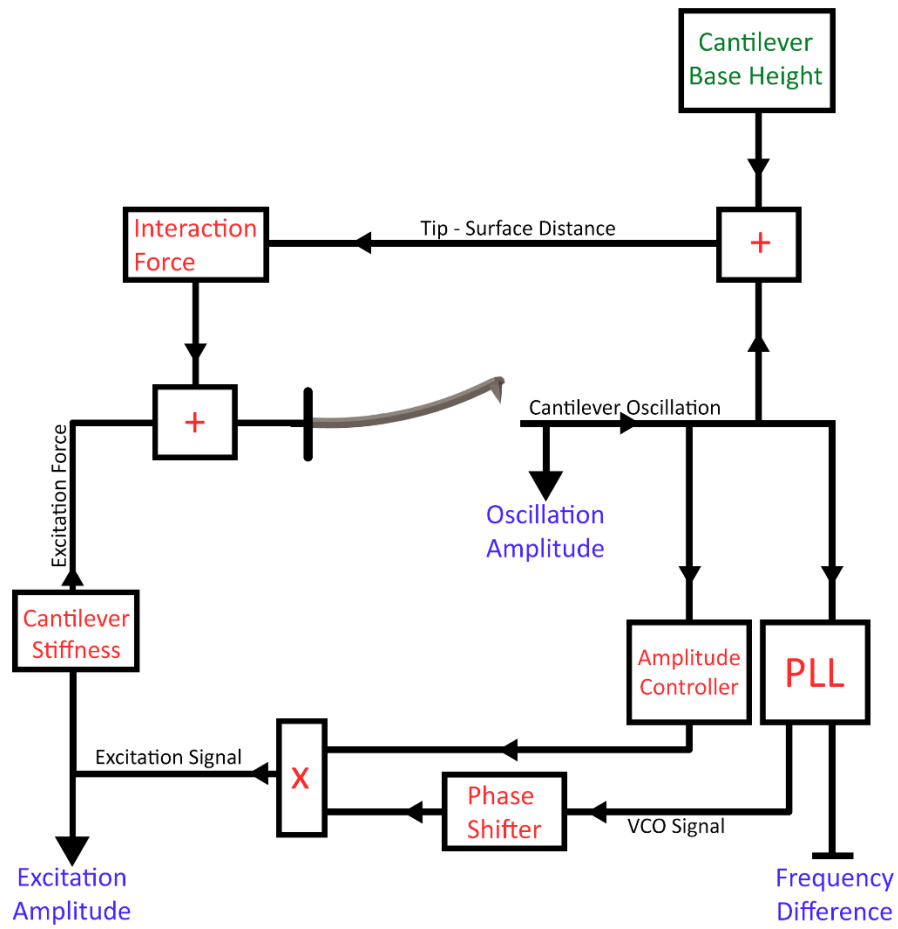


**Figure 3.4** Block diagram of the NC-AFM model working in constant height mode. Frequency detection and driving the cantilever are performed by a phase-locked loop. Driving (excitation) signal's amplitude is modulated with a PI amplitude controller. Interaction force is calculated with respect to the tip-surface distance and applied to the oscillating AFM cantilever.

Two different NC-AFM modes are simulated in Simulink: Constant Height Mode and Topography Scan. Constant height mode is a rather simple mode as mentioned before. A basic schematic of the model used in this work can be found in Figure 3.4. Detected cantilever output is fed to a PLL and its phase is locked to 0 degrees. The driving signal of the cantilever is obtained by PLL, hence PLL is used in a multi-functional fashion, and its phase is shifted by -90 degrees. In this way phase difference between excitation and response of the cantilever is set to 90 degrees. Hence, cantilever is excited with its actual resonance frequency during the entire operation. As mentioned before, interaction between the tip and substrate surface creates a position-dependent force on

the cantilever and hence changes the resonance frequency of the oscillation. With the help of PLL, this resonance frequency is tracked. Although the frequency and phase characteristics of the driving signal are obtained by PLL, its amplitude is determined by a PI amplitude controller. Amplitude of the oscillation is compared to a desired fix value and the difference (i.e., error) is used to modulate the excitation amplitude and hence, the oscillation amplitude. In this setting, the tip position (with respect to the cantilever base) is added to the cantilever base height (which is freely chosen by the user) and the tip-sample distance is calculated accordingly. Interaction force between the surface and the tip is calculated with respect to this position and the resulting force is applied to cantilever, together with the force coming from the driving signal. With this setting, the sample surface is scanned on  $xy$  planes at chosen heights in a line-by-line fashion. Logged frequency shift values are mapped. Note that, frequency shift is dependent on tip-surface interactions and stronger interactions result in larger frequency shift during oscillation. In order not to get affected by the transient response of the cantilever, cantilever is first freely oscillated without surface interactions for 0.6 s and later it is oscillated under the presence of surface interactions for 2.4 s without  $xy$  scanning. Subsequently, the scan starts.

In order to achieve topography scanning, a similar approach to the constant height mode is employed. A basic schematic of the model used for this purpose can be found in Figure 3.5. Detected cantilever output is fed to a PLL and with the help of the PLL VCO signal and a phase shifter, cantilever is driven at its resonance frequency. Likewise, oscillation amplitude is set to a desired value by modulating the excitation amplitude. The main difference from the constant height mode is that frequency shift is not simply taken as a logging result but is used to track the sample surface by changing the cantilever base position. The cantilever base position is modulated with a PI controller with respect to frequency shift: The actual frequency shift value is compared to a desired set frequency shift value and the difference (error) signal is used to modulate the cantilever base height. As such, increasing tip-sample interactions increase the frequency shift and the system responds to increasing frequency shift by increasing the cantilever-surface distance, hence decreasing interaction to the set value. In order not to get affected by the transient response of the cantilever, the cantilever is first oscillated far away from the sample for 0.6 s with the distance controller disabled. After

0.6 s, the cantilever is approached to the surface and the distance controller is enabled. Before starting to scan the surface in the  $x$  and  $y$  directions, the cantilever is oscillated on top of a fixed surface point for 2.4 s. Cantilever base height values are logged according to the  $xy$  position and topography maps of the surface are created in this fashion.

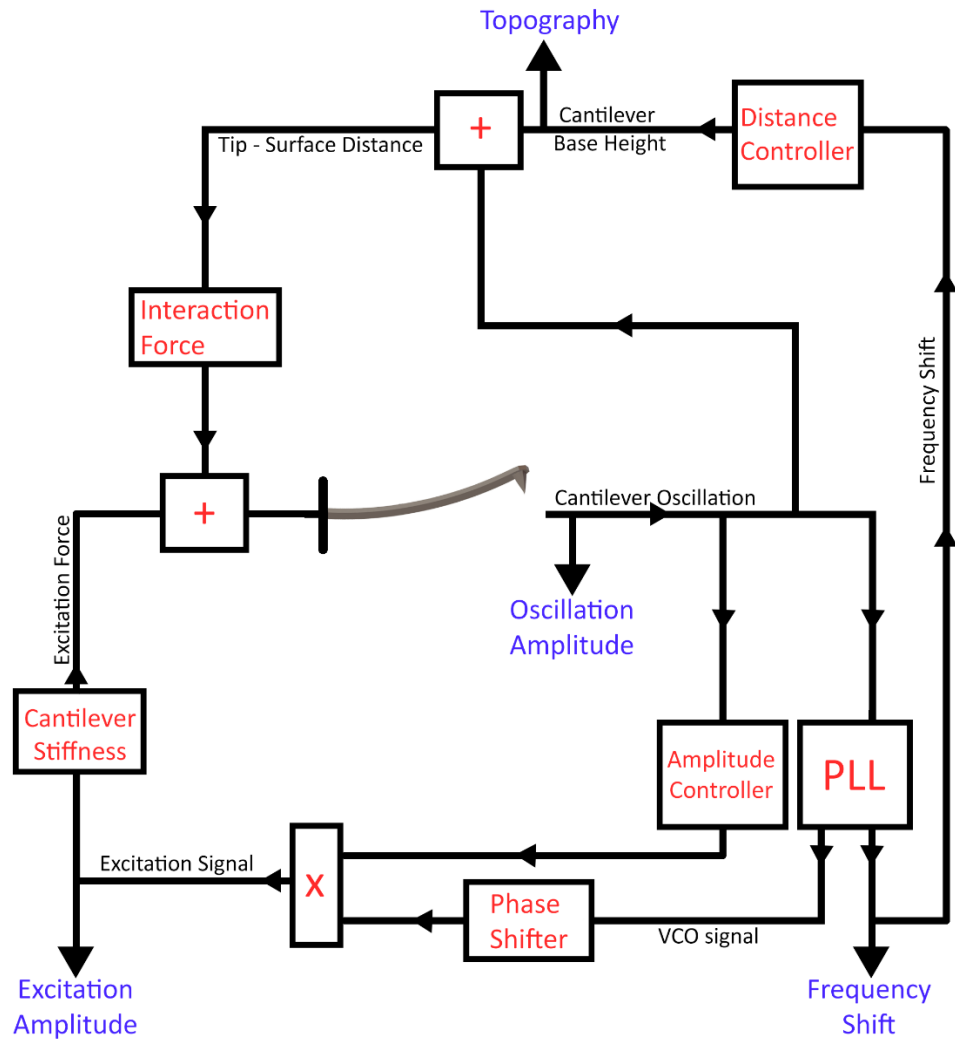


**Figure 3.5** Block diagram of the NC-AFM model working in constant height mode. Frequency detection and driving the cantilever are performed by a phase-locked loop. Driving (excitation) signal's amplitude is modulated with a PI amplitude controller. Cantilever base – surface distance is modulated according to the difference between the actual frequency shift and a set value. Interaction force is calculated with respect to the tip-surface distance and applied to the oscillating AFM cantilever.

As mentioned before, cantilever tip – surface interactions are obtained from MD simulations. As discussed in the previous chapter, interaction force between tip and the surface is saved in multiple lateral force maps with 0.5 Å height difference between them. In order to be able to use this highly discrete data in NC-AFM simulations, the data is interpolated. Due to convenience and its “feather weight” in computation, data are fitted to polynomial expressions in the  $z$  direction. First, interaction data are stacked in a 3D (volumetric) matrix.  $x$ ,  $y$  and  $z$  coordinates are represented by one single dimension of the constructed matrix. Every single array in  $z$  direction, with the same  $x$  and  $y$  coordinate, is separated into 3 overlapping sections (close, medium-range, far) and fit to a polynomial function. Hence, interaction data could be represented as a partial polynomial function. Due to employed partial fits, fitted data have discontinuities at two specific tip – sample distances where different sections overlap. These discontinuities are assumed to be small enough to not affect the cantilever motion.

# Chapter 4

## Results and Discussion

### 4.1 Force Maps Obtained by MD Simulations

As mentioned before, the first part of this work consists of Molecular Dynamics simulations. Therefore, as a starting point for this chapter, the effects of employing four different MD configurations for the same surface and AFM tip model on calculated force maps are investigated. As already discussed in the Methodology chapter, a model platinum AFM tip and platinum supported graphene surface are constructed and force maps at different heights are calculated in four different configurations, with the only difference being in the ability of surface or tip atoms to move.

The first and the simplest configuration is the “Fixed Surface & Fixed Tip” setting, where individual atoms of the tip and sample are fixed in their positions with respect to each other, with the tip moving as a rigid body over the sample to obtain force maps. Since atoms are immobile, in this configuration the initially defined tip-surface distance is equal to the distance between the foremost tip atom and the graphene sample. In simulations performed with this configuration, hollow sites (H-sites) of the graphene exhibited the most attractive force with the tip apex. This result is in line with existing

experimental work in the literature [62], [63]. Around 3.5 Å tip-surface distance, a separation between the interactions over hollow sites and carbon atoms becomes visible and the force corrugation starts to drastically increase as reported in several results in the literature [50], [52], [63] (see Figure 4.1).

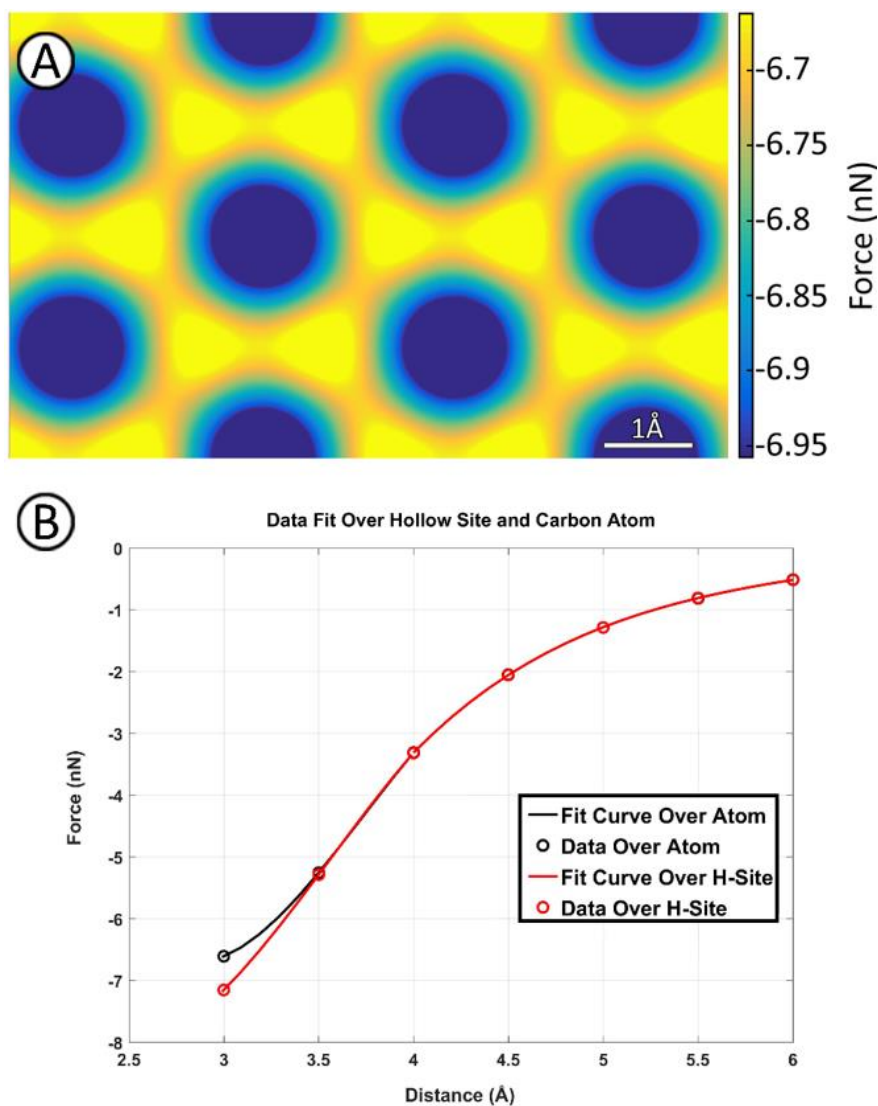


**Figure 4.1** (a) Force map obtained on the graphene surface in the “Fixed Surface & Fixed Tip” configuration at 3 Å separation. (b) Force-distance data over a carbon atom and a hollow site and their interpolated curves. Separation after 3.5 Å distance is highly visible.

In the simulated force map, the honeycomb structure of the graphene is clearly visible. But due to the asymmetry of the model tip which is a relaxed platinum chunk, it is also possible to see artifacts coming from the tip asymmetry; spatial disturbance in the force

map and in particular, shifts in detected atom positions [52]. In Figure 4.2a, spatial disturbance is highlighted. A and B types of carbon atoms of the surface are labeled and iso-color areas of A and B atoms are marked with red and black dashed lines, respectively, in the white dashed square area. When the A type atom is projected onto the B type atom, size differences between iso-color areas of different types of atoms are clearly visible. Since graphene is only single-layer in our simulations, there is no chemical/electronic difference between the two types of atoms and the difference must therefore arise from tip asymmetry [52]. Detected atom position error is demonstrated in Figure 4.2b: Real locations of six carbon atoms and one hollow site are marked with green and yellow dots, respectively. An approximate 0.5 Å of lateral shift in detected lattice positions is observed, in line with the use of an asymmetric tip [52].

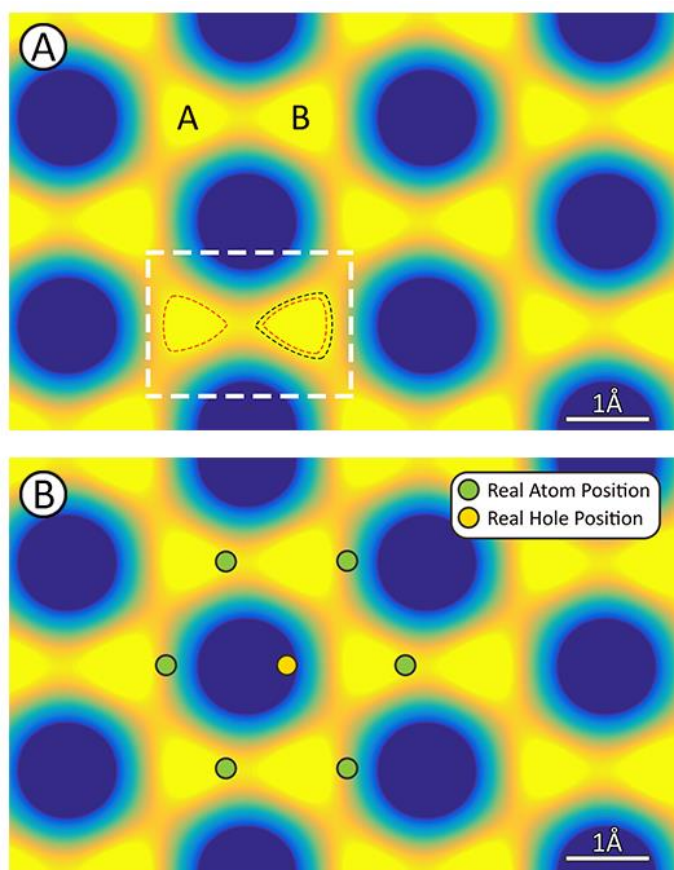


**Figure 4.2** In (a), the spatial disturbance in the force map due to tip asymmetry is marked. Two types of carbon atoms are named as A and B, and areas of the same magnitude of forces are enclosed with dashed lines. Two perimeters are projected on one another and the difference between the areas of A and B atoms becomes quite

visible. In (b), actual positions of carbon atoms and a hollow site are marked on the force map acquired by the same asymmetric tip. An approximate 0.5 Å of lateral shift in detected positions is observed.

As the next configuration, the “Fixed Surface & Free Tip” setting can be discussed. As already described in the Methodology chapter, this configuration has immobile surface atoms and a more realistic deformable tip where most of the tip atoms are free in motion. In this configuration, the shift in detected atom positions are stronger due to the mobile tip apex which may temporarily create more asymmetry in the tip during scanning (Figure 4.3a). In close distances between tip and surface, extensive motion of apex atoms may occur which results in artifacts and distortions in force maps (Figure 4.3b).

The “Fixed Surface & Free Tip” configuration reaches its maximum attractive interaction at 4 Å of separation. Moreover, by comparing Figure 4.1 and Figure 4.3, one can see that the interaction forces between surface and tip are smaller in the “Fixed Surface & Free Tip” configuration when compared with the “Fixed Surface & Fixed Tip” configuration. These may be explained by the elastic elongation of the tip during simulations. Although the tip-sample separation is recorded as 4 Å, the actual distance between the foremost tip atom and the surface is approximately 3 Å due to the elongation of the tip in response to tip-surface interaction. Consequently, if the length of the tips are measured in both configurations in the vertical direction, the fixed tip exhibits a length of 14.7 Å while the free tip is about 15.8 Å. Additionally, once the tip elongates, the number atoms that are relatively close to surface decrease, hence less interaction between surface and the tip is obtained. In Figure 4.4, the distribution of the tip atoms with respect to their heights (as measured from the tip apex) is reported for both configurations, demonstrating tip elongation and increasing tip sharpness.

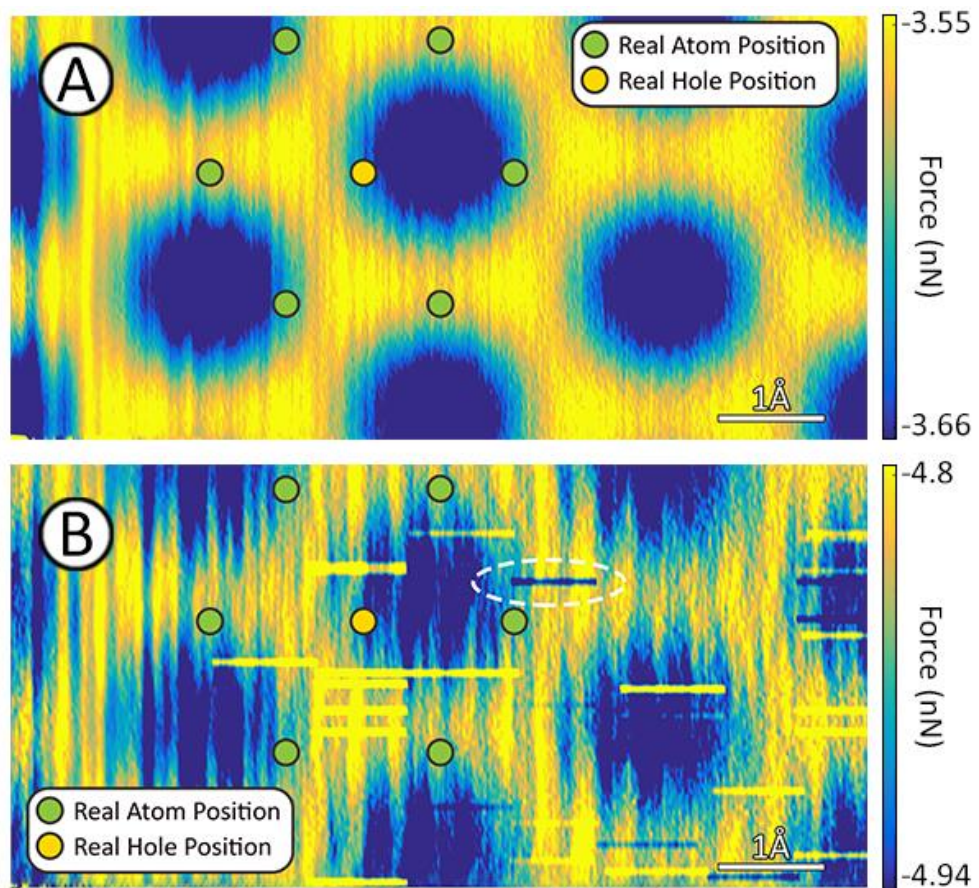


**Figure 4.3** Two force maps obtained in the “Fixed Surface & Free Tip” configuration. (a) and (b) are taken at separations of 4.5 Å and 4 Å, respectively. There is considerable shift in detected lateral positions of surface sites along both  $x$  and  $y$  directions. Distortions and artifacts due to atomic motion are visible in (b).

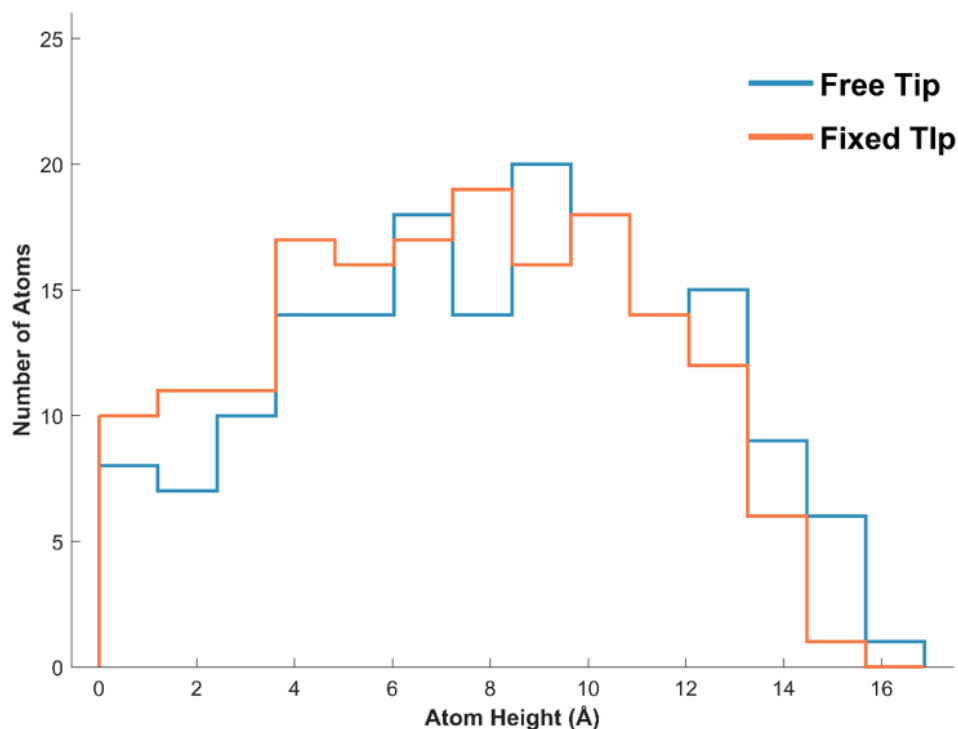


**Figure 4.4** Histogram of tip atom heights (as measured from the tip apex). Free tip atoms are denoted by blue and fixed tip atoms are denoted by orange. Foremost tip atoms are assumed to have a height of zero before preparation of the histogram. As can be seen from the histogram, the fixed tip contains more atoms in the near-surface region. The free tip is elongated and contains less atoms in the near-surface region.

The “Free Surface & Fixed Tip” configuration contains a fixed tip undergoing rigid body motion and a relaxed, free substrate surface. Details of the structure of free surface are discussed in the Methodology chapter. Just like the configuration before, it features one *frozen* part and one realistic, free part which is the surface in this case. In this configuration, the distance between the platinum surface and graphene decreases by more than 0.5 Å during relaxation. Spatial disturbance of the honeycomb structure in force maps is clearly visible and more obvious than the “Fixed Surface – Fixed Tip” configuration (Figure 4.5b). This may be explained by the partial elevation of the graphene surface towards the tip during scanning: Specifically, graphene beneath the tip apex elevates and forms a bump due to attractive force interactions (Figure 4.6). The created bump follows the scanning tip like a “Mexican wave” and is the part that interacts the most with the tip.

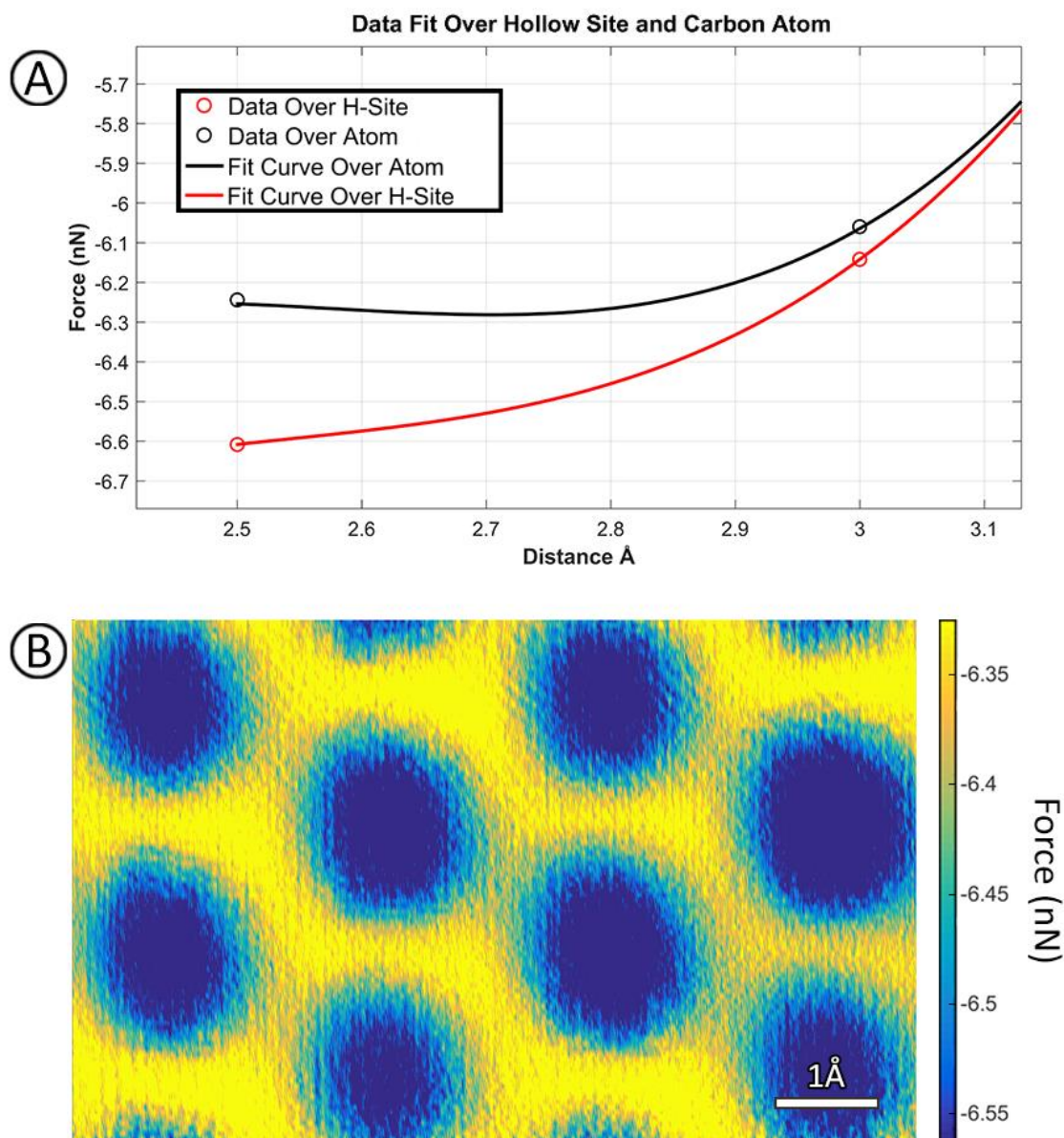


**Figure 4.5** (a) Force-distance data over a carbon atom and a hollow site and their interpolated curves in the “Free Surface & Fixed Tip” configuration. Although separation starts before 3 Å, separation after 3 Å is quite clear. (b) Force map at 2.5 Å separation. The spatial disturbance of the honeycomb structure, caused by tip asymmetry and amplified by surface deformation, is clearly visible. Please note that the indicated tip-sample distances are with respect to the unrelaxed state of the system (i.e., before the graphene moves down to the platinum support by an additional 0.5 Å).

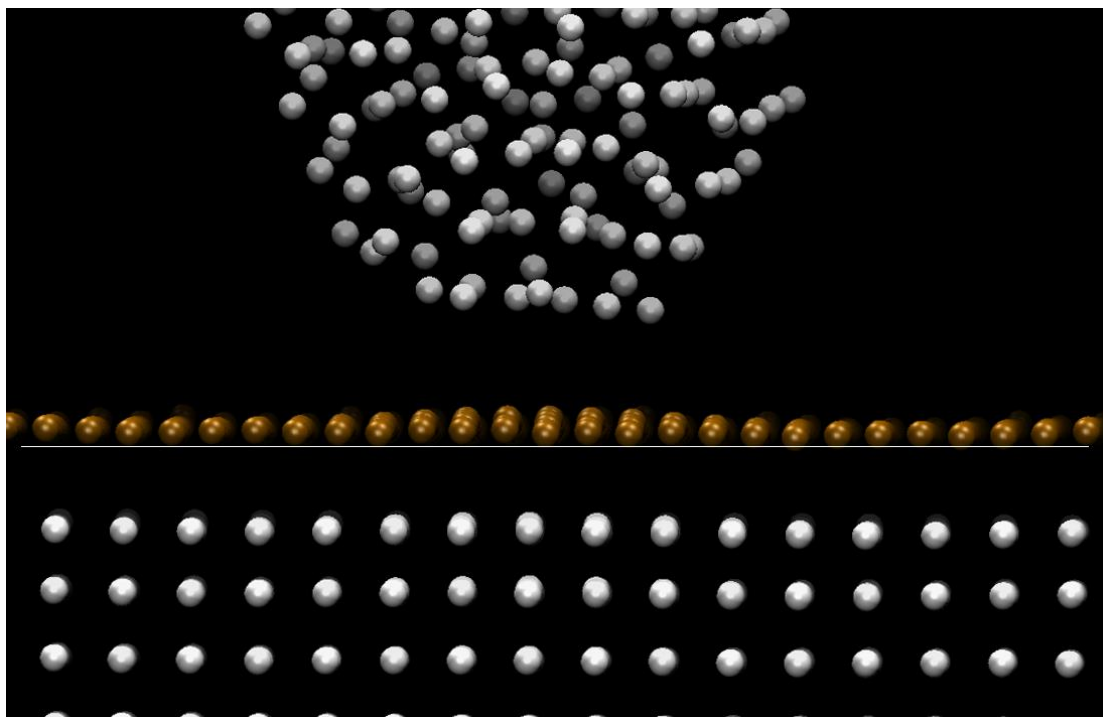


**Figure 4.6** A simulation snapshot from the “Free Surface & Fixed Tip” configuration. Carbon atoms close to the tip are elevated nearly  $0.5\text{\AA}$  toward the tip. A white guide line has been drawn under the line of carbon atoms to make elevated atoms more visible. The tip is followed by this bump of carbon atoms like a “Mexican wave”.

The final setting to be considered is the “Free Surface & Free Tip” configuration, where surface and tip mainly consist of free atoms as discussed in the Methodology chapter. Since this configuration does not contain any rigid bodies, it is the most realistic setting among the four configurations. The maximum attractive interaction in this configuration occurs at  $3.5\text{\AA}$  separation, which corresponds to somewhere between “Fixed Surface – Fixed Tip” and “Fixed Surface – Free Tip” maximum attractive interaction tip heights. This can be easily explained by a combining the effect of tip elongation and the descent of graphene onto the platinum substrate. In this configuration small spatial distortions due to atomic motion are also visible and the overall force maps appear noisier (Figure 4.7).

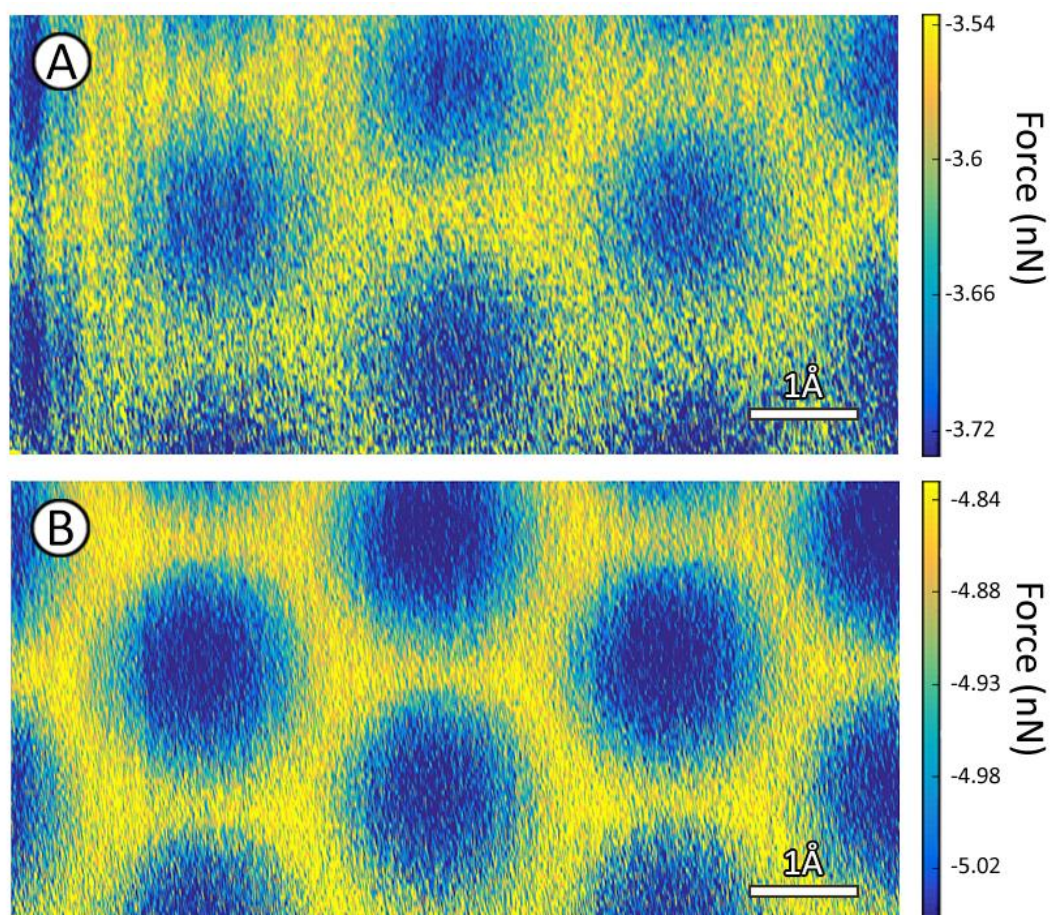


**Figure 4.7** Force maps at (a) 3.5 Å and (b) 4 Å separation obtained in the “Free Surface & Free Tip” configuration. Although it is very easy to discern the honeycomb structure of the graphene at both tip heights, noise over the force maps due to atomic motion is clearly visible.

During NC-AFM measurements, interaction force corrugation is crucial to distinguish different parts of the surface, therefore looking at 2D, vertical maps of interaction forces is beneficial [52] (Figure 4.8). As in the horizontal force maps, it is easy to distinguish carbon atoms and hollow sites, and individual atom movement in deformable bodies lead to noise on images. Site-specific variations in interaction forces can be detected as a function of tip-sample distance using such maps.

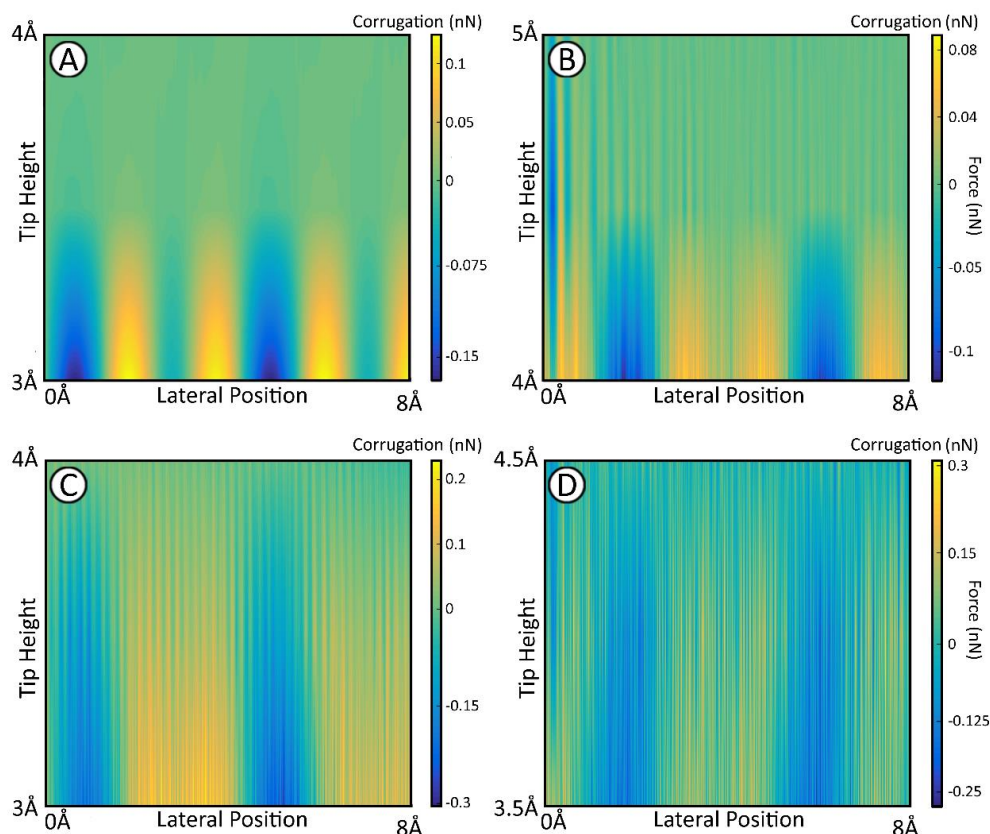


**Figure 4.8** Vertical slices of interaction forces obtained via different configurations. Blue and yellow colored parts represents more and less attractive parts of the surface, respectively. (a) Fixed Surface & Fixed Tip. (b) Fixed Surface & Free Tip. (c) Free Surface & Fixed Tip. (d) Free Surface & Free Tip.

## 4.2 NC-AFM Scanning Results

As discussed in the Methodology section, obtained volumetric force maps simulating the interaction between tip and sample are “scanned” with a virtual NC-AFM based on the harmonic oscillator model in two different modes: constant height and topography scan. In the constant height mode, the frequency shift created in the oscillating cantilever is tracked, as discussed before. Via Figure 4.9 and Figure 4.10 it is clear to observe that frequency shift scan maps are able to visualize surfaces properly. As expected, artifacts in the interaction force maps are carried over to the scan results and images highly resemble interaction force maps that are taken near the minimum separation reached by the tip of the oscillating cantilever.

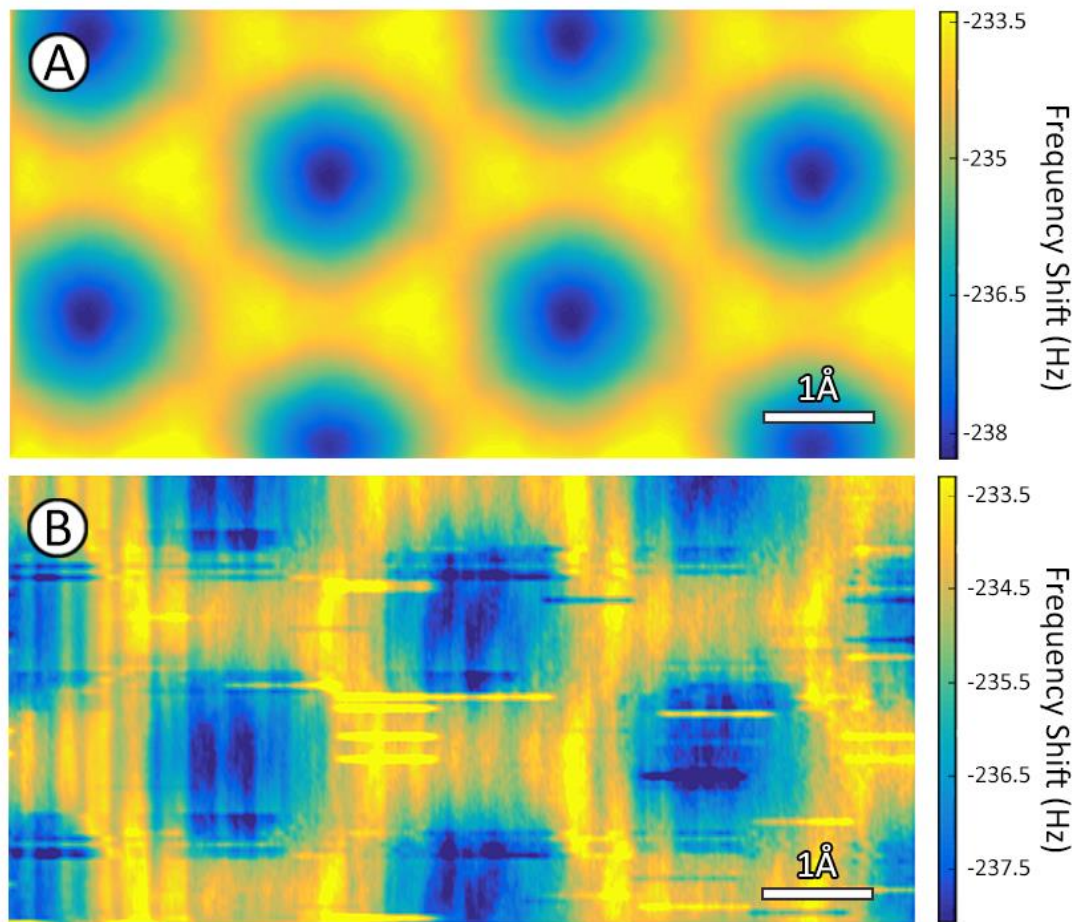


**Figure 4.9** NC-AFM scans of (a) “Fixed Surface & Fixed Tip” and (b) “Fixed Surface & Free Tip” configurations in constant height mode. Artifacts discussed for force maps of the configurations are carried over to the scans. Please note that the scan area in (a) is smaller than the horizontal force map presented in Figure 4.1a.

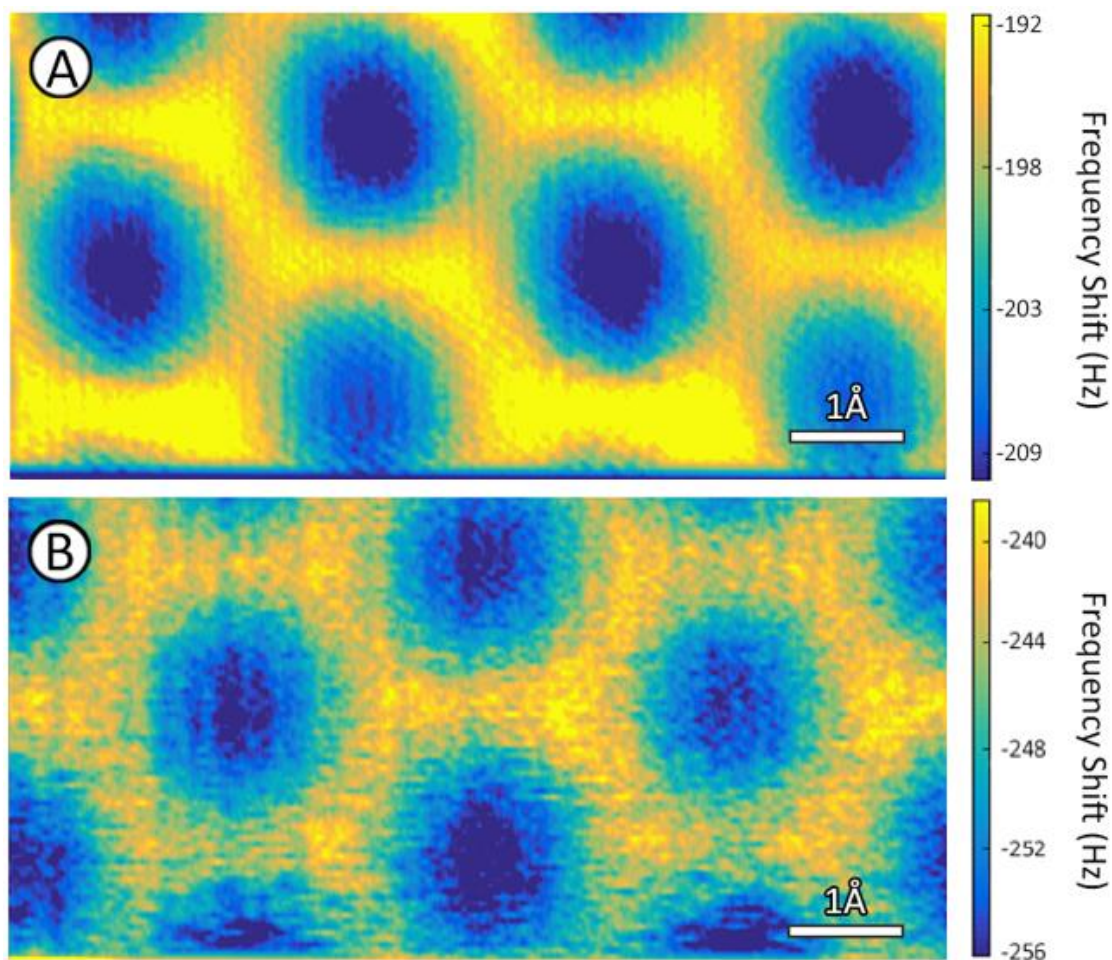


**Figure 4.10** NC-AFM scans of (a) “Free Surface & Fixed Tip” and (b) “Free Surface & Free Tip” configurations in constant height mode. Artifacts discussed for force maps of the configurations are carried over to the scans. Please note that the scan area in (a) is smaller than the horizontal force map presented in Figure 4.5b.

Higher interaction forces are expected to yield higher (absolute) frequency shift values since an oscillating cantilever in absence of interaction force would not have any frequency shift. Following this line of argument, approaching the cantilever base to the surface is expected to increase the overall frequency shift during scanning. This expectation is met by the data presented in Figure 4.11. In the figure, constant height NC-AFM scans of the “Free Surface & Free Tip” configuration are shown at two different separations of 4.2 Å and 4.4 Å. Moving the cantilever base by 0.2 Å results in an increase of frequency shift by ~30 Hz.

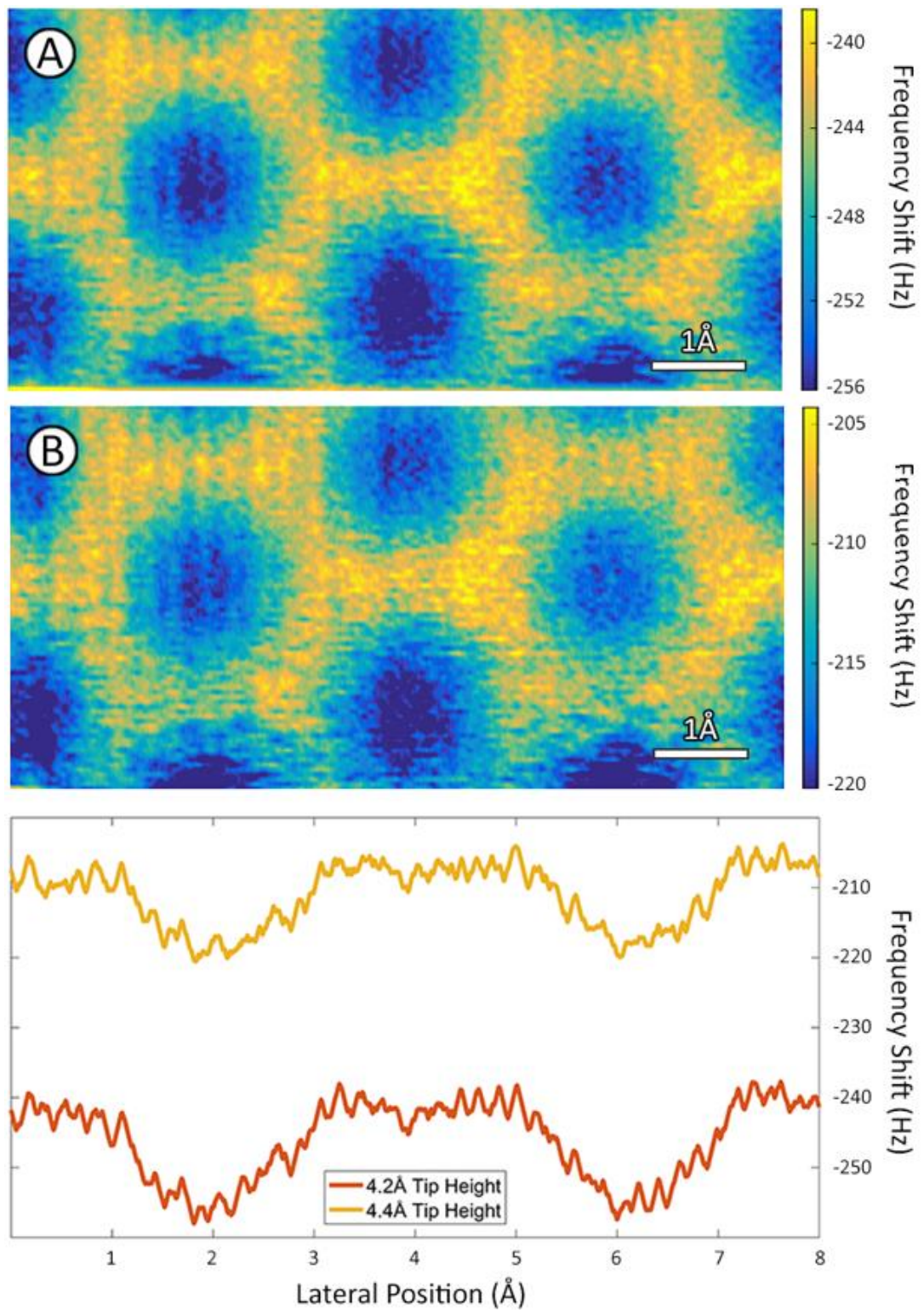


**Figure 4.11** NC-AFM constant height mode images taken from the “Free Surface & Free Tip” configuration at (a) 4.2 Å and (b) 4.4 Å separations with 0.8 Å peak-to-peak (p-p) oscillation amplitude. (c) Line profiles taken from NC-AFM scans at two different separations of 4.2 Å and 4.4 Å.

One other parameter of importance for a constant height mode NC-AFM scan is the oscillation amplitude of the cantilever. At the same cantilever base height, increasing oscillation amplitude increases the tip-surface attractive interaction during the half cycle of the cantilever oscillation close to the surface, however it also decreases the same interaction during the other half of the cycle, away from the surface. In Figure 4.12 constant height scans with two different oscillation amplitudes are presented. Increasing the oscillation amplitude results in a decrease of the frequency shift, confirming results from the literature that predict higher sensitivity to interaction forces with lower oscillation amplitudes [41].

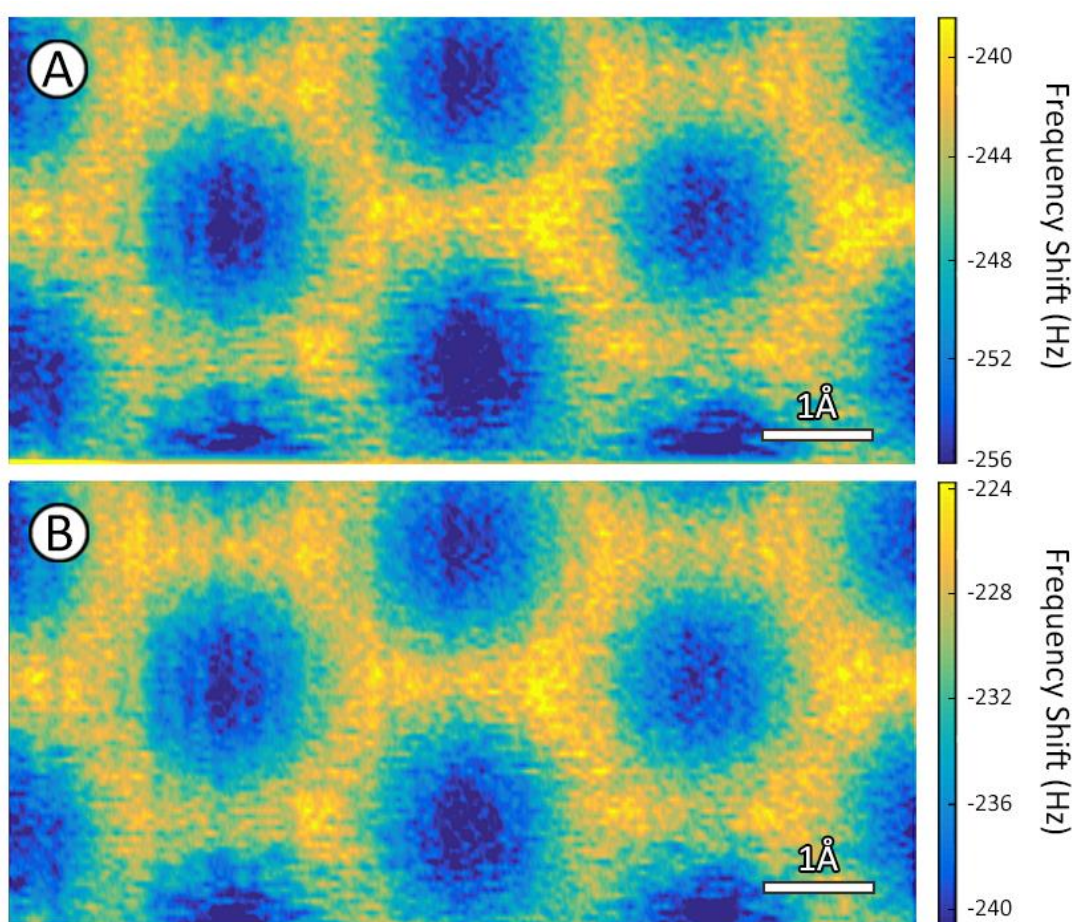


**Figure 4.12** Constant height scans in the “Free Surface & Free Tip” configuration with 4.2 Å separation and two different p-p oscillation amplitudes: (a) 0.8 Å, (b) 1 Å. As can be seen from the images, increasing the oscillation amplitude decreases the overall frequency shift.

Like in constant height mode scans, the topography mode is also successful in scanning surfaces and yields reasonable topography maps and error data, which essentially is the deviation from the set frequency shift. As discussed before, high interaction yields high frequency shift, so in this configuration higher interactions lead to the tip to get retracted from the surface. Hence, hollow sites of the graphene surface are tracked by the distance controller as ‘bumps’. In Figure 4.13, representative topography and controller error maps of the “Free Surface & Free Tip” configuration, which is the most realistic one discussed, can be found. Hollow-sites are tracked with higher cantilever base height, as round “bumps”.

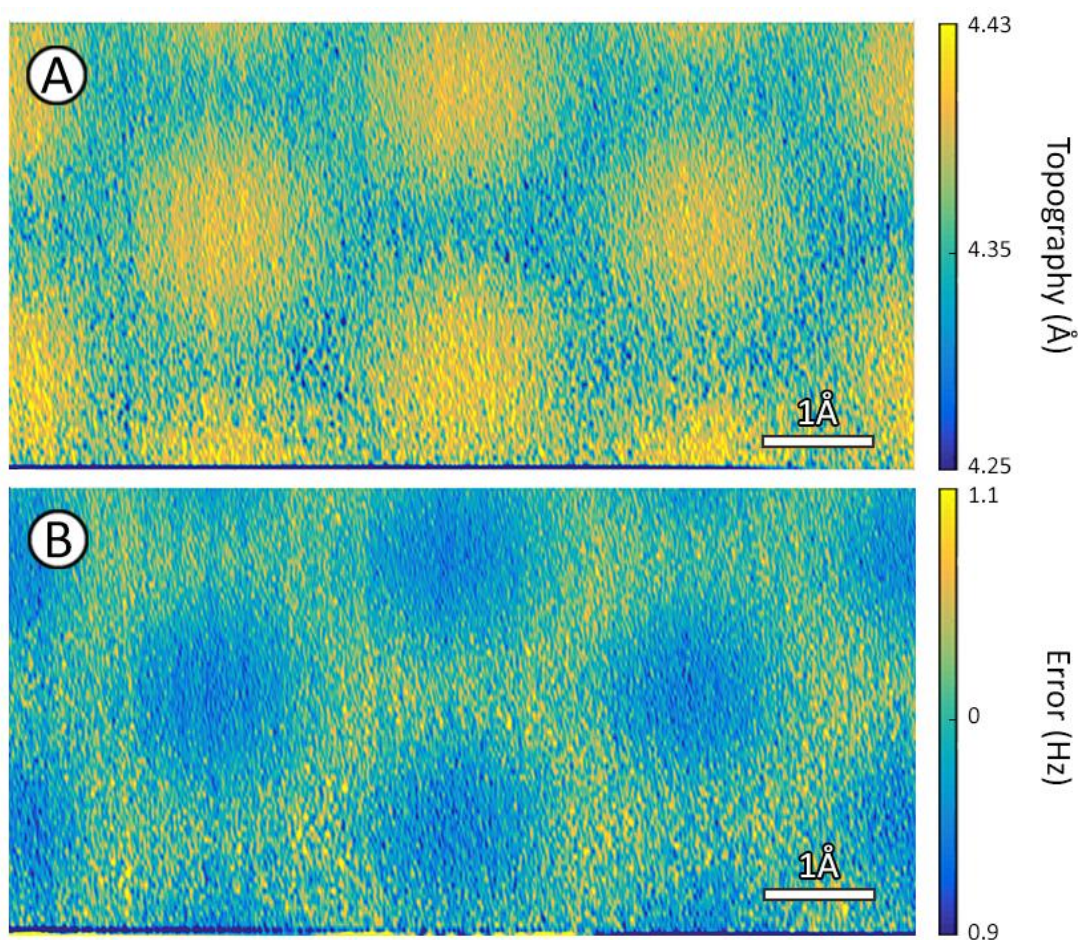


**Figure 4.13** NC-AFM topography scan of the “Free Surface & Free Tip” configuration where (a) is the obtained topography map and (b) is the error signal map. Set frequency shift is -222 Hz. Hollow-sites are shown in the topography map with larger heights, in accordance with their higher reactivity when compared with carbon atoms.

Changing the set frequency shift value of the distance controller also affects the topography map taken. As expected, a higher difference from the natural frequency of the cantilever brings the cantilever closer to the surface since higher detuning requires higher interaction. This is expected to result in higher corrugations in topography. As can be seen from the Figure 4.14, changing the set frequency shift from -200 Hz to -222 Hz leads to a slight increase in topographical corrugation (from 12 pm to 16 pm). This result is also consistent with previously discussed constant height images at different cantilever base heights.

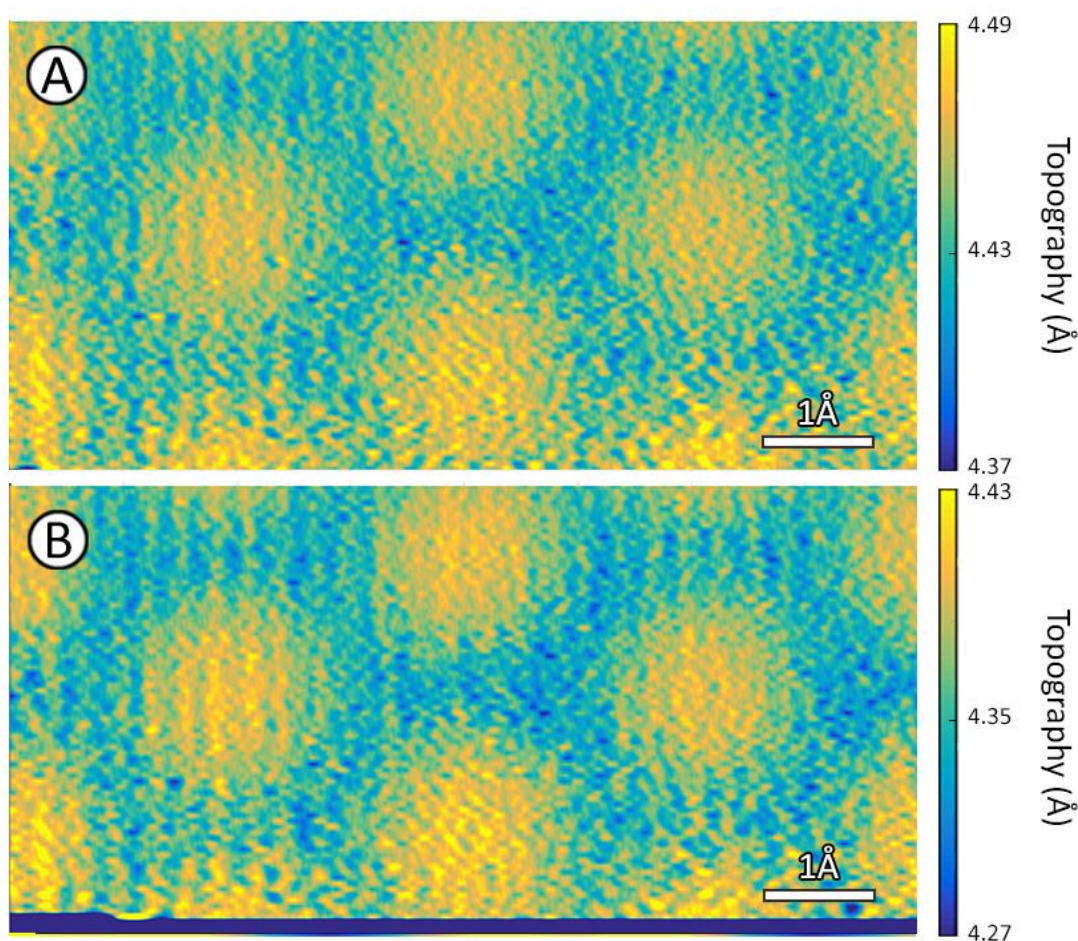


**Figure 4.14** Two topography scans with (a) -200 Hz and (b) -222 Hz frequency shift values. With increasing deviation from the initial natural frequency, the corrugation of the topography maps increases, consistent with a smaller mean tip-sample distance. In (b) at the very bottom of the image there are visible artifact due to the less than ideal settings of the distance controller. Please note that the image in (b) has been acquired with different controller parameters than the image in Figure 4.13a.

The distance controller is an essential part of the topography scan mode and differentiates it from the constant height mode. Employed controller values/parameters directly affect the obtained images. For instance, having a very slow controller with small P values makes the controller dysfunctional and the cantilever becomes unable to track the surface. In that case, the error signal becomes larger and starts to resemble the surface (see Figure 4.15). Because the system starts to act as in constant height mode with slow distance controllers, “quasi-static” constant height images can be taken by intentionally setting distance controller parameters quite slow, as discussed before. Although having a slow distance controller is undesired, a very fast controller, on the other hand, causes artifacts and noisy images. A controller with very large P values leads to controller noise and “buries” the surface topography (see Figure 4.16). Thus, as demonstrated and verified by our simulations, finding optimum controller parameters is quite important during NC-AFM operation.

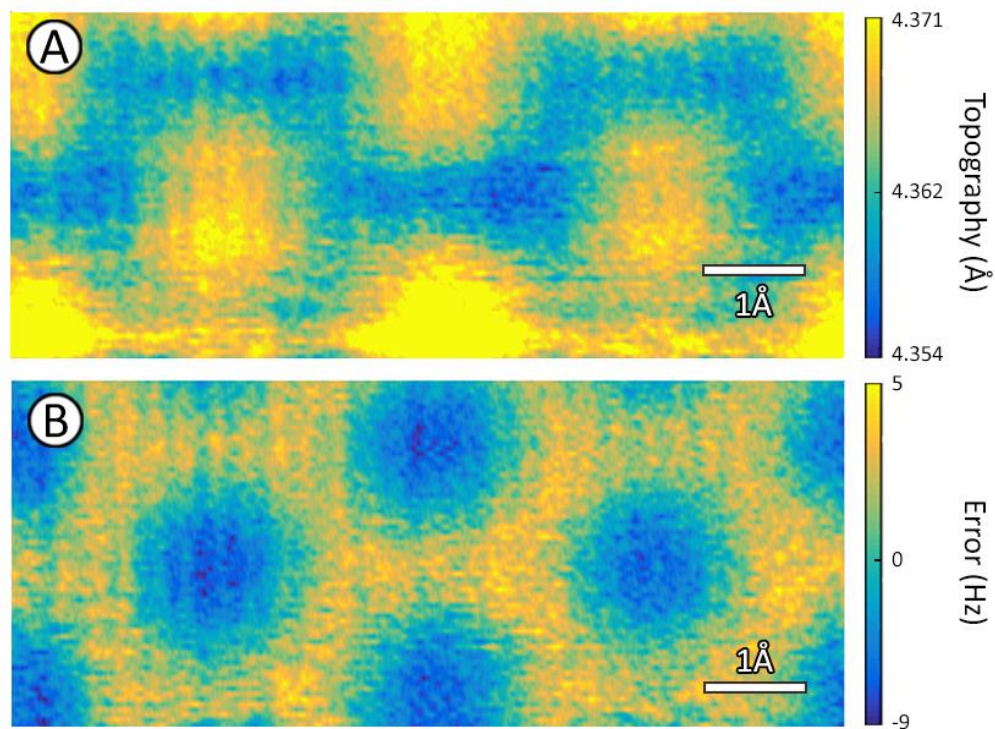


**Figure 4.15** NC-AFM scan with -220 Hz frequency shift set point, 0.8 Å p-p oscillation amplitude and a very slow distance controller. (a) Topography map demonstrates very low corrugation ( $\sim 2$  pm) which may be impossible to detect in a real life experiment. (b) Error signal demonstrates very high corrugation in error, when compared with Figure 4.13b.

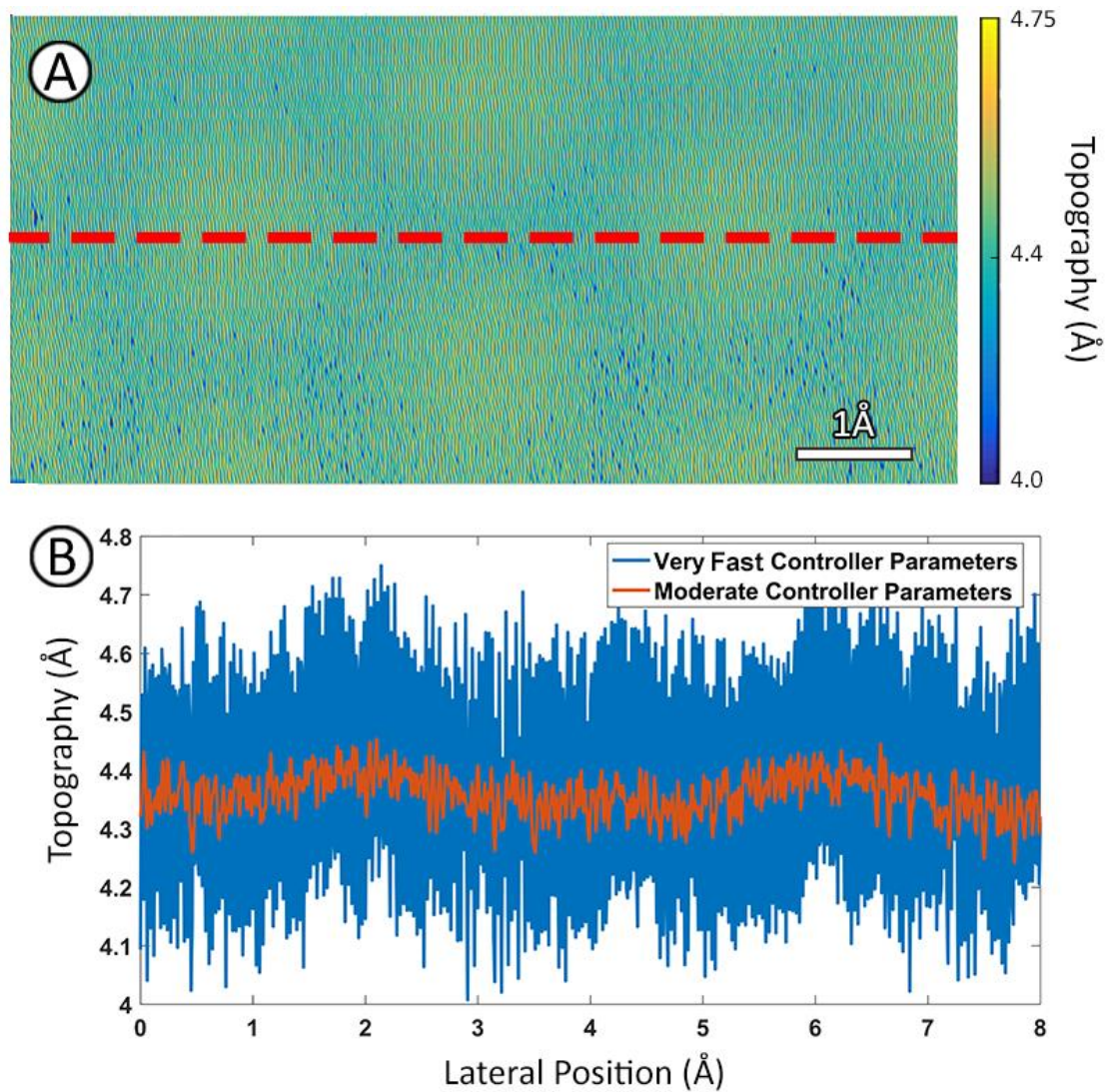


**Figure 4.16** (a) Topography map obtained with -220 Hz frequency shift set point, 0.8 Å p-p oscillation amplitude and a very fast distance controller. Although corrugation is quite high, it is not easy to distinguish hollow sites of the graphene surface due to controller-induced overall noise over the image. (b) Blue graph demonstrates a line profile taken along the red dashed line in (a). Red line demonstrates the line profile taken from a different scan with a more optimal distance controller. As one can see, very fast controller parameters create additional noise over the physical features rather than improve tracking.

## Chapter 5

### Conclusion and Outlook

In this MS thesis, a model for simulating non-contact atomic force microscopy (NC-AFM) experiments by using molecular dynamics (MD) and the harmonic oscillator model is presented. The suggested model is tested in with a sample surface-tip couple and two different NC-AFM scanning modes.

For modeling the interaction between the AFM cantilever tip and the sample surface, MD techniques are employed. A model, single-layer graphene surface supported by a bulk platinum substrate and a platinum tip are constructed as the main components of the simulated system. Four different tip-sample combinations according to the deformability of the corresponding tips and samples are created, and the interaction forces are calculated on 2D, horizontal planes at different vertical separations. The discrete 3D data obtained in this fashion is fitted to partial polynomial functions to be subsequently used in the harmonic oscillator model. Using the harmonic oscillator model, two different NC-AFM scan modes are simulated: constant height and topography scan.

After obtaining force maps from different configurations, it is observed that tip asymmetry creates an overall spatial disturbance in the images. Furthermore, tip asymmetry creates a lateral shift in the detected positions of surface sites. Having a

deformable and hence, realistic tip, decreases the interaction forces. Specifically, due to tip elongation, the number of atoms at the very apex of the tip (the region closest to the sample surface) decreases and so does the overall interaction with the surface. On the other hand, the mobility of the surface atoms makes graphene reach out toward the tip by forming local bumps beneath the apex. It is observed that deformable tips and surfaces in general lead to the observation of an overall noise on the images due to thermally-induced motion.

Employing the simulated force maps, the suggested NC-AFM model is tested in two different scanning modes. In the constant height mode, more attractive interaction yields larger absolute values of frequency shift. Hence, hollow-sites of the graphene yield more frequency shift than carbon atoms. Likewise; decreasing the distance between the cantilever and the surface leads to larger frequency shifts, as expected. Increasing the oscillation amplitude of the cantilever caused the overall frequency shift, and hence, the sensitivity to force interactions, to decrease. In the topography scan mode, hollow-sites are tracked via locally increasing cantilever-surface distance due to higher attractive interactions. Increased absolute set frequency shift values increase topographical corrugation, as expected from the literature. Distance controller parameters also have a huge impact on topography maps, as expected. Very low speed controllers are unable to track the surface. On the other hand, very fast distance controllers cause noise over the images, hence decreasing image quality and burying physical information.

Although the work presented in this thesis constitutes a functional simulator for NC-AFM, for improving the accuracy of the simulations with respect to experiments, the size of the simulated systems can be increased. With a larger number of tip and surface atoms, more realistic force maps can be obtained. Furthermore, having more force maps in the vertical direction would improve the accuracy of the fitted force data that are imported by the harmonic oscillator model. Changing the distance controller from basic PI and experimenting with other types of controllers, like adaptive ones, could provide insight about less conventional AFM setups and may lead to new designs for future applications.

# Bibliography

- [1] G. Binnig, H. Rohrer, C. Gerber, and E. Weibel, “7 x 7 Reconstruction on Si(111) Resolved in Real Space,” *Phys. Rev. Lett.*, vol. 50, no. 2, pp. 120–123, 1983.
- [2] R. Wiesendanger, H.-J. Güntherodt, G. Güntherodt, R. J. Gambino, and R. Ruf, “Observation of vacuum tunneling of spin-polarized electrons with the scanning tunneling microscope,” *Phys. Rev. Lett.*, vol. 65, no. 2, pp. 247–250, 1990.
- [3] Y. Hasegawa and P. Avouris, “Direct observation of standing wave formation at surface steps using scanning tunneling spectroscopy,” *Phys. Rev. Lett.*, vol. 71, no. 7, pp. 1071–1074, 1993.
- [4] R. J. Hamers, R. M. Tromp, and J. E. Demuth, “Surface electronic structure of Si (111)-(7x7) resolved in real space,” *Phys. Rev. Lett.*, vol. 56, no. 18, pp. 1972–1975, 1986.
- [5] J. A. Stroscio, R. M. Feenstra, and A. P. Fein, “Electronic structure of the Si(111)2 x 1 surface by scanning-tunneling microscopy,” *Phys. Rev. Lett.*, vol. 57, no. 20, pp. 2579–2582, 1986.
- [6] D. M. Eigler and E. K. Schweizer, “Positioning single atoms with a scanning tunnelling microscope,” *Nature*, vol. 344, no. 6266, pp. 524–526, 1990.
- [7] J. Repp, G. Meyer, F. E. Olsson, and M. Persson, “Controlling the Charge State of Individual Gold Adatoms,” *Science*, vol. 305, no. 5683, pp. 493–495, 2004.
- [8] D. Serrate *et al.*, “Imaging and manipulating the spin direction of individual atoms,” *Nat. Nanotechnol.*, vol. 5, no. 5, pp. 350–353, 2010.
- [9] The Royal Swedish Academy of Sciences, “The Nobel Prize in Physics 1986,” 1986. [Online]. Available: [http://www.nobelprize.org/nobel\\_prizes/physics/laureates/1986/press.html](http://www.nobelprize.org/nobel_prizes/physics/laureates/1986/press.html)
- [10] U. Hartmann, “Magnetic force microscopy: Some remarks from the micromagnetic point of view,” *J. Appl. Phys.*, vol. 64, no. 3, pp. 1561–1564, 1988.

- [11] J. R. Matey and J. Blanc, “Scanning capacitance microscopy,” *J. Appl. Phys.*, vol. 57, no. 5, pp. 1437–1444, 1985.
- [12] A. M. Chang *et al.*, “Scanning Hall probe microscopy,” *Appl. Phys. Lett.*, vol. 61, no. 16, pp. 1974–1976, 1992.
- [13] U. Dürig, D. W. Pohl, and F. Rohner, “Near-field optical-scanning microscopy,” *J. Appl. Phys.*, vol. 59, no. 10, pp. 3318–3327, 1986.
- [14] V. J. Morris, A. R. Kirby, and A. P. Gunning, *Atomic Force Microscopy for Biologists*, 2<sup>nd</sup> ed. London: Imperial College Press, 2009.
- [15] G. Binnig and C. F. Quate, “Atomic Force Microscope,” *Phys. Rev. Lett.*, vol. 56, no. 9, pp. 930–933, 1986.
- [16] P. Eaton and P. West, *Atomic Force Microscopy*. Oxford: Oxford University Press, 2010.
- [17] B. Leimkuhler and C. Matthews, *Molecular Dynamics*. Berlin: Springer International Publishing, 2015.
- [18] The Royal Swedish Academy of Sciences, “The Nobel Prize in Chemistry 2013,” 2013. [Online]. Available: [http://www.nobelprize.org/nobel\\_prizes/chemistry/laureates/2013/press.html](http://www.nobelprize.org/nobel_prizes/chemistry/laureates/2013/press.html)
- [19] J. D. Bernal, “A Geometrical Approach to the Structure Of Liquids,” *Nature*, vol. 183, no. 4655, pp. 141–147, 1959.
- [20] J. D. Bernal, “The Bakerian Lecture, 1962. The Structure of Liquids,” *Proc. R. Soc. A Math. Phys. Eng. Sci.*, vol. 280, no. 1382, pp. 299–322, 1964.
- [21] B. J. Alder and T. E. Wainwright, “Phase Transition for a Hard Sphere System,” *J. Chem. Phys.*, vol. 27, no. 5, pp. 1208–1209, 1957.
- [22] B. J. Alder and T. E. Wainwright, “Studies in Molecular Dynamics. I. General Method,” *J. Chem. Phys.*, vol. 31, no. 2, pp. 459–466, 1959.
- [23] J. B. Gibson, A. N. Goland, M. Milgram, and G. H. Vineyard, “Dynamics of radiation damage,” *Phys. Rev.*, vol. 120, no. 4, pp. 1229–1253, 1960.

- [24] A. Rahman, "Correlations in the Motion of Atoms in Liquid Argon," *Phys. Rev.*, vol. 136, no. 2A, pp. A405–A411, 1964.
- [25] L. Verlet, "Computer 'Experiments' on Classical Fluids. I. Thermodynamical Properties of Lennard-Jones Molecules," *Phys. Rev.*, vol. 159, no. 1, pp. 98–103, 1967.
- [26] M. Z. Baykara, O. E. Dagdeviren, T. C. Schwendemann, H. Mönig, E. I. Altman, and U. D. Schwarz, "Probing three-dimensional surface force fields with atomic resolution: Measurement strategies, limitations, and artifact reduction," *Beilstein J. Nanotechnol.*, vol. 3, no. 1, pp. 637–650, 2012.
- [27] M. Klocke and D. E. Wolf, "Coupled molecular and cantilever dynamics model for frequency-modulated atomic force microscopy," *Beilstein J. Nanotechnol.*, vol. 7, no. 1, pp. 708–720, 2016.
- [28] M. S. Daw and M. I. Baskes, "Semiempirical, quantum mechanical calculation of hydrogen embrittlement in metals," *Phys. Rev. Lett.*, vol. 50, no. 17, pp. 1285–1288, 1983.
- [29] M. S. Daw and M. I. Baskes, "Embedded-atom method: Derivation and application to impurities, surfaces, and other defects in metals," *Phys. Rev. B*, vol. 29, no. 12, pp. 6443–6453, Jun. 1984.
- [30] J. Tersoff, "New empirical approach for the structure and energy of covalent systems," *Phys. Rev. B*, vol. 37, no. 12, pp. 6991–7000, 1988.
- [31] D. Brenner, "Empirical potential for hydrocarbons for use in simulating the chemical vapor deposition of diamond films," *Phys. Rev. B*, vol. 42, no. 15, pp. 9458–9471, 1990.
- [32] S. J. Stuart, A. B. Tutein, and J. A. Harrison, "A reactive potential for hydrocarbons with intermolecular interactions," *J. Chem. Phys.*, vol. 112, no. 14, pp. 6472–6486, 2000.
- [33] W. W. Wood and J. D. Jacobson, "Preliminary Results from a Recalculation of the Monte Carlo Equation of State of Hard Spheres," *J. Chem. Phys.*, vol. 27, no. 5, pp. 1207–1208, 1957.

- [34] M. Levitt and A. Warshel, "Computer simulation of protein folding," *Nature*, vol. 253, no. 5494, pp. 694–698, 1975.
- [35] H. Hu and Y. Sun, "Molecular dynamics simulations of disjoining pressure effect in ultra-thin water film on a metal surface," vol. 263110, pp. 1–5, 2013.
- [36] Z. Ye, P. Egberts, G. H. Han, A. T. C. Johnson, R. W. Carpick, and A. Martini, "Load-Dependent Friction Hysteresis on Graphene," *ACS Nano*, vol. 10, no. 5, pp. 5161–5168, 2016.
- [37] P. L. Freddolino, A. S. Arkhipov, S. B. Larson, A. McPherson, and K. Schulten, "Molecular dynamics simulations of the complete satellite tobacco mosaic virus," *Structure*, vol. 14, no. 3, pp. 437–449, 2006.
- [38] S. Morita, "Atomically resolved force microscopy at room temperature," *AIP Conf. Proc.*, vol. 1591, no. May, pp. 24–26, 2014.
- [39] T. R. Albrecht, P. Grütter, D. Horne, and D. Rugar, "Frequency modulation detection using high-Q cantilevers for enhanced force microscope sensitivity," *J. Appl. Phys.*, vol. 69, no. 2, pp. 668–673, 1991.
- [40] B. Gotsmann and H. Fuchs, "Dynamic AFM using the FM technique with constant excitation amplitude," *Appl. Surf. Sci.*, vol. 188, no. 3–4, pp. 355–362, 2002.
- [41] S. Morita, R. Wiesendanger, and E. Meyer, *Noncontact Atomic Force Microscopy*. Berlin: Springer, 2002.
- [42] F. J. Giessibl, "Atomic Resolution of the Silicon (111)-(7x7) Surface by Atomic Force Microscopy," *Science*, vol. 267, no. 5194, pp. 68–71, 1995.
- [43] S. Kitamura and M. Iwatsuki, "Observation of 7 x 7 Reconstructed Structure on the Silicon (111) Surface using Ultrahigh Vacuum Noncontact Atomic Force Microscopy," *Jpn. J. Appl. Phys.*, vol. 34, no. Part 2, No. 1B, pp. L145–L148, 1995.
- [44] Y. Sugimoto *et al.*, "Real topography, atomic relaxations, and short-range chemical interactions in atomic force microscopy: The case of the  $\alpha$ -Sn/S(111)-

- ( $\sqrt{3} \times \sqrt{3}$ )R30° surface,” *Phys. Rev. B*, vol. 73, no. 20, p. 205329, 2006.
- [45] R. Pawlak, S. Kawai, S. Fremy, T. Glatzel, and E. Meyer, “High-resolution imaging of C 60 molecules using tuning-fork-based non-contact atomic force microscopy,” *J. Phys. Condens. Matter*, vol. 24, no. 8, p. 84005, 2012.
- [46] L. Gross *et al.*, “Bond-Order Discrimination by Atomic Force Microscopy,” *Science*, vol. 337, no. 6100, pp. 1326–1329, 2012.
- [47] R. Bechstein, C. Gonzalez, J. Schütte, P. Jelinek, R. Perez, and A. Kühnle, “‘All-inclusive’ imaging of the rutile TiO<sub>2</sub> (110) surface using NC-AFM,” *Nanotechnology*, vol. 20, no. 50, p. 505703, 2009.
- [48] J. V Lauritsen *et al.*, “Chemical identification of point defects and adsorbates on a metal oxide surface by atomic force microscopy,” *Nanotechnology*, vol. 17, no. 14, pp. 3436–3441, 2006.
- [49] J. E. Sader and S. P. Jarvis, “Accurate formulas for interaction force and energy in frequency modulation force spectroscopy,” *Appl. Phys. Lett.*, vol. 84, no. 10, pp. 1801–1803, 2004.
- [50] M. Z. Baykara, T. C. Schwendemann, E. I. Altman, and U. D. Schwarz, “Three-dimensional atomic force microscopy - taking surface imaging to the next level,” *Adv. Mater.*, vol. 22, no. 26–27, pp. 2838–2853, 2010.
- [51] B. Uluutku and M. Z. M. Z. Baykara, “Effect of lateral tip stiffness on atomic-resolution force field spectroscopy,” *J. Vac. Sci. Technol. B*, vol. 31, no. 4, p. 41801, 2013.
- [52] B. Uluutku and M. Z. M. Z. Baykara, “Artifacts related to tip asymmetry in high-resolution atomic force microscopy and scanning tunneling microscopy measurements of graphitic surfaces,” *J. Vac. Sci. Technol. B*, vol. 33, no. 3, p. 31802, 2015.
- [53] H. Nejat Pishkenari and A. Meghdari, “Investigation of the atomic-scale hysteresis in NC-AFM using atomistic dynamics,” *Phys. E Low-dimensional Syst. Nanostructures*, vol. 42, no. 8, pp. 2069–2077, 2010.

- [54] A. L. J. Pang, V. Sorkin, Y. W. Zhang, and D. J. Srolovitz, “Self-assembly of free-standing graphene nano-ribbons,” *Phys. Lett. Sect. A Gen. At. Solid State Phys.*, vol. 376, no. 8–9, pp. 973–977, 2012.
- [55] K. Termentzidis *et al.*, “Modulated SiC nanowires: Molecular dynamics study of their thermal properties,” *Phys. Rev. B*, vol. 87, no. 12, p. 125410, 2013.
- [56] W. G. Hoover, “Canonical dynamics: Equilibrium phase-space distributions,” *Phys. Rev. A*, vol. 31, no. 3, pp. 1695–1697, 1985.
- [57] M. E. Tuckerman, J. Alejandre, R. López-Rendón, A. L. Jochim, and G. J. Martyna, “A Liouville-operator derived measure-preserving integrator for molecular dynamics simulations in the isothermal–isobaric ensemble,” *J. Phys. A. Math. Gen.*, vol. 39, no. 19, pp. 5629–5651, 2006.
- [58] L. Nony, A. Baratoff, D. Schär, O. Pfeiffer, A. Wetzel, and E. Meyer, “Noncontact atomic force microscopy simulator with phase-locked-loop controlled frequency detection and excitation,” *Phys. Rev. B - Condens. Matter Mater. Phys.*, vol. 74, no. 23, pp. 1–19, 2006.
- [59] S. Plimpton, “Fast Parallel Algorithms for Short – Range Molecular Dynamics,” *J. Comput. Phys.*, vol. 117, no. 1, pp. 1–19, 1995.
- [60] S. Y. Liem and K. Y. Chan, “Simulation study of platinum adsorption on graphite using the Sutton-Chen potential,” *Surf. Sci.*, vol. 328, no. 1–2, pp. 119–128, 1995.
- [61] S. M. Foiles, M. I. Baskes, and M. S. Daw, “Embedded-atom-method functions for the fcc metals Cu, Ag, Au, Ni, Pd, Pt, and their alloys,” *Phys. Rev. B*, vol. 33, no. 12, pp. 7983–7991, 1986.
- [62] M. Ashino, A. Schwarz, H. Hölscher, U. D. Schwarz, and R. Wiesendanger, “Interpretation of the atomic scale contrast obtained on graphite and single-walled carbon nanotubes in the dynamic mode of atomic force microscopy,” *Nanotechnology*, vol. 16, no. 3, pp. S134–S137, 2005.
- [63] B. J. Albers *et al.*, “Three-dimensional imaging of short-range chemical forces with picometre resolution,” *Nat. Nanotechnol.*, vol. 4, no. 5, pp. 307–310, 2009.